

## Dissertation

# Optimisation of a Compound Lean Turbine Blade in a Linear Cascade

ausgeführt zum Zwecke der Erlangung des akademischen Grades eines Doktors der technischen Wissenschaften unter der Leitung von

Ao.Univ.Prof. Dipl.-Ing. Dr.techn. Reinhard Willinger  
E 302  
Institut für Thermodynamik und Energiewandlung

eingereicht an der Technischen Universität Wien

**Fakultät für Maschinenwesen und Betriebswissenschaften**

von

Dipl.-Ing. Wolfgang Beer  
e 9025009  
1020 Wien, Venediger Au 8

Wien, am 13. Oktober 2008

I dedicate this work to my father.

Ich widme diese Arbeit meinem Vater.

# Kurzfassung

In dieser Arbeit wurde ein lineares Turbinengitter, gebildet aus sogenannten 3D Compound Lean Turbinenschaufeln, optimiert. Ausgangspunkt war eine zylindrische Hochdruckdampfturbinenschaufel, deren 2D Profil aus der Arbeit von Perdichizzi und Dosse-  
na [29] entnommen wurde.

Für die Kalibrierung des numerischen Berechnungsverfahrens (CFD) wurde ein Experiment im Niedergeschwindigkeitswindkanal des Instituts für Thermodynamik und Energie-  
wandlung der Technischen Universität Wien mit einem linearen Schaufelgitter mit zylindrischen Schaufeln durchgeführt. Stromabwärts des Schaufelgitters wurden Druckmes-  
sungen mit pneumatischen Drei- und Fünflochsonden durchgeführt, zusätzlich wurden Profildruckmessungen in halber Schaufelhöhe durchgeführt. Aus den gemessenen Daten wurden weiters Druckkoeffizienten, Geschwindigkeiten und Strömungswinkel berechnet.

Die Optimierung des linearen Schaufelgitters wurde mittels der kommerziellen Programme Fluent (CFD-Solver), Gambit (Geometrieerstellung und Netzgenerierung) sowie eines eigens programmierten genetischen Algorithmus vorgenommen. Die Steuerung der drei beteiligten Komponenten wurde ebenfalls programmiert. Die Randbedingungen für das CFD Modell wurden aus dem Ergebnis des Experiments entnommen. Für die Turbulenzmodellierung wurde ein Standard  $k/\varepsilon$  Turbulenzmodell verwendet. Die Staffelungslinie der Compound Lean Schaufeln wurde aus zwei Parabelstücken an den Seitenwänden und einem geraden Stück in der Schaufelmitte gebildet, das 2D Profil der zylindrischen Schaufel wurde für alle Schaufeln nicht verändert. Zwei Parameter, nämlich der Winkel zwischen der Parabeltangente an der Seitenwand und der Normalenrichtung zur Seitenwand, sowie die Länge des geraden Stücks der Staffelungslinie, wurden während der Optimierung variiert. Als zu optimierende Zielfunktion wurde der globale Totaldruckverlustkoeffizient verwendet. Die Optimierung berechnete, einmal gestartet, ohne jeden manuellen Eingriff selbständig über 1200 Konfigurationen.

Im Anschluß an die Optimierung wurden Rechnung und Messung für die zylindrische Konfiguration verglichen. Sehr gute Übereinstimmung zeigte sich in Bezug auf den Strömungswinkel in Teilungsrichtung und den statischen Druck hinter dem Schaufelgitter in quantitativer und qualitativer Hinsicht. Für die Geschwindigkeit und den Totaldruck stromabwärts des Schaufelgitters waren die Übereinstimmungen zwar sehr gut in qualitativer Hinsicht, jedoch wurden die Verluste vom CFD Verfahren anscheinend als zu hoch berechnet, weshalb es zu Abweichungen in quantitativer Hinsicht kam. Der Strömungswinkel in Richtung der Schaufelhöhe zeigte weder in qualitativer noch in quantitativer Hinsicht gute Übereinstimmung.

Weiters wurde im Anschluß an die Optimierung die zylindrische Ausgangskonfiguration mit zwei optimierten Compound Lean Konfigurationen verglichen. In Bezug auf die Zielfunktion wiesen diese beiden Konfigurationen einen um ca. 1.5% niedrigeren Totaldruckverlustkoeffizienten auf. Insbesondere im Bereich der Seitenwandgrenzschichten zeigten sich bei beiden Compound Lean Konfigurationen Verbesserungen hinsichtlich der Verluste, die beste Konfiguration zeigte auch eine deutlich gleichmäßigere Verteilung

des teilungsgemittelten Abströmwinkels. Erhebliche Verringerungen der aerodynamischen Schaufelbelastungen der Compound Lean Konfigurationen an den Seitenwänden konnten mittels der Profildruckverteilungen beobachtet werden. In Schaufelmitte kam es jedoch teilweise zu Zunahmen der aerodynamischen Schaufelbelastungen bei den Compound Lean Konfigurationen. Verringerungen wurden auch in Bezug auf die Intensität des Kanalwirbels bei den beiden optimierten Konfigurationen festgestellt.

# Abstract

In this work, an optimisation of a linear 3D compound lean turbine blade cascade was performed. A cylindric high-pressure steam turbine blade was used as reference and starting configuration. The 2D blade profile of this cylindric blade was taken from the work of Perdichizzi and Dossena [29].

The numerical calculations were calibrated with an experiment in the low-pressure wind-tunnel of the Institute for Thermodynamics and Energy Conversion of the Vienna University of Technology. This experiment was done with a linear cascade of cylindric blades. Downstream of the cascade pressure measurements were done with three-hole pressure probes and five-hole pressure probes. In addition, profile pressure measurements at midspan were done. Pressure coefficients, velocities and flow angles were calculated from the measured data.

The optimisation of the linear cascade was done by means of the commercial CFD-solver Fluent, the commercial geometry- and grid-generation program Gambit, and a self-programmed genetic algorithm. A program, which controlled all three involved components was self-programmed as well. As boundary conditions for the CFD model the same as observed in the experiment were used. Turbulence was modelled with a Standard  $k/\varepsilon$  model. The staggerline of the compound lean blades consisted of two parabolic arcs at the endwalls and a straight part in between them. The 2D blade profile was not altered for any of the configurations. Two parameters, viz. the angle between the tangent of the parabolic arc and the spanwise direction at the intersection of the endwall and the parabolic arc, and the length of the mentioned straight part of the staggerline, were varied during the optimisation process. Global total pressure loss coefficient was the objective function of choice. The optimisation process calculated, after initialisation, more than 1200 configurations independently of any human interaction.

After the optimisation process, the experiment and the calculation for the cylindric configuration were compared. Very good agreement could be reached for the pitchwise flow angle and the static pressure downstream of the cascade in qualitative and quantitative terms. The agreement for the velocity and the total pressure were quite good qualitatively, but the losses were seemingly calculated too high by CFD, which resulted in quantitative divergences. The spanwise flow angle, however, did not show good agreement, neither qualitatively nor quantitatively.

Finally, two optimised compound lean configurations were compared with the cylindric configuration. Both configurations had a lower value of global total pressure loss coefficient of approximately 1.5%. Especially in the endwall regions both compound lean configuration showed improvements in terms of loss, a remarkably more even distribution of the pitchwise mass-averaged flow angle could be observed for the best configuration. A considerable decrease of aerodynamic bladeload was observed for both compound lean configurations at the endwall by means of blade profile pressure distributions. At midspan, however, to some extent an increase of aerodynamic bladeload could be observed for the compound lean configurations. In addition, a decrease of the intensity of the pas-

sage vortex could be determined for both optimised compound lean configurations.

# Contents

<b>1</b>	<b>Introduction</b>	<b>15</b>
1.1	Motivation . . . . .	15
1.2	Secondary Flow . . . . .	18
1.2.1	Horseshoe Vortex, Counter Vortex . . . . .	19
1.2.2	Passage Vortex . . . . .	19
1.2.3	Corner Vortex . . . . .	20
1.2.4	Trailing Edge Vortex . . . . .	20
1.3	Overview of published Results . . . . .	21
<b>2</b>	<b>Experimental Calibration of the initial Configuration</b>	<b>30</b>
2.1	Wind Tunnel and Measurement Instrumentation . . . . .	30
2.2	Calibration of the Pressure Probes . . . . .	33
2.2.1	Three-Hole Pressure Probe . . . . .	33
2.2.2	Five-Hole Pressure Probe . . . . .	36
2.3	Inlet Conditions . . . . .	40
2.4	Blade and Operating Data of the Investigation . . . . .	40
2.5	2D Measurement . . . . .	42
2.6	3D Measurement . . . . .	45
2.7	Profile Pressure Measurements . . . . .	47
<b>3</b>	<b>Optimisation</b>	<b>51</b>
3.1	Comparison of four widely used Optimisation Techniques . . . . .	51
3.1.1	Hillclimbing . . . . .	51
3.1.2	Simplex Algorithm . . . . .	53
3.1.3	Simulated Annealing . . . . .	53
3.1.4	Genetic Algorithm . . . . .	54
3.2	Definition of the Genetic Algorithm for the given Problem . . . . .	57
3.3	Grid Generation and Boundary Condition Definition . . . . .	60
3.3.1	Meshing of the Computational Domain . . . . .	61
3.3.2	Modelling Turbulence . . . . .	63
3.3.3	Boundary Conditions, nondimensional Variables, numerical Schemes	70
3.4	Optimisation Loop . . . . .	74
3.4.1	Convergence and Reliability Check of the Solutions . . . . .	76
3.4.2	Result of Optimisation . . . . .	77
<b>4</b>	<b>Results</b>	<b>79</b>
4.1	Comparison of Experiment and CFD Calculation . . . . .	79

## Contents

4.1.1	Exit Flow Angles: Pitchwise Flow Angle $\beta_1$ and Spanwise Flow Angle $\gamma_1$ . . . . .	79
4.1.2	Static Pressure Coefficient $C_{p,1}$ . . . . .	81
4.1.3	Exit Flow Velocity $w_1$ . . . . .	84
4.1.4	Total Pressure Coefficient $C_{p,t1}$ . . . . .	85
4.1.5	Profile Static Pressure at Midspan . . . . .	88
4.2	Results of the CFD Optimisation . . . . .	88
4.2.1	Local Total Pressure Coefficient $C_{p,t1}$ . . . . .	90
4.2.2	Pitchwise mass-averaged Total Pressure Coefficient $\overline{C}_{p,t1}$ . . . . .	94
4.2.3	Pitchwise mass-averaged Exit Flow Angle $\overline{\beta}_1$ . . . . .	95
4.2.4	Static Profile Pressure at Midspan and Endwall . . . . .	96
<b>5</b>	<b>Conclusion and Outlook</b> . . . . .	<b>99</b>
5.1	Experiment . . . . .	99
5.2	Optimisation and Numeric Flow Calculation . . . . .	100
5.3	General Developments . . . . .	101
<b>A</b>	<b>Geometric Data of the Blade</b> . . . . .	<b>103</b>
<b>B</b>	<b>Used Software</b> . . . . .	<b>107</b>

# List of Figures

1.1	World Electric Energy Production by Region: 1980 - 2005 in TWh (Source: EIA) . . . . .	16
1.2	Electricity net installed Capacity in the EU-27 Countries by Source [37] .	16
1.3	CO <sub>2</sub> Emissions without LULUCF: Share of largest Key Source Categories in 2006 for EU-15 Countries [3] . . . . .	17
1.4	Horseshoe Vortex [16] . . . . .	19
1.5	Secondary Flow Model of Langston [21] . . . . .	20
1.6	Blade Stacking in Harrison's Experimental Work [10] (Front View in Downstream Direction) . . . . .	22
1.7	Origin and Importance of Aerodynamic Losses in Reaction Stages . . . .	24
2.1	Variation of Density Ratio with Mach number . . . . .	31
2.2	Sketch of Windtunnel . . . . .	32
2.3	Sketch of Cascade Measuring Setup . . . . .	32
2.4	Sketch of Three-Hole Pressure Probe . . . . .	34
2.5	Calibration Data of the Three-Hole Pressure Probe: Yaw Angle Coefficient $k_\beta$ , Total Pressure Coefficient $k_t$ , Static Pressure Coefficient $k_s$ . . .	35
2.6	Sketch of Five-Hole Pressure Probe . . . . .	36
2.7	Calibration Data of the Five-Hole Pressure Probe: Pitch Angle Coefficient $k_\beta$ vs. Yaw Angle Coefficient $k_\gamma$ . . . . .	37
2.8	Bilinear Interpolation: Element with 4 Nodes . . . . .	38
2.9	Calibration Data of the Five-Hole Pressure Probe: Total Pressure Coefficient $k_t$ . . . . .	39
2.10	Calibration Data of the Five-hole Pressure Probe: Static Pressure Coefficient $k_s$ . . . . .	39
2.11	Sketch of Blade Cascade . . . . .	41
2.12	Pitchwise Exit Flow Angle $\beta_1$ at Midspan with Three-Hole Pressure Probe (Probe Setup-Angle $\Delta\xi = 15^\circ$ ) . . . . .	43
2.13	Cascade Exit Flow Velocity Ratio at Midspan with Three-Hole Pressure Probe (Probe Setup-Angle $\Delta\xi = 15^\circ$ ) . . . . .	44
2.14	Total Pressure Coefficient $C_{p,t1,MS}$ at Midspan with Three-Hole Pressure Probe (Probe Setup-Angle $\Delta\xi = 15^\circ$ ) . . . . .	45
2.15	Pitchwise Exit Flow Angle $\beta_1$ with Five-Hole Pressure Probe (Probe Setup-Angle $\Delta\xi = 15^\circ$ ) . . . . .	46
2.16	Spanwise Exit Flow Angle $\gamma_1$ with Five-Hole Pressure Probe (Probe Setup-Angle $\Delta\xi = 15^\circ$ ) . . . . .	48
2.17	Total Pressure Coefficient $C_{p,t1}$ with Five-Hole Pressure Probe (Probe Setup-Angle $\Delta\xi = 15^\circ$ ) . . . . .	49

*List of Figures*

2.18	Static Profile Pressure Coefficient $C_p$ at Midspan . . . . .	50
3.1	Good qualified Search Domain (Global Optimum) for Hillclimbing Algorithm	52
3.2	Bad qualified Search Domain (Local Optimum) for Hillclimbing Algorithm	53
3.3	Pseudocode for Simulated Annealing Optimisation Algorithm . . . . .	54
3.4	The two altered Parameters of the 3D Configuration . . . . .	58
3.5	2D Sketch of Computational Domain . . . . .	61
3.6	Calculation of Vertex Coordinates of Parabola . . . . .	62
3.7	Time-Averaging for Stationary Turbulence . . . . .	65
3.8	Turbulent Boundary Layer: Viscous Sublayer, Overlap Region and Log Layer . . . . .	70
3.9	Velocity Inlet: 1/7 Power Law . . . . .	73
3.10	Flow Chart of Optimisation Loop . . . . .	75
3.11	CFD Solution Space . . . . .	76
3.12	Contour Plot of Total Pressure Loss Coefficient $\omega$ of Optimisation . . . . .	78
4.1	Comparison of Experiment and CFD Calculation: Three-Hole Pressure Probe, Pitchwise Exit Flow Angle $\beta_1$ at Midspan . . . . .	80
4.2	Four different Coordinate Systems for the Experiment . . . . .	80
4.3	Comparison of Experiment (a) and CFD Calculation (b): Five-Hole Pressure Probe, Pitchwise Exit Flow Angle $\beta_1$ . . . . .	82
4.4	Comparison of Experiment (a) and CFD Calculation (b): Five-Hole Pressure Probe, Spanwise Exit Flow Angle $\gamma_1$ . . . . .	83
4.5	Comparison of Experiment and CFD Calculation: Three-Hole Pressure Probe, Static Pressure Coefficient $C_{p,1}$ at Midspan . . . . .	84
4.6	Comparison of Experiment and CFD Calculation: Three-Hole Pressure Probe, Cascade Exit Flow Velocity Ratio at Midspan . . . . .	85
4.7	Comparison of Experiment and CFD Calculation: Three-Hole Pressure Probe, Total Pressure Coefficient $C_{p,t1,MS}$ . . . . .	86
4.8	Comparison of Experiment (a) and CFD Calculation (b): Five-Hole Pressure Probe, Total Pressure Coefficient $C_{p,t1}$ . . . . .	87
4.9	Comparison of Experiment and CFD Calculation: Static Profile Pressure Coefficient $C_p$ at Midspan . . . . .	89
4.10	Comparison of Total Pressure Coefficient $C_{p,t1}$ of Set 1 (a) and Set 2 (b) .	91
4.11	Comparison of Total Pressure Coefficient $C_{p,t1}$ of Set 1 (a) and Set 3 (b) .	92
4.12	Comparison of Total Pressure Coefficient $C_{p,t1}$ of Set 2 (a) and Set 3 (b) .	93
4.13	Pitchwise mass-averaged Total Pressure Coefficient $\overline{C_{p,t1}}$ . . . . .	94
4.14	Pitchwise mass-averaged Exit Flow Angle Deviation $\Delta\overline{\beta_1}$ . . . . .	96
4.15	Static Profile Pressure Coefficient $C_p$ at Midspan . . . . .	97
4.16	Static Profile Pressure Coefficient $C_p$ at Endwall . . . . .	98
A.1	Model Blade Profile (Original Size) . . . . .	104
A.2	Model Blade for Static Pressure Measurements . . . . .	106

# List of Tables

1.1	Reduction of Power Output due to CO <sub>2</sub> Sequestration . . . . .	18
2.1	Technical Data of Axial Fan of Windtunnel . . . . .	30
2.2	Cascade Geometric Data . . . . .	41
2.3	Main Flow Data for the Experiment . . . . .	42
3.1	Initial Population of the Genetic Algorithm . . . . .	60
3.2	Approximate Regions of Local Optima . . . . .	77
4.1	Geometry Parameters and Objective Functions of evaluated Configurations . . . . .	89
A.1	Blade Profile Coordinates . . . . .	105

# Notation

## English Letters and Symbols

$AR$	Blade aspect ratio, $\frac{H}{c}$
$b$	Axial chord length
$C$	Integration constant
$C_D$	Boundary layer dissipation integral
CFD	Computational Fluid Dynamics
$c$	Chord length
$c_p$	Specific heat capacity at constant pressure
$c_v$	Specific heat capacity at constant volume
GA	Genetic algorithm
$H$	Blade height
HP	High-pressure
$h$	Length of straight part of compound lean blade
IP	Intermediate-pressure
$i$	Incidence angle
$k$	Turbulent kinetic energy
$L$	Blade loading parameter
$LI$	Leakage Flow interaction
LP	Low-pressure
$Ma$	Mach number
$o$	Throat width
PS	Pressure side
$p$	Static pressure
$p_c$	Probability of crossover
$p_m$	Probability of mutation
$R$	Gas constant
RANS	Reynolds-averaged Navier Stokes
$Re$	Reynolds number
$S$	Sutherland Constant
$S$	Vertex
SS	Suction side
$s$	Entropy
$s_{ij}$	Strain-rate tensor
$T$	Temperature
$T$	Time (period)

## Notation

$T_0$	Reference temperature for Sutherland's law
$Tu$	Turbulence intensity
$t$	Pitch length
$t$	Time
$t$	Tangent
$t_{ij}$	Viscous stress tensor
$U$	Free Stream Velocity
$u$	Velocity component in $x$ -direction
$u_\tau$	Friction velocity
$u^+$	Nondimensional, sublayer scaled, velocity
$v$	Velocity component in $y$ -direction
$w$	Velocity component in $z$ -direction
$w$	General notation for velocity
$y^+$	Nondimensional, sublayer scaled, wall-distance

## Greek Letters and Symbols

$\Delta$	Incremental difference
$\Delta\beta$	Relative flow turning angle
$\Delta\xi$	Pressure probe setup-angle
$\alpha$	Angle between tangent of parabolic arc and spanwise direction at endwall for 3D-blades
$\beta$	Blade angle
$\beta$	Flow angle
$\beta$	Pitch angle
$\gamma$	Yaw angle
$\gamma$	Stagger angle
$\delta$	Boundary layer thickness
$\delta_{ij}$	Kronecker delta
$\varepsilon$	Turbulent dissipation rate
$\varepsilon$	Absolute surface roughness
$\theta$	Momentum displacement thickness
$\kappa$	Adiabatic exponent
$\kappa$	Kármán's constant
$\mu$	Dynamic viscosity
$\mu_0$	Reference viscosity at reference temperature $T_0$
$\nu$	Kinematic viscosity
$\nu_t$	Kinematic eddy viscosity, $\frac{\mu_t}{\rho}$
$\xi$	Boundary layer entropy generation rate per unit area
$\xi_{Sec}$	Secondary loss generation
$\rho$	Density
$\tau_W$	Wall shear stress
$\tau_{ij}$	Specific Reynolds stress tensor

## Notation

$\omega$	Total pressure loss coefficient
$\zeta$	Aerodynamic loss

## Superscripts

$\overline{(\quad)}$	Pitchwise mass-averaged
$\overline{(\quad)}$	Time-averaged
$\overline{(\quad)}$	Area mass-averaged
*	Nondimensional
'	Nozzle

## Subscripts

0	Inlet
1	Outlet
<i>dyn</i>	Dynamic
<i>Leak</i>	Leakage
<i>MS</i>	Midspan
<i>Prof</i>	Profile
<i>ref</i>	Reference
<i>Sec</i>	Secondary
<i>s</i>	Isentropic
<i>t</i>	Total
<i>t</i>	Turbulent

# 1 Introduction

Nothing has such power to broaden the mind as the ability to investigate systematically and truly all that comes under thy observation in life.

---

*(Marcus Aurelius Antonius  
Augustus,  
Roman Emperor)*

## 1.1 Motivation

Electric energy drives the economy of the entire world. As the economy grows, the thirst for energy in general, and for electric energy in especially is rising too. Figure 1.1 shows the growing demand for electric energy worldwide. It is important to note, that the demand of Asia and Oceania has already surpassed those of Europe and North America and, in addition, is growing more rapidly than the other ones. According to the Energy Information Administration, the electric power generation of the world will allmost double from 16424 TWh in the year 2004 to 30364 TWh in the year 2030 [2].

For the example of the EU-27 countries, it can be seen from Fig. 1.2 that, although alternative concepts (termed "Others" in Fig. 1.2) such as geothermal power, windpower, biomass, etc., become more and more important, fossil fuelled thermal power plants still form the backbone of today's electric energy production with a share of roughly 50% of the total production. They will probably continue to play that important role for the next 50 years or so to come, in the author's opinion <sup>1</sup>. Burning fossil fuels generates greenhouse gases, of which CO<sub>2</sub> is probably the best known. They are widely accepted to be the main source of global warming and climate change. To challenge the difficult task of reducing the CO<sub>2</sub> and other greenhouse gas emissions, the Kyoto protocol was introduced in 1997 as an amendment to the United Nations Framework Convention on Climate Change (UNFCCC). Its objective is to commit the individual countries to reduce their greenhouse gas emissions. The EU for example has agreed on reducing its greenhouse gas emissions by 8% compared to the reference value of 1990, leaving it up to the EU institutions to allocate different burdens for different member states.

To get an idea how the greenhouse gas emissions are distributed among the different key source categories Fig. 1.3 shows the shares of those key source categories for the EU-15

---

<sup>1</sup>A revival of nuclear power can be observed recently in Europe, but is not yet reflected in the data up to 2006.

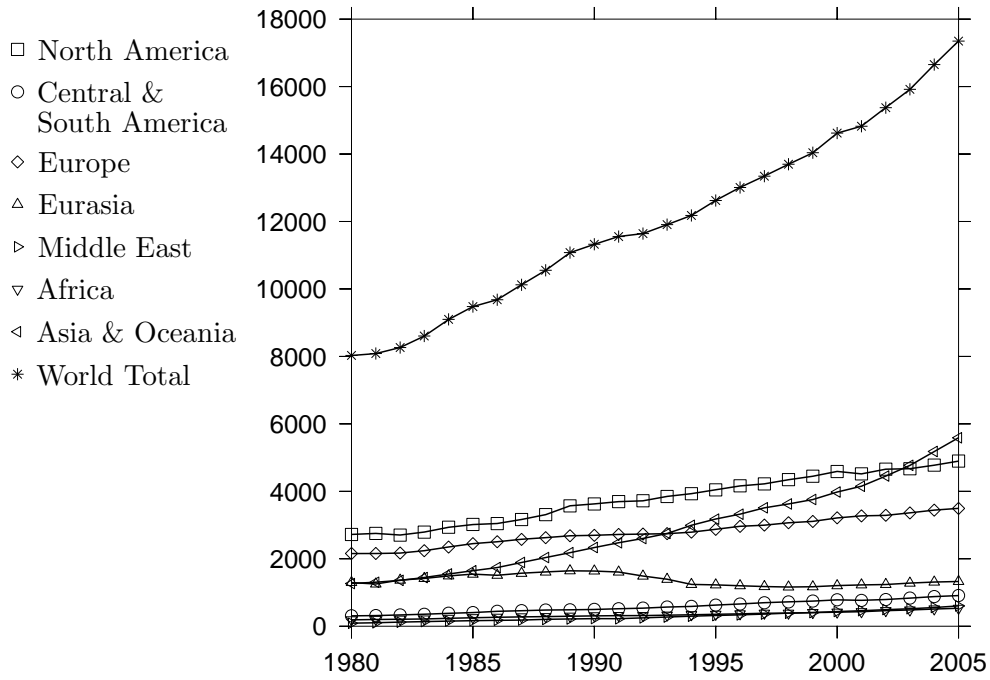


Figure 1.1: World Electric Energy Production by Region: 1980 - 2005 in TWh (Source: EIA)

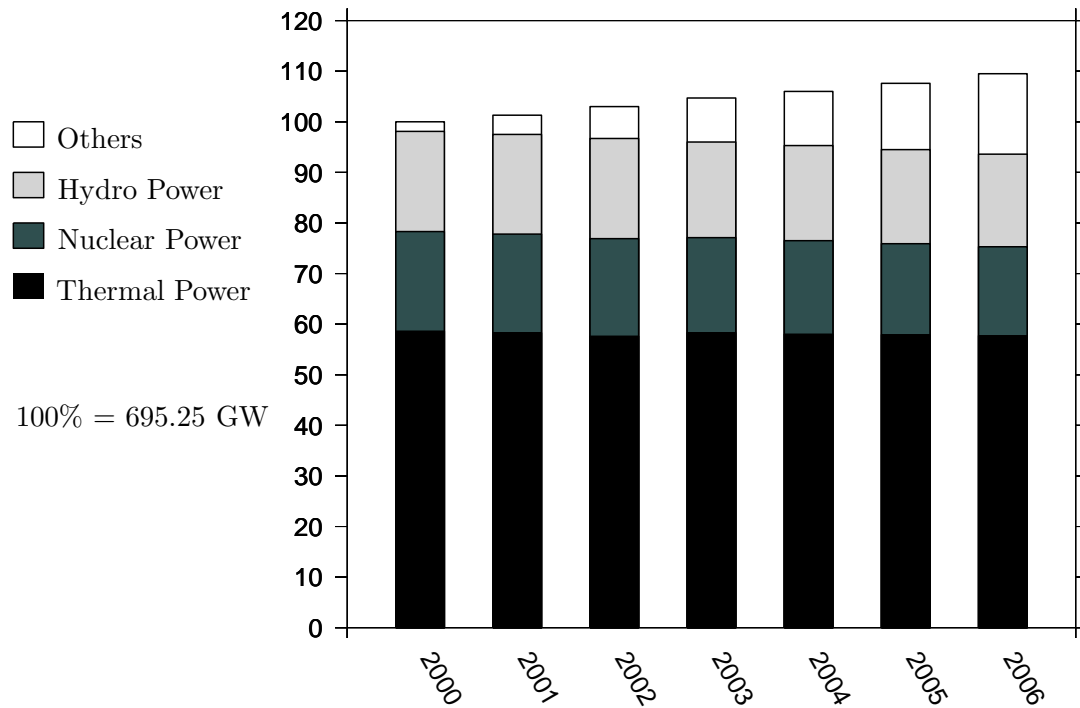


Figure 1.2: Electricity net installed Capacity in the EU-27 Countries by Source [37]

## 1 Introduction

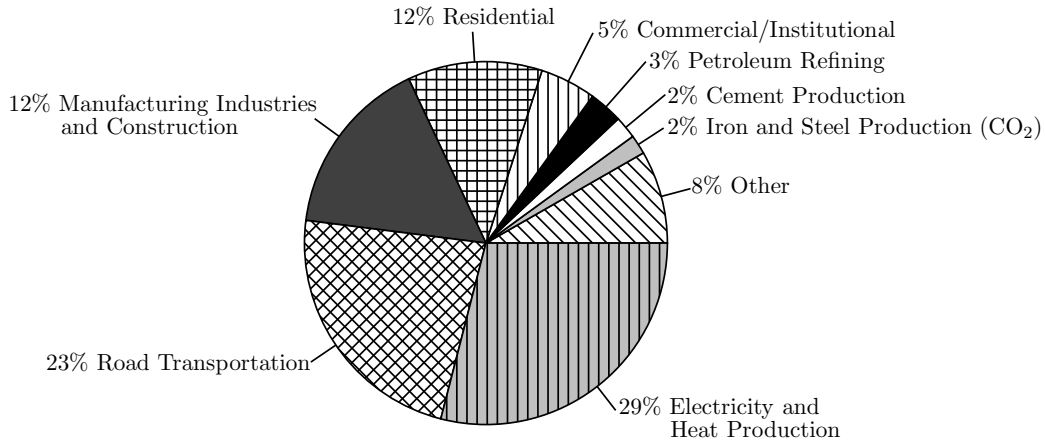


Figure 1.3: CO<sub>2</sub> Emissions without LULUCF<sup>4</sup>: Share of largest Key Source Categories in 2006 for EU-15 Countries [3]

countries for the year 2006<sup>2</sup>.

The CO<sub>2</sub> emissions of electricity production and heating account for nearly one third of total emissions, therefore there exists an urgent need for action to reduce those emissions. As mentioned above, CO<sub>2</sub> is always produced, when fossil fuels are burned, and can not be evaded, so technical concepts for CO<sub>2</sub> sequestration were developed and tested in small and medium sized experiments in the last years. These concepts are now awaiting their final real sized tests and will then probably be available for full scale use in thermal power plants. The swedish Vattenfall group is currently building a Zero-CO<sub>2</sub>-emission hard-coal fired Demonstration Power Plant in Eastern Germany with a thermal output of 30 MW<sup>3</sup>. It is planned to start operation in mid-2008. CO<sub>2</sub> emissions will be reduced with an Oxyfuel-process by 90 %. The german RWE group is currently planning and projecting an Integrated Gasification Combined Cycle (IGCC) power plant which is going to be coal fired. It is planned to start operation in 2014 and will have a net electric output of 360 MW (gross electric output: 450 MW) [12]. There is a certain drawback to all those CO<sub>2</sub> capture and storage (CCS) techniques, namely that they are quite energy consuming themselves. According to Ploetz [30], the different process types for CO<sub>2</sub> sequestration result in a decrease of efficiency between 7 to 14 percentage points for the whole power plant. The total output of the different types of power plant would be significantly decreased with current technology, but even for technology, which will only be available in the future<sup>5</sup>, the reduction in power output is still an alarmingly high number (compare Tab. 1.1), as these reductions raise the price of electricity considerably.

It is therefore of utmost importance to increase the efficiency of power plants as high

<sup>2</sup>Complete data for the EU-27 countries was not available, but it is assumed, that the EU-15 data is closely comparable to the EU-27 data.

<sup>3</sup>[http://www.vattenfall.de/www/vf/vf\\_de/225583xberx/228227umwel/228407klima/228587co2-f/index.jsp](http://www.vattenfall.de/www/vf/vf_de/225583xberx/228227umwel/228407klima/228587co2-f/index.jsp)

<sup>4</sup>Land Use, Land Use Change and Forestry

<sup>5</sup>"Future" was not specified exactly in the cited work.

Power Plant Type	Power output decrease Current Technology [%]	Power output decrease "Future" Technology [%]
Conventional Coal Fired Power Plant	27 - 37	15
Gas Fired Power Plant	15 - 25	10 - 11
Advanced Coal Fired Power Plant	13 - 17	9

Table 1.1: Reduction of Power Output due to CO<sub>2</sub> Sequestration

as possible. Even very small improvements in efficiency result in high economic savings, when considering the operation hours per year and the long operation times of power plants and their huge consumption of primary energy. One of the key components of fossil fuelled power plants is without doubt the turbomachine, be it a steam turbine or a gas turbine. Amongst the most important components, that determine the performance and efficiency of a turbine, are for sure the turbine blades. Therefore, increasing the performance of the turbine blades is certainly an objective, that is very promising when trying to increase the efficiency and performance of a turbine.

In this work, a linear high-pressure steamturbine stator blade cascade will be optimised by making use of a genetic algorithm and CFD. Amongst the many methods that are known to influence the performance and efficiency of turbine bladings, 3D compound lean was the approach of choice. The CFD calculation will be calibrated by experimental data, which will be derived from an experiment in the institute's windtunnel.

## 1.2 Secondary Flow

Losses due to secondary flow are the major loss source in HP turbine (reaction) stages (compare Fig. 1.7), so presumably the most promising field for increasing the efficiency of a HP turbine stage is decreasing those losses. There are many model theories about the origin and development of the various vortex systems and their importance for secondary flow and the losses induced by secondary flow. Sieverding [35] and Langston [21] give very broad overviews of the work done so far. However, when going through all those theories it turns out, that despite all their differences and the different interpretations for all the phenomenons observed, five basic vortices are more or less equal to all of them, viz.

- the horseshoe vortex,
- the passage vortex,
- the counter vortex,
- the corner vortex, and
- the trailing edge vortex.

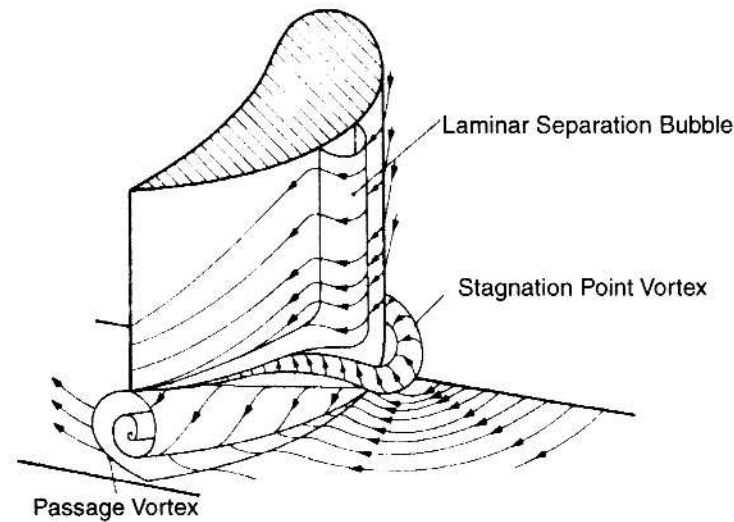


Figure 1.4: Horseshoe Vortex [16]

A model sketch of the passage vortex and the counter vortex is presented in Fig. 1.5, the horseshoe vortex is presented in Fig. 1.4 <sup>6</sup>.

3D compound lean shape is known to have a positive influence on the reduction of losses due to secondary flow in linear turbine blade cascades, which qualifies it as the method of choice for this work.

### 1.2.1 Horseshoe Vortex, Counter Vortex

Whenever a wallbounded viscous flow meets an obstacle, such as the leading edge of a turbine blade, a positive pressure gradient towards the endwall is being exerted. The endwall boundary layer cannot withstand this adverse pressure and curls up into the horseshoe vortex, which is further transported around the leading edge of the blade. The pressure side leg of this horseshoe vortex is pushed towards the suction side of the blade passage due to the pressure gradient between pressure and suction side and merges with the passage vortex. The suction side leg, rotating in the opposite direction of the passage vortex, becomes the counter vortex in the blade passage.

### 1.2.2 Passage Vortex

The passage vortex is mainly induced by the pitchwise pressure gradient inside the blade passage. In the undisturbed flow region the pressure gradient due crossflow is balanced

---

<sup>6</sup> called Stagnation Point Vortex there

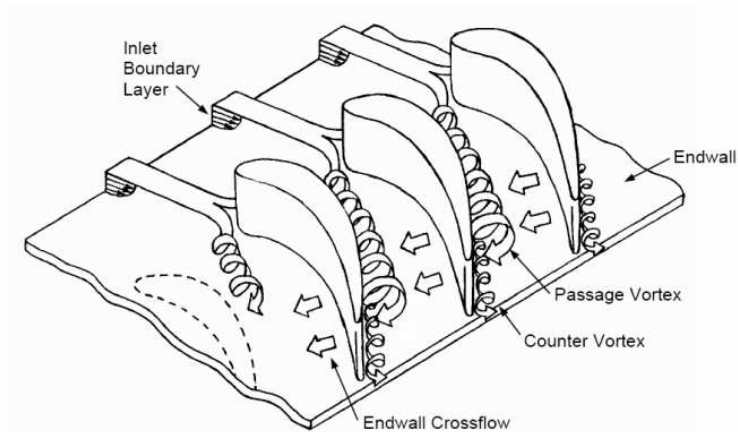


Figure 1.5: Secondary Flow Model of Langston [21]

out by the forces due to the turning of the flow. In the endwall regions, as the flow velocity in the main direction decreases in the endwall boundary layer, the forces due to the pitchwise pressure gradient exceed the acceleration forces, and crossflow occurs. This crossflow continues on the blade profiles for reasons of mass conservation and develops into the passage vortex. The higher the flow turning angle, the higher the bladeload and the pitchwise pressure gradient, and the stronger gets the passage vortex.

### 1.2.3 Corner Vortex

The corner vortex, being much smaller than the passage vortex, is very difficult to verify experimentally. It is situated in the corner of the endwall and the blade suction side. The size of the corner vortex depends very much on the aerodynamic bladeload, the higher the load, the larger the corner vortex. The corner vortex originates from the interference of the passage crossflow and the near-wall flow in the blade passage. As a consequence, the boundary layer of the near-wall flow curls up into what is defined as the corner vortex.

### 1.2.4 Trailing Edge Vortex

The trailing edge vortex is located behind the trailing edge of the blade. At this position, the blade pressure side flow, flowing towards the endwall, and the blade suction side flow, flowing towards midspan, come together in the wake of the blade. This causes the so-called trailing edge vortex. As with all the other vortices described, again, the intensity depends on the turning angle of the blade, the stronger the flow turning the stronger the trailing edge vortex.

### 1.3 Overview of published Results

In this chapter, the results of research done so far in the fields of

- secondary flow and endwall losses,
- numerical calculation of turbomachinery flow, and
- optimisation of turbomachinery flow

are presented, as far as they are in conjunction with this work. It is quasi impossible to group those works into meaningful categories, as they all touch, in one way or the other, more than one field of those mentioned above. Therefore, it was chosen to list them chronologically.

In 1977 Langston et al. [22] performed investigations in a low speed linear cascade to find out more about the origin, nature and development of three-dimensional flows in turbine cascade passages. They used cylindrical blades with an aspect ratio of  $AR=0.9888$ , a turning angle of  $110.03^\circ$  and a pitch/chord ratio  $\frac{t}{c} = 0.78$ . Velocity and pressure measurements were performed before, within and behind the cascade passage, using a five-hole pressure probe. Flow visualisations were made with ink and smoke traces on the various surfaces and inside the passage respectively. In addition hot wire measurements were taken in the endwall boundary layer within the cascade passage. The inlet Reynolds number was  $7.22 \cdot 10^5$ , based on the blade chord length, the endwall boundary layer thickness was measured to be 3.3 cm. The flow visualisations revealed the well-known three-dimensional separation and reattachment lines of the flow, underlining the strong three-dimensional nature of the flow. The saddle point in front of the horseshoe vortex, where the two separation and reattachment lines intersect <sup>7</sup> could be observed quite clearly as well. Static pressure taps in the blades at 50 percent, 25 percent, 12.5 percent and 2.3 percent of span were used to determine the blade loading. Excellent agreement between the measured and calculated values of static pressure could be reached on the pressure surface of the blade. The calculations were the result of a two-dimensional potential flow calculation. On the suction surface the agreement between measured and calculated values was good at 50 percent span. At the other locations on the suction surface towards the endwall, the effects of three-dimensional flow began to show up, as the measured values began to deviate more and more from the potential solution. At the endwall, the static pressure measurement values showed big differences from the potential flow calculations. The minimum pressure in the cascade did no longer occur on the suction side surface of the blade, as in the calculation, but had moved into the flow channel between the blades. The flow field measurements, with the five-hole pressure probe showed the curling up of the inlet boundary layer (13 percent axial chord) and the formation of the passage vortex (57 percent axial chord) and finally the fully developed passage vortex just before the blade exit. The formation of a new, very thin, endwall boundary layer, just after suction separation line of the inlet boundary layer, was observed with hot wire technology. Due to the extreme thinness of this new boundary layer, no

---

<sup>7</sup>compare [35] and [21]

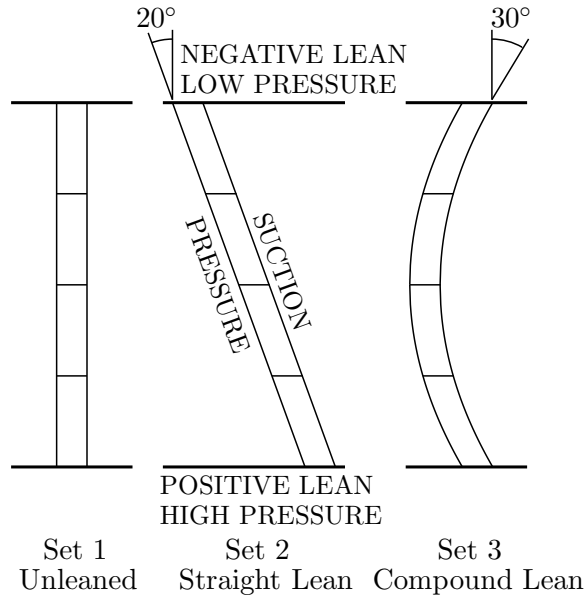


Figure 1.6: Blade Stacking in Harrison's Experimental Work [10] (Front View in Downstream Direction)

further measurements could be made to find out more about the nature of this boundary layer.

In 1992 Harrison [10] did some experimental research to find out more about the influence that blade lean has on the losses of turbines. In a linear cascade he investigated three sets of nozzle blades, an unleaned, cylindrical set (Set 1), a straight, simple, lean set (Set 2), and a compound lean set (Set 3) with positive lean on both ends<sup>8</sup>. The blade stacking is shown in Fig. 1.6.

Measurements included surface static tappings on the blade and endwall surfaces, traverses within and downstream of the blade rows with five-hole probes, a three-hole "cobra" probe and a flattened Pitot probe. Harrison discovered a dramatic change of static pressure on the leaned blades, especially at midchord, which, he argued, had consequences for the thickness and the structure of the incoming boundary layers at the endwalls (thickening and decelerating at the high pressure endwall, thinning and accelerating at the low pressure endwall), as well as for the vortex systems that developed in the blade passage. In addition he found out, that the spanwise variation of pitchwise average exit flow angle was larger for Set 2 than for Set 1 and Set 3, which happened to have the smallest variation of all (30% less than Set 1). Harrison identified five potential influences on the general loss generation in a turbine cascade:

- Flow velocities<sup>9</sup>

<sup>8</sup>Positive means the blades are leaned in the "circumferential" direction, so they have a convex pressure side.

<sup>9</sup> Going out from the assumption of a constant boundary layer dissipation integral  $C_D = T\xi/\rho U^3$  for

## 1 Introduction

- Blade Surface Boundary Layer Transition
- Endwall Boundary Layer Transition
- Mixing Loss
- Other Effects

Harrison concluded, that simple lean marginally increased the loss coefficient whereas compound lean had no overall effect on loss. However, compound lean was found to increase flow turning, to reduce downstream mixing losses and to substantially reduce spanwise variations in mean flow angle, which would lead to an improvement in turbine efficiency.

In 1994 Wanjin et al. [42] performed straight cascade experiments with four different sets of blades with very low aspect ratios ( $AR = 0.917$ ) and very high turning angles ( $\Delta\beta = 128.5^\circ$ ), namely with a straight, cylindrical, set, a straight lean set, a positively curved compound lean set and a negatively curved compound lean set<sup>10</sup>. They used 10 measuring planes in their cascade, two in front of the cascade entry, seven inside the cascade and one behind the exit of the cascade. The measurements were done in a low speed facility with Reynolds number and Mach number at midspan of the cascade exit plane being  $Re = 6.4 \cdot 10^5$  and  $Ma = 0.26$ . In these experiments it was experienced, that the intensity and scale of the horseshoe vortices were bigger in acute angles between endwall and leaned blades and between endwall and positively curved blades than between endwall and the corresponding obtuse angles of the blades. The opposite was true for negatively curved blades. According to the authors, the suction side leg of the horseshoe vortex, which, in other publications is often termed counter vortex, as it rotates in the opposite direction of the passage vortex, was gradually dissolved by the shear forces when getting in contact with the passage vortex. For the passage vortices, Wanjin et al. found out, that they developed later in the blade passage, stayed nearer at the endwalls and were weaker for negatively curved blades and in obtuse angle zones than for positively curved blades and acute angle zones. In addition, the passage vortices from both endwalls did not merge at midspan in the blade passage for the negatively curved blades, therefore they did not produce that much loss as they did for the straight, leaned or positively curved blades. For the cascades tested, Wanjin et al. indicated the mass flux-averaged total loss coefficients to be 0.1948, 0.1883, 0.2255 and 0.1572 for straight, leaned, positively curved and negatively curved blades. A favourable redistribution of the outflow angle was also observed by the researchers, i.e. lower under- and overturning.

It shall be annotated, that to the author's best knowledge, this is the only evidence where a reduction of total pressure loss and a favourable impact on secondary flow was observed with negative compound lean blades.

---

"typical" turbulent boundary layers, the relevant influence on boundary layer losses is the integral  $\int U^3 dA$  only. It turned out, that the proportional effect of  $\int U^3 dA$  was greater on endwalls than on the blade surfaces, but as the suction surface accounted for nearly 2/3 of the overall  $\int U^3 dA$ , the effects of lean on overall loss were negligible.

<sup>10</sup>Negative here means, that the blades are leaned against the "circumferential" direction, so they have a concave pressure side.

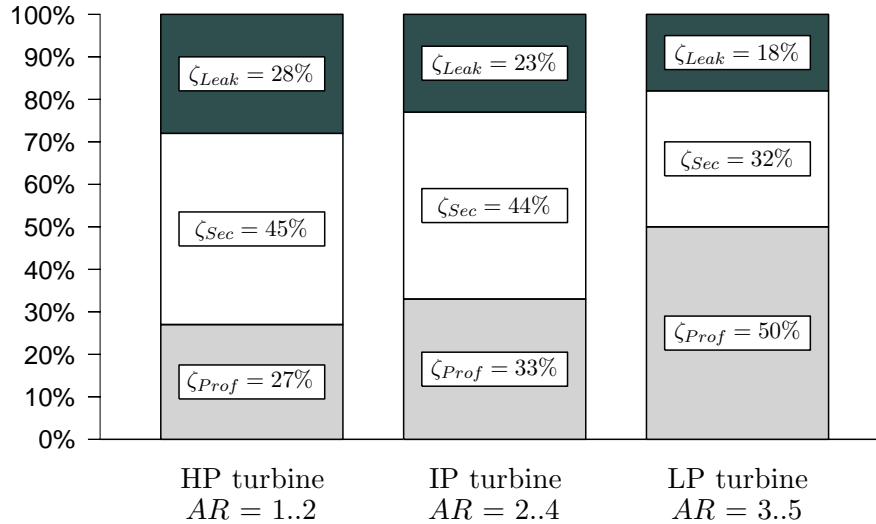


Figure 1.7: Origin and Importance of Aerodynamic Losses in Reaction Stages

Havakechian and Greim [11] gave an extensive overview of their work concerning the reduction of aerodynamic losses in 50 percent reaction steam turbines in the last decade of the 20th century. They cover all sorts of stages, HP, IP and LP with the respective aspect ratios  $AR$  ranging from  $1 < AR < 5$ , Reynolds number ranges from  $0.5 \cdot 10^6 < Re < 15 \cdot 10^6$ , and Mach numbers in the low and mid-to-high subsonic ranges ( $Ma \cong 0.25..0.55$ )<sup>11</sup>. The origin and importance of the different losses, namely profile losses, secondary losses and losses due to leakage are depicted for the different stages in Fig. 1.7.

All sorts of tools and techniques, such as

- advanced one-dimensional (1D) design tools
- quasi-three-dimensional (Q3D) design tools
- three-dimensional (3D) design tools
- cascade testing
- advanced three-dimensional turbine bladings
- Computational Fluid Dynamics
- experimental validation in a five-stage model turbine

were investigated, and their results were combined in one vast blading development project. The Q3D/3D-methods consisted of S2<sup>12</sup> calculations, S1<sup>13</sup> calculations, the combination of both, and automation of combined 1D-, Q3D- and 3D-methods. It turned out, that the combination of S1 potential code, coupled with a 2D finite difference boundary layer program produced an excellent resolution of the flow field and had excellent

<sup>11</sup>This is true for HP and IP stages, for LP stages this is only valid for the first stages

<sup>12</sup>meridional flow

<sup>13</sup>blade-to-blade flow

## 1 Introduction

predictive capabilities with respect to exit angle and surface pressure distribution. Making use of various types of 3D codes <sup>14</sup>, while using Q3D results as boundary conditions, superimposed by additional features such as inlet boundary layers enabled the designer to view the 3D flow field in acceptable time scales. Advanced vortex design methods, which means usage of alternative elaborated twist schemes of blades in order to decrease the consequences of extreme values of reaction at hub and tip sections, were used to positively influence design criteria, such as minimisation of the spanwise gradient of total pressure, reduction of the velocity level at endwalls or reduction of flow turning at endwalls for example.

Profile design and optimisation was done by Havakechian and Greim by employing a Bézier - Bernstein curve/surface representation for describing the profile section as well as the 3D airfoil geometry, as this method proved to be superior in terms of flexibility to the classical methods, where prescribed thickness distributions are superimposed on circular or parabolic camberlines. Going a step further they implemented a complete automated profile contour design system, which, while observing the desired precise Q3D/3D aerodynamic and mechanical constraints, generated the whole 3D polynomial surface at very short design cycle time.

Secondary loss generation in a turbine stage can be assumed to be a function of the following parameters, according to Havakechian and Greim:

$$\xi_{Sec} = f(H/c, t/c, \Delta\beta, w_1/w_0, L, \theta_0/H, \delta_0/H, \theta_1/o, \delta_1/o, Re, Ma_1, Tu, \varepsilon/c, LI) \quad (1.1)$$

To decrease secondary flow and its negative effects, e.g. increase of loss, several approaches namely Lean, Meridional endwall contouring (MEWC) and Tangential endwall contouring (TEWC) were investigated by the two researchers. Experimental research, done in a multistage environment with constant section compound leaned blading (pressure side convexing), showed that a stage efficiency increase of  $\Delta\eta_{(H/c=2)} = 0.7\%$  could be reached. The methods and results for MEWC and TEWC will not be treated further here.

Lampart et al. [19] performed numerical studies of the effects of compound lean and compound twist <sup>15</sup> of stator blades for HP turbine stages in 1999. The stage with cylindrical blades was an impulse type stage with an average degree of reaction  $R_k = 0.2$ . The compound lean stator blades consisted of straight part in the middle section of the blade, and two parabolic parts at the endwalls, resulting in a convex pressure side of the blade. The compound twist blade had a curved leading edge, as the compound lean blade <sup>16</sup>, but the trailing edge of the blade was strictly kept radial. Two configurations of the compound twist blade were examined, one with varying chord length, the other with fixed chord

---

<sup>14</sup>In-house 3D Euler and Navier Stokes codes but also commercially available codes such as Fluent products

<sup>15</sup>This type of blade is often referred to as "Controlled Flow Nozzle".

<sup>16</sup>The leading edge curvature, contrary to the compound lean blade, consisted of a full parabolic arc.

length. The second compound twist component resulted in a concaved curved leading edge. The calculations were done with the CFD code FlowER, modelling turbulence with an algebraic modified Baldwin Lomax model without wall functions. Tip leakage and unsteady effects were not considered. The calculations of Lampart et al. showed an increase of stage efficiency of up to 0.4%, expressed in a decrease of overall kinetic energy loss. The increase of stage efficiency for the compound twist configuration was 0.4% for the configuration with fixed chord length and 0.2% - 0.3% for the design, where the chord length was enlarged towards the endwalls to maintain a straight stator leading edge. For both configurations, compound lean and compound twist, a significant redistribution of the mass flux inside the blade passages was observed. Lampart and Gardzilewicz [18] published additional findings for the same, when speaking of the original cylindrical configuration, HP turbine stage. Boundary conditions and operating data were equal to those in [19]. Straight lean produced mutually opposing effects on the opposite endwalls, resulting in a redistribution of mass flux, reaction and kinetic energy loss. The improvement for the stage did not exceed 0.2%. Lampart particularly pointed out, that for all four configurations, the choice of the parameters, e.g. lean angle, circumferential displacement of the stator blades at the endwalls compared to the mid-span sections, etc., is crucial for the beneficial effects of 3D shaping. Bad choice of those parameters can also result in unfavourable effects on the stage efficiency.

Some first approaches to employ a Genetic Algorithm (GA) for automatic 2D blade profile generation were made in the late nineties of the past century by Trigg et al. [39]. The motivation was to significantly reduce the time for designing new and more efficient blade profiles, as this was done manually by experienced designers until then. Only the introduction of modern CFD programs and the availability of fast and inexpensive computers had made this approach, automatic design and analysis instead of empirical methods applied by experienced designers, possible. Trigg et al. optimised a 2D impulse blade profile defined by 17 parameters, which were calculated with a refined method of blade profile generation of Pritchard [32]. Profile loss coefficient<sup>17</sup> was the objective function chosen to be optimised, the fluid-mechanical calculations were done with a CFD code for steady viscous compressible fully turbulent flow created by Dawes [6]. The robustness and the speed of the algorithm turned out to fulfill the expectations, as one step of evolution of the GA took about 2 minutes and the GA worked flawlessly until stopped manually. Starting from a blade profile design, which was used in the 1960s, it took the GA roughly 250 steps of evolution to reach a profile with the same loss as that, which would be satisfactory to an experienced designer without optimisation tools. It took the GA about 1600 additional steps of evolution to reach an optimum design, which then had 19% less profile loss than the original design and 5% less profile loss than the manually improved design.

Van den Braembussche [40] from the Belgian Von Kármán Institute for Fluid Dynamics made several approaches in what he calls "Numerical Laboratories", which means using numerical design and analysing tools for turbomachinery bladings. He identified two reasons for that: First, the difficulties when studying complex geometries, where mea-

---

<sup>17</sup>Profile loss coefficient =  $\frac{P_{t0} - P_{t1}}{P_{t0}} \cdot 100$

## 1 Introduction

surements might even not be possible at all, and second, the abundance of information. For the second reason he pointed out, that even with the results of 3D Navier Stokes calculations, which provide informations about a limited number of physical quantities at a large number of grid points, informations about how to modify the geometry to improve the performance cannot be given by those results. Not willing to use evolutionary algorithms alone, as they seemed too time-consuming when using Navier Stokes Solvers for each step of the evolutionary path, Van den Braembussche developed a rapid evaluation system, which allowed them to make fast approximative calculations for 2D potential flow analysis, by taking into account, that viscous effects could not be predicted by their inviscid method. The results of this approximation were then evaluated by using full Navier Stokes solvers. Storing all the results in a database gave them the tools to develop an Artificial Neural Network (ANN), which was then used to predict the performance of a new blade design. Van den Braembussche points out two advantages of the ANN: First, the ANN does not need to have hypotheses about the relations between input (new blade design) and output (performance of the new design), and, second, the time for training the ANN is considerably lower than the time needed for a Navier Stokes solver. Another advantage, Van den Braembussche saw for this method, is the ability, to do multi-objective-optimisations in one run by defining a global objective function (OF), which imposes penalties for all constraints, that are violated. A possible global objective function would be for example:

$$OF = P_{Meca} + P_{Perf} + P_{Geom} + P_{\xi} + P_{Mach} \quad (1.2)$$

The P-values denote the penalties, that would be imposed, when violating the constraints for mechanical requirements ( $P_{Meca}$ ), for aerodynamical requirements ( $P_{Perf}$ ), for geometrical requirements ( $P_{Geom}$ ), for non optimum performance ( $P_{\xi}$ ) and for non-optimum Mach number distribution ( $P_{Mach}$ ).

Lampart and Yershov [20] performed 3D shape optimisations for several turbomachine applications. They used a code called "Optimus" to optimise stator-rotor stages. Total loss, with the exit kinetic energy also considered as loss was used as objective function, which was minimised. According to Lampart and Yershov, "Optimus" provides the opportunity to oppose constraints and penalties for leaving those constraints for the objective function. The CFD calculations were done with a 3D RANS solver, which used the code FlowER and a modified algebraic turbulence model of Baldwin and Lomax without wall function.

First, a highly loaded gas turbine stage was optimised, with six geometrical parameters, viz.

- stator and rotor blade stagger angle,
- stator and rotor linear twist angle, and
- stator blade linear lean and sweep angle,

## 1 Introduction

chosen for variation during the optimisation process. The optimisation resulted in a 0.7% decrease of mass-averaged kinetic energy loss, reducing the average stage reaction from 40% to 34%. Favourable effects on the flow patterns in the rotor were observed, as an oblique shock wave on the suction side was significantly reduced in intensity and the stagnation zone behind this shock wave was eliminated. In the stator, transsonic/supersonic velocities at the root were reduced due to increased reaction there.

Second, a HP steam turbine impulse stage was optimised in a two-stage optimisation process. In the first step, stator and rotor blade numbers and stator and rotor stagger angles were optimised with a 1D-based procedure, yielding in an intermediate geometry. In the second step, rotor blade linear twist angle and stator blade compound lean displacements at hub and tip were optimised by means of 3D calculations. It should be mentioned, that for the optimisation process, only coarse grids of 100000 cells were used. Verifying calculations for the results were done at the end of the optimisation with a grid of 800000 cells. Stage efficiency was improved by 0.4% in the first step, and by another 0.4% in the second step, yielding 0.8% in total.

Third, a LP exit stage of a steam turbine was optimised, using the same tools as above. This time, 8 geometrical parameters were varied for optimisation, namely

- stator straight circumferential lean,
- stator compound lean at root (2 parameters),
- stator straight axial sweep,
- stator compound sweep at tip (2 parameters), and
- stator and rotor stagger angles.

The optimisation for the stage was done at nominal operating conditions, however, the results of the optimisation were also checked for high-load mass flow rate and low-load mass flow rate, as this kind of stage usually operates over a wide range of flow rates. Again, the optimisation was carried out with a rather coarse grid, for verifying calculations a refined grid with 600000 cells was used. Overall stage losses were improved by 1.8% for nominal operating conditions, for low-load mass flow rates this improvement reached 1.2%, whereas for high-load mass flow rates the improvement was only 0.9%.

To get some understanding of what results can be expected of the application of CFD, and what cannot be expected to be solved by CFD, Horlock and Denton [14] in 2005 took a closer look on some early design practices using CFD. They compared the concepts and results of empirical formulas of the 1950-1970 periods, i.e. those developed by Lakshminarayana, and the results, that modern CFD delivers for selected problems. The field of blade-to-blade flows, secondary flows, through-flow methods and clearance flows, and the approaches made to better understand those phenomena, were examined. For flow deviation it turned out, that the empirical formulas used were strikingly simple, as they only seemed to be derived from pitchwise averaged equations of continuity and momentum. Nevertheless no convincing semi-analytical derivations for those formulas could be found by Horlock and Denton. So they concluded, that no alternative

to full numerical computations existed, if deviation was to be obtained accurately. In addition, having compared the results of various CFD approaches to this problem, they estimated the inclusion of viscous effects and fully turbulent flow as inevitable in order to get reasonable results for cascades. The limits of CFD to predict secondary flows are, according to Horlock and Denton, turbulence and boundary layer transition modelling when trying to predict viscous effects. For this reason they concluded, that it is more promising to use CFD for turbines rather than for compressors, as viscous effects are less dominant there. However, to get accurate results from CFD, the inlet boundary layer profiles on the endwalls must be known as exactly as possible. Usually, data about this is available for cascades, but not for real turbines. Horlock and Denton backed up their conclusion by comparing CFD results and experimental results for a cascade tested by Harrison [9]. They made inviscid CFD calculations with the measured inlet boundary layer, viscous calculations with no boundary layer and viscous calculations with inlet boundary layer. It can be seen quite clearly, that the inclusion of both, viscous effects and boundary layers, is necessary to obtain reasonable results. The final conclusion of Horlock and Denton was, that CFD provides very good insight into flow details, which cannot be measured experimentally at affordable costs, or, not at all. Still, they pointed out, it is important that the results of CFD be interpreted by skilled engineers with good physical understanding. According to Horlock and Denton, the end of experiments have not yet come and good experimental data, also from models and low-speed machines will be needed to further improve the current CFD methods.

Chen and Yuan [5] presented a numerical design tool for turbomachinery blade design in 2008. Facing the limits of Bézier curves and B-splines for the representation of turbomachine bladings, they used NURBS<sup>18</sup> as a design tool for geometries instead, which, in contrary to both of the former ones, is capable of representing conics for the leading and trailing edge shapes. NURBS was used for the stacking of the blade profiles as well as for the profile shapes. In addition, Chen and Yuan used several optimisation techniques such as genetic algorithms (GA), adaptive simulated annealing (ASA) and others, which were provided by the commercial optimisation software ISIGHT<sup>©</sup> in an integrated way, which means, that their design system chose by itself the most promising optimisation strategy, be it a robust exploratory algorithm or a highly efficient numerical method. To generate the geometry and the CFD grid, MATLAB<sup>©</sup> and an in-house code (AUTOGRID) were used. The numerical calculations were done with an in-house code as well. Testing of the aerodynamic optimization system was done numerically by optimising the following:

- a) Subsonic Turbine Blade
- b) Transsonic Turbine Blade
- c) Subsonic Turbine Stage

For test case "a" the optimised blade showed an increase of isentropic efficiency<sup>19</sup> of 0.58%. For test case "b" an efficiency improvement of 0.84% was reached, whereas for test case "c" the isentropic efficiency was increased by 0.5%.

---

<sup>18</sup>Non-Uniform Rational B-Spline

<sup>19</sup> $\eta' = \frac{w_1^2}{w_{1s}^2}$ , compare [26]

## 2 Experimental Calibration of the initial Configuration

No amount of experimentation  
can ever prove me right; a single  
experiment can prove me wrong.

---

*(Albert Einstein,  
German Physicist)*

The experiment for calibrating the following CFD calculations were done in the linear cascade wind tunnel of the Institute for Thermodynamics and Energy Conversion of the Vienna University of Technology. Large parts of the description of the used equipment and methods were taken from [46].

### 2.1 Wind Tunnel and Measurement Instrumentation

The wind tunnel used is a low speed wind tunnel. Air at ambient conditions is sucked from the environment from outside the laboratory building into the windtunnel through a filter. This is done by means of an axial fan with variable inlet guide vanes (VIGV). The basic data of the fan is summarized in Tab. 2.1.

The air is directed through a diffuser and arrives at a flow straightener with a turbulence grid. Following that, the air is accelerated as it flows from the circular channel into a rectangular one of 150 mm x 566.9 mm cross-section, where the surface area decreases by a ratio of about 13.3:1. This is important to secure a steady flow with thin endwall boundary layers at the inlet of the blade cascade. Furthermore, the turbulent intensity,  $Tu$ , is reduced by the large acceleration of the flow. The maximum Mach number reached is about  $Ma \approx 0.2$ , so in accordance with Fig. 2.1 from [4], where  $\varrho_0$  is the density of a gas at rest and  $\varrho$  represents the density of the gas at the Mach number considered,

Volume flux, $\dot{V}$	2.7	m <sup>3</sup> /s
Pressure rise, $\Delta p$	15	mbar
Rotational speed, $n$	3000	min <sup>-1</sup>
Outer diameter	630	mm
Blade length at exit plane	60	mm

Table 2.1: Technical Data of Axial Fan of Windtunnel

## 2 Experimental Calibration of the initial Configuration

incompressible conditions may be assumed <sup>1</sup>, as the variation of the densities for Mach numbers smaller than 0.2 is less than 2%.

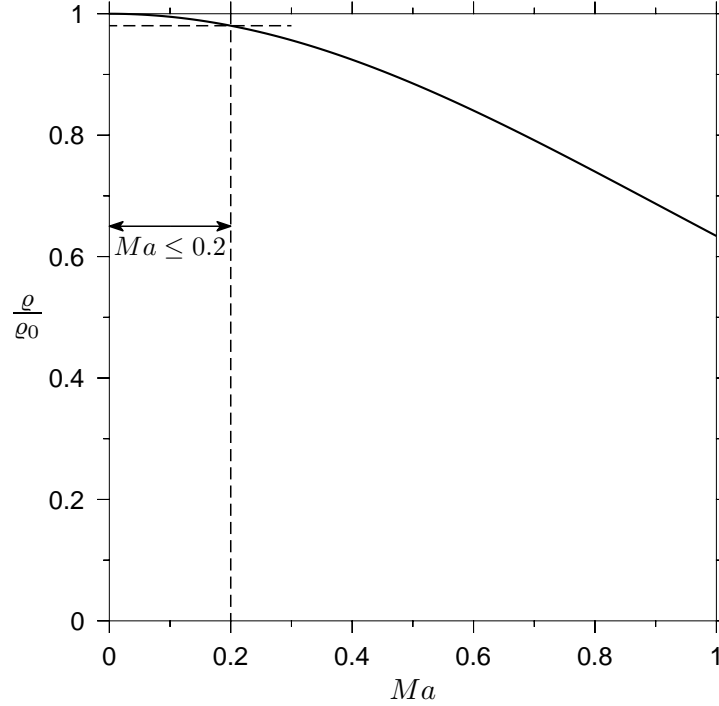


Figure 2.1: Variation of Density Ratio with Mach number

Figure 2.2 shows a sketch of the windtunnel.

The measuring setup is sketched in Fig. 2.3.

The HP 3852A unit is used for collecting data from the sensors and controlling the measuring process. It is equipped with a 24-channel highspeed-multiplexer-unit (HP 44711A), a 13-bit highspeed-voltmeter (HP 44702B), and a 16-channel digital output (HP 44724A). The voltages, delivered by the sensors Pt-100 (resistance thermometer) and the piezo-resistive pressure sensors (Honeywell), are recorded with the highspeed-multiplexer-unit and the highspeed-voltmeter-unit. The digital output controls the scanning box (FURNESS CONTROLS), which is used to switch between the different channels for measuring the different pressures of the setup. The DANTEC traversing unit was used to move the pressure probes in a translatic way parallel to the cascade exit plane. The exact position of the probe is secured by a step motor, which itself is controlled by the ISEL C10C-E/A controlling unit. All components are connected to a PC, which controls the whole process by making use of the software LabView 5.0<sup>©</sup> from National Instruments.

Nine blades were installed in a blade mounting box at the end of the windtunnel, which can be rotated along its base in order to be able to adjust the right inlet flow angle,

<sup>1</sup>  $\frac{\rho_0}{\rho} = \left(1 + \frac{\kappa-1}{2} M^2\right)^{\frac{1}{\kappa-1}}$  with air as ideal gas:  $\kappa = 1.4$

## 2 Experimental Calibration of the initial Configuration

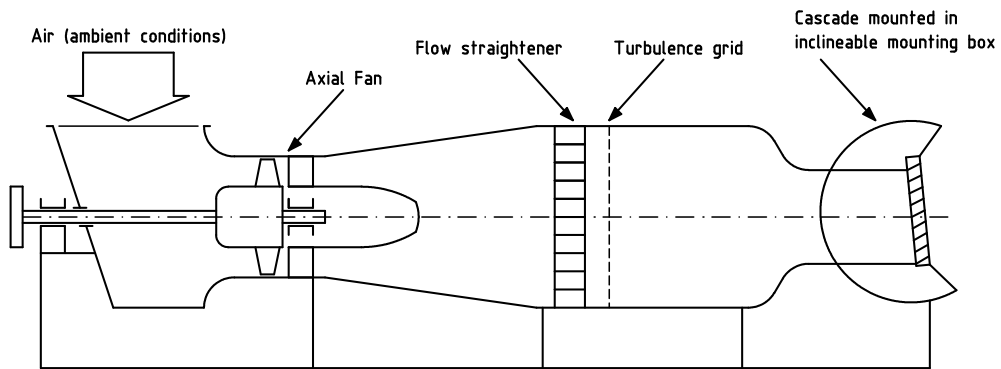


Figure 2.2: Sketch of Windtunnel

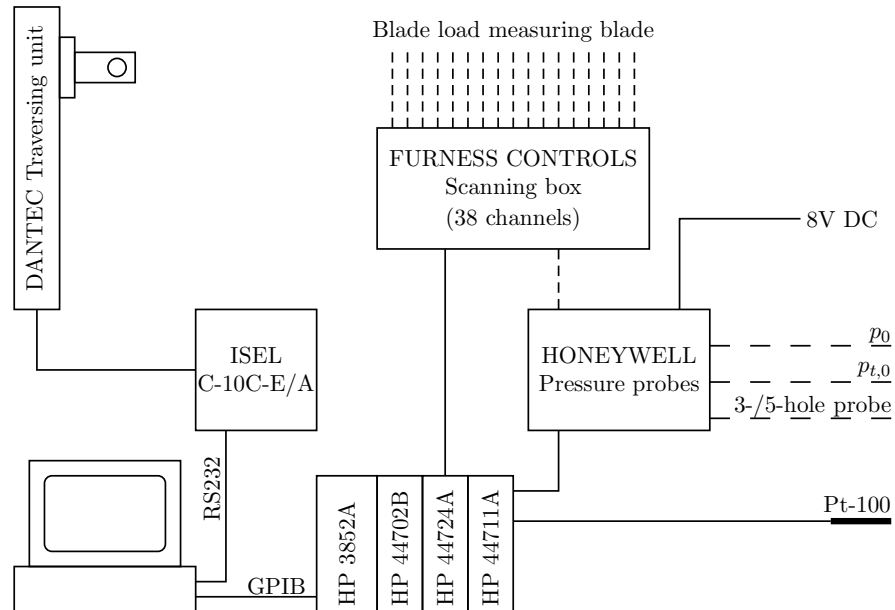


Figure 2.3: Sketch of Cascade Measuring Setup

here for incidence zero. The number of blades is limited by the maximum height of the windtunnel, the aspect ratio  $AR$  of the blade and the pitch-to-chord ratio. It is imperative to mount a sufficient number of blades to simulate periodic boundary conditions. To get well defined flow conditions at the most upper and lower blade of the cascade, two adjustable plates are positioned in a way, that there remain no gaps between the end of the plates and the leading edges of the blades.

For measuring the blade profile pressure, a special blade with milled grooves was used. The blade was made of aluminium. A sketch of the blade is presented in the appendix in Fig. A.2. 38 thin plastic tubes with 1.9 mm outer and 0.8 mm inner diameter were placed inside the grooves, then the grooves were filled up with a 2-component-adhesive on methacrylat-basis. The excess adhesive was sanded off the blade, so that the blade got the same outer contour as the other blades of the cascade. The thin plastic tubes were led through the endwall of the cascade and connected with flexible silicon tubes to the scanning box (FURNESS CONTROLS). The scanning box, which allows to switch between the 38 input channels sequentially, was connected with its output to a piezo-resistive pressure sensor. Finally, holes of 0.3 mm diameter were drilled through the filled grooves from the surface of the blade into the thin plastic tubes at midspan ( $z = \frac{H}{2} = 75$  mm, compare Fig. 3.4). The pressure on the surface of the blade could then be measured at 38 measuring points.

## 2.2 Calibration of the Pressure Probes

The measurement in the measuring plane downstream and parallel to the cascade exit plane was done with pneumatic pressure probes. Before using such devices for measuring, they have to be calibrated. For this work this was done with a so-called freestream wind tunnel, which is also available at the laboratory of the institute.

### 2.2.1 Three-Hole Pressure Probe

A 2D measurement was undertaken downstream of the cascade with a so-called three-hole pressure probe. Figure 2.4 shows a sketch of such a device. The probe is traversed at half span along the exit of the cascade at  $x = 80$  mm, which is about 1.293 times the axial chord length  $b$  (compare Fig 2.11 and Tab. 2.2). The shaft of the probe has a diameter of 6 mm, the inner diameters of holes 1, 2 and 3 are 0.5 mm each. The head of the probe has a cross-sectional area of 0.8 mm x 2.4 mm, the front faces of holes 2 and 3 are inclined at an angle of  $60^\circ$  towards the axis of hole 1. The probe is mounted with its shaft in a special device, which allows to adjust the setup-angle of the probe accurately.

The probe was used in the so-called non nulling mode. This means, that the axis of hole 1 was not aligned in streamwise direction at every measuring point. The information about the angle, at which the axis of hole 1 was inclined towards the streamwise direction at every measuring point was determined by making use of the calibration information given

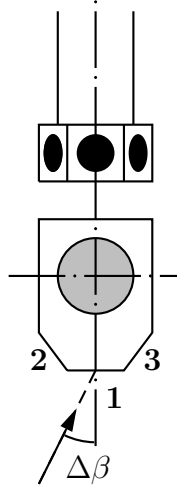


Figure 2.4: Sketch of Three-Hole Pressure Probe

in Fig. 2.5. In addition, the probe head was inclined at a well defined angle, the setup-angle  $\Delta\xi$ , away from the expected flow direction. The reason for that was, that the pressure differences expected to occur at holes 2 and 3 were of such small magnitude if the axis of hole 1 would have been aligned in streamwise direction, that it could possibly not have been determined clearly, if those differences did occur due to accuracy errors of the sensors used. This setup-angle has to be observed when evaluating the results of the experiment by either adding or subtracting the setup-angle to the yaw angle, solely depending on the coordinate system used for the evaluation.

The probe was calibrated at a Reynolds number of

$$Re = \frac{w \cdot l}{\nu} \approx 11250, \quad (2.1)$$

as this was the Reynolds number expected to be reached in the experiment with the cascade. The Reynolds number was calculated with the width of the probe head ( $l = 2.4$  mm, see Fig. 2.4 and explanation above) and the kinematic viscosity

$$\nu = \frac{\mu}{\rho}$$

where  $\mu$  denotes the dynamic viscosity and was calculated with Sutherland's law

$$\frac{\mu}{\mu_0} = \left( \frac{T}{T_0} \right)^{\frac{3}{2}} \cdot \frac{T_0 + S}{T + S} \quad (2.2)$$

according to [44]. The result of the calibration process of the probe are three calibration

## 2 Experimental Calibration of the initial Configuration

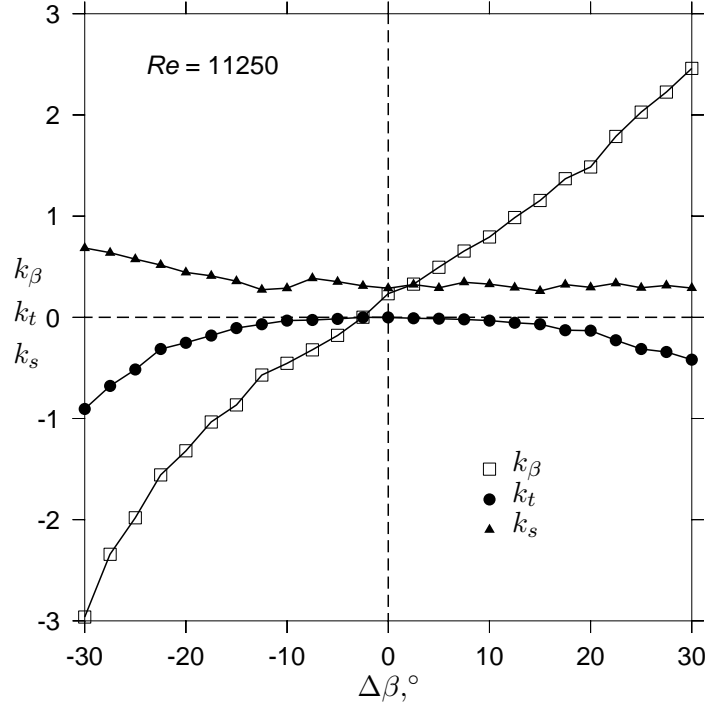


Figure 2.5: Calibration Data of the Three-Hole Pressure Probe: Yaw Angle Coefficient  $k_\beta$ , Total Pressure Coefficient  $k_t$ , Static Pressure Coefficient  $k_s$

coefficients, namely  $k_\beta$ ,  $k_t$  and  $k_s$ . Treaster and Yocum [38] defined four calibration coefficients for five-hole pressure probes (compare Chap. 2.2.2), adapted for the three-hole pressure probe  $k_\beta$ ,  $k_t$  and  $k_s$  read as follows:

$$k_\beta = \frac{p_2 - p_3}{p_1 - \bar{p}} \quad (2.3)$$

$$k_t = \frac{p_1 - p_t}{p_1 - \bar{p}} \quad (2.4)$$

$$k_s = \frac{\bar{p} - p}{p_1 - \bar{p}} \quad (2.5)$$

$p_i$  denominates the pressure, that can be measured at hole  $i$ ,  $p_t$  the total pressure, and  $p$  the static pressure. The mean pressure  $\bar{p}$ , is defined as

$$\bar{p} = \frac{p_2 + p_3}{2}. \quad (2.6)$$

Then,  $k_\beta$ , the yaw angle coefficient, gives an unambiguous relation between the yaw angle  $\Delta\beta$ , shown in Fig. 2.4 and the pressure difference at holes 2 and 3. Having identified

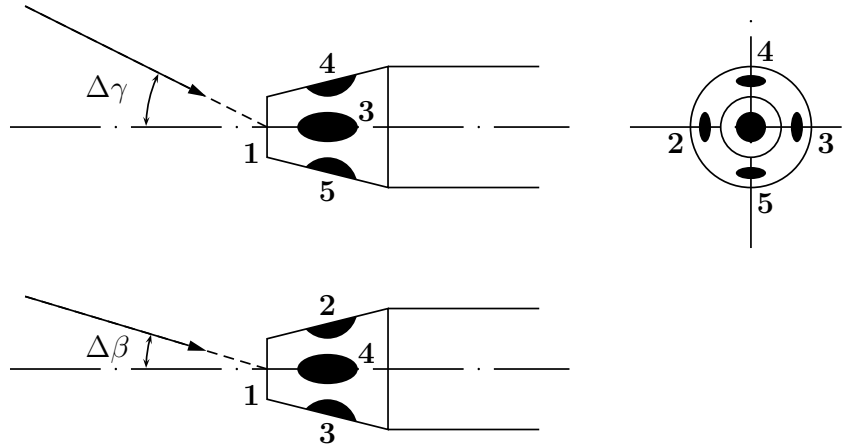


Figure 2.6: Sketch of Five-Hole Pressure Probe

the yaw angle, the total pressure and the static pressure can be found out by using the calibration diagram given in Fig. 2.5. Assuming incompressible flow, which is acceptable, as demonstrated above, the local velocity at the head of the pressure probe can be determined.

### 2.2.2 Five-Hole Pressure Probe

To measure the 3D flow field downstream of the cascade, a five-hole pressure probe was used. A sketch of this device is shown in Fig. 2.6. The shaft of the probe, which is not shown here, has a diameter of 6 mm, the probe itself is conical with a cone angle of  $60^\circ$ . The diameter of the probe head is 3 mm, again the holes have an inner diameter of 0.5 mm. The yaw angle  $\Delta\beta$  and the pitch angle  $\Delta\gamma$  can also be seen in Fig. 2.6. The yaw angle is the angle between the projection of a velocity vector of the flow in the plane of holes 1, 2 and 3 and the direction of the axis of hole 1. The pitch angle is the angle between the projection of a velocity vector of the flow in the plane of holes 1, 4 and 5 and the direction of the axis of hole 1.

For the same reasons as mentioned above for the three-hole pressure probe, the Reynolds number for the five-hole pressure probe was set to a value, that could be expected for the experiment with the cascade. As the geometry of the probe is slightly different from that of the three-hole probe, the Reynolds number also slightly differs, so here it was set to  $Re = 13600$ , again calculated according to Eq. 2.1, with  $l = 3$  mm now being the diameter of the probe head (see Fig 2.6 and explanations above). The result of the calibration of the five-hole pressure probe were three calibration diagrams, one for  $k_\beta$  vs.  $k_\gamma$  (Fig. 2.7), one for  $k_t$  (Fig. 2.9), and one for  $k_s$  (Fig. 2.10).

The different calibration coefficients are calculated as

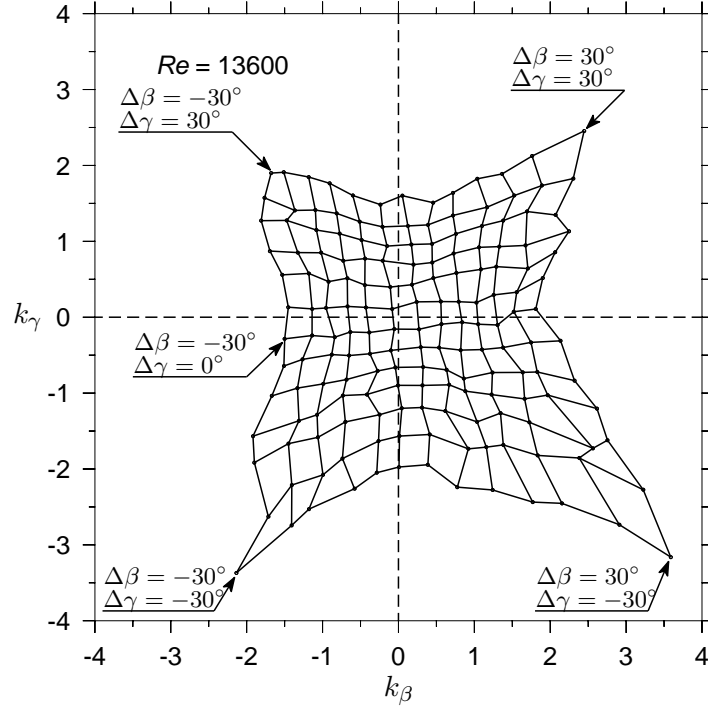


Figure 2.7: Calibration Data of the Five-Hole Pressure Probe: Pitch Angle Coefficient  $k_\beta$  vs. Yaw Angle Coefficient  $k_\gamma$

$$k_\beta = \frac{p_2 - p_3}{p_1 - \bar{p}} \quad (2.7)$$

$$k_\gamma = \frac{p_4 - p_5}{p_1 - \bar{p}} \quad (2.8)$$

$$k_t = \frac{p_1 - p_t}{p_1 - \bar{p}} \quad (2.9)$$

$$k_s = \frac{\bar{p} - p}{p_1 - \bar{p}} \quad (2.10)$$

with  $\bar{p}$  now being defined as

$$\bar{p} = \frac{p_2 + p_3 + p_4 + p_5}{4}. \quad (2.11)$$

When measuring the 3D flow downstream of the cascade, again the probe was traversed along the exit plane of the cascade at an axial position of  $x = 80$  mm, which is equal to 1.293 times the axial chord length  $b$ . Doing this, 5 different values of pressure were measured for each point examined in the flow field, namely  $p_{1..5}$ . For the same reasons

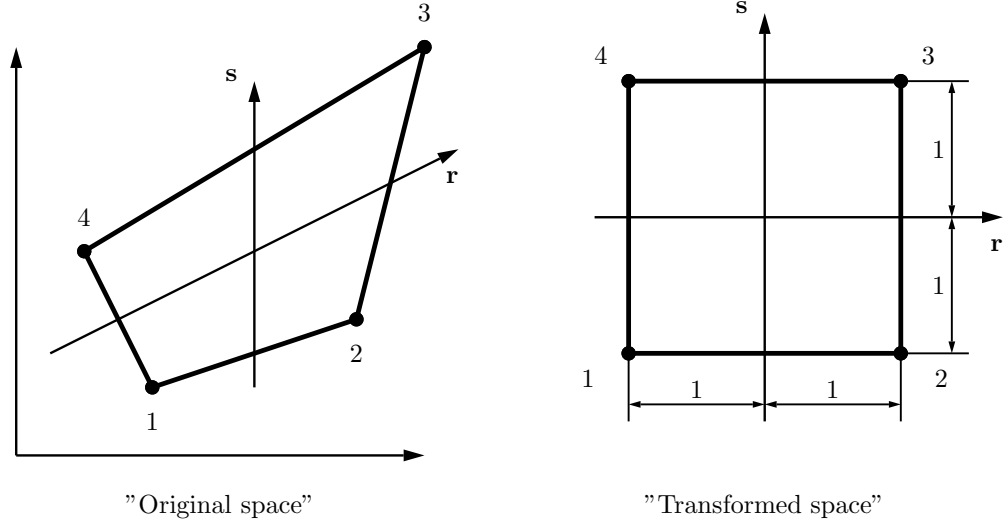


Figure 2.8: Bilinear Interpolation: Element with 4 Nodes

as explained above for the three-hole probe, the five-hole probe is used in the non nulling mode too. With the five determined pressures for each measuring point,  $k_\beta$  and  $k_\gamma$  were determined with Eq. 2.7 and Eq. 2.8 first. Figure 2.7 was then used to determine  $\Delta\beta$  and  $\Delta\gamma$ . The trapezoid, where the intersection of the  $\Delta\beta$ - and  $\Delta\gamma$ -values was situated (intersection point "P") was then transformed into a quadrat with side length 2 with a so-called bilinear interpolation (Fig. 2.8).

To determine the exact position of "P" in the relevant quadrilateral, the method of bilinear interpolation for a 4-node element is used with the following ansatz:

$$\vec{\varphi} = \begin{pmatrix} \varphi_1(r, s) \\ \varphi_2(r, s) \\ \varphi_3(r, s) \\ \varphi_4(r, s) \end{pmatrix} = \begin{pmatrix} \frac{1}{4}(1-r)(1-s) \\ \frac{1}{4}(1+r)(1-s) \\ \frac{1}{4}(1+r)(1+s) \\ \frac{1}{4}(1-r)(1+s) \end{pmatrix} \quad (2.12)$$

$\varphi_{1..4}$  represent functions for the 4 corner nodes of the quadrilateral in the transformed space. The coordinates of any arbitrary point "P" can then be described by

$$\begin{aligned} x_P &= \sum_{i=1}^4 \varphi_i(r, s) x_i \quad \text{and} \\ y_P &= \sum_{i=1}^4 \varphi_i(r, s) y_i . \end{aligned} \quad (2.13)$$

2 Experimental Calibration of the initial Configuration

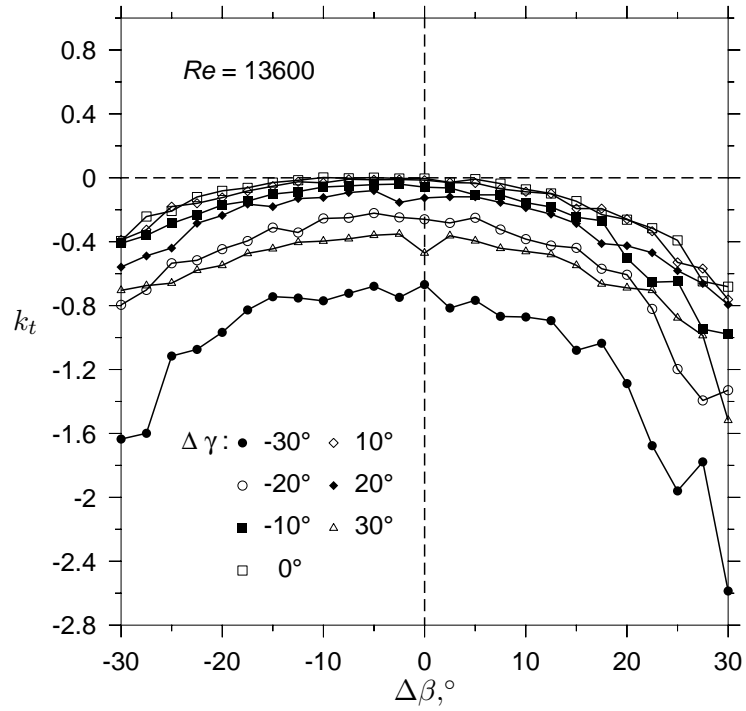


Figure 2.9: Calibration Data of the Five-Hole Pressure Probe: Total Pressure Coefficient  $k_t$

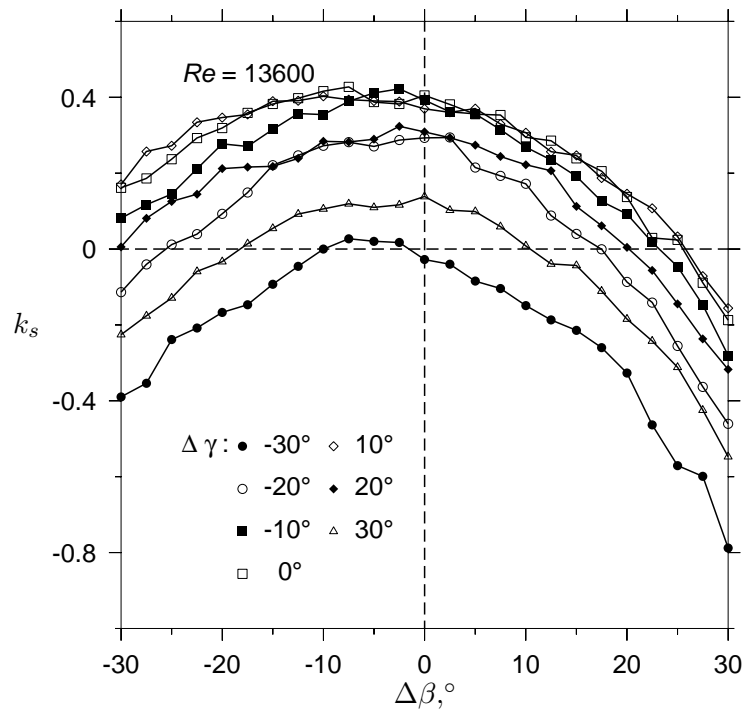


Figure 2.10: Calibration Data of the Five-hole Pressure Probe: Static Pressure Coefficient  $k_s$

Equation 2.13 can be solved for  $r$  and  $s$  with any suitable equation solving method. Having determined  $r$  and  $s$ , the relevant quadrilateral in the calibration grid of  $k_\beta$  vs.  $k_\gamma$ , and therefore the parameters  $\Delta\beta$  and  $\Delta\gamma$  at the edges of the quadrilateral, the angles  $\Delta\beta$  and  $\Delta\gamma$  for "P" can be determined. With Eq. 2.9 and Fig. 2.9 the total pressure of the measuring point can be determined. Using Eq. 2.10 and Fig. 2.10 the static pressure can be determined. Incompressible conditions assumed this allows to calculate the local velocity at the probe head in addition to the local direction of the flow.

## 2.3 Inlet Conditions

The conditions upstream of the blade row were measured at  $x = -180$  mm (static pressure) and at  $x = -225$  mm (total pressure, and temperature). This is equal to  $-2.91 \cdot b$  and  $-2.63 \cdot b$  respectively, so it could be expected, that the flow was not influenced by the cascade, which was situated downstream at  $x = 0$ . To measure the static pressure, a hole of 2 mm diameter in the sidewall of the windtunnel was used to connect a tube which was further connected to a piezo-resistive differential pressure sensor. The total pressure was measured with a Pitot tube with 3 mm outer and 1 mm inner diameter. The temperature of the flow upstream of the cascade was measured with a Pt-100 temperature sensor. The total and the static pressure were measured at  $z = \frac{H}{2}$  (half span). The difference between total and static pressure is the dynamic pressure, taking into account the assumption of incompressible flow, the velocity of the flow could be calculated with

$$w_0 = \sqrt{\frac{2 \cdot (p_{t0} - p_0)}{\varrho(T)}},$$

where  $\varrho(T)$  represents the temperature dependence of the density.

## 2.4 Blade and Operating Data of the Investigation

The blades used were made of aluminium. The 2D profile of the model blades used in real size is depicted in A.1. The basic geometric data of the blades and the cascade is figured in Tab. 2.2 and Fig. 2.11. The 2D profile coordinates were taken from Perdichizzi and Dossena [29].

The main flow data is summarized in Tab.2.3.

The blade Reynolds number in this setup was fairly low to be compared with the conditions in the high-pressure sections of a real steam turbine, where it is about  $Re \cong 15 \cdot 10^6$

---

<sup>2</sup>The outlet blade angle is the angle between the tangent of the camber line at the trailing edge of the blade and the blade exit plane.

<sup>3</sup>calculated with the chord length  $c$  of the blade and the cascade outlet velocity

## 2 Experimental Calibration of the initial Configuration

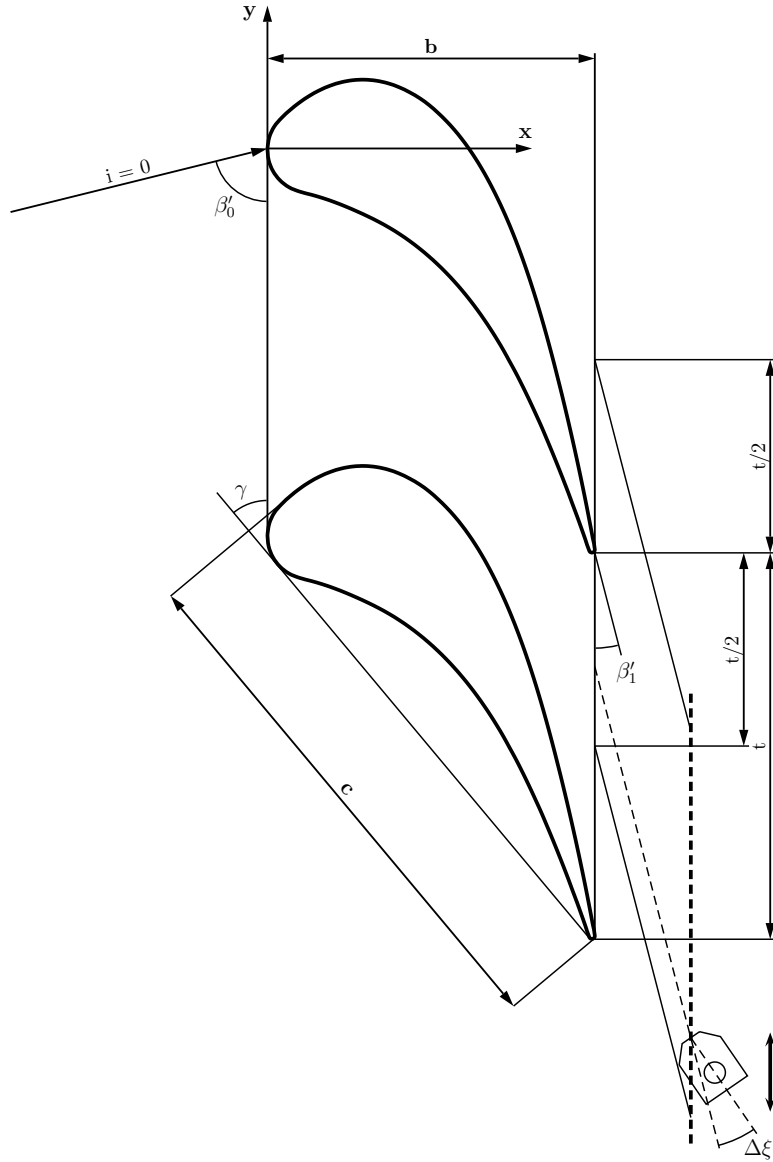


Figure 2.11: Sketch of Blade Cascade

Chord length, $c$	100	mm
Axial chord length, $b$	61.85	mm
Pitch length, $t$	73	mm
Aspect ratio, $AR = \frac{H}{c}$	1.5	
Inlet blade angle, $\beta'_0$	76.1	deg
Outlet blade angle <sup>2</sup> , $\beta'_1$	14.5	deg
Blade turning angle, $\Delta\beta'$	89.4	deg
Stagger angle, $\gamma$	39.9	deg

Table 2.2: Cascade Geometric Data

## 2 Experimental Calibration of the initial Configuration

Freestream flow velocity at cascade inlet, $w_0$	$\cong$	20	m/s
Boundary layer thickness at endwalls at inlet, $\delta$		25	mm
Flow velocity at measuring plane, $w_1$	$\cong$	75	m/s
Blade Reynolds number <sup>3</sup> , $Re$	$\cong$	$4.2 \cdot 10^5$	
Freestream turbulence intensity, $Tu$	$\cong$	5	%

Table 2.3: Main Flow Data for the Experiment

(compare [11]). However, in good agreement with Denton [7], it should be high enough for the losses in the cascade to be independent of the Reynolds number, as far as blades with typical relative surface roughness are considered. As far as the exit Mach number,  $Ma_1 \approx 0.21$ , is concerned, it can be said, that the conditions expected in high-pressure sections were fully matched in these low speed experiments, according to Havakechian and Greim [11]. The turbulence grid (see Fig. 2.2), which is located upstream in the windtunnel, produces a streamwise turbulence intensity  $Tu \cong 5\%$ . According to Mayle [24] the turbulence intensity  $Tu = 5 - 10\%$  in the free stream region of an axial turbomachinery environment, so the value in this experiment was rather at the low end of the range. For obvious reasons, the blade wakes of the upstream rotating blades, which have turbulence intensities  $Tu = 15 - 20\%$ , could not be modelled in a stationary linear cascade wind tunnel.

### 2.5 2D Measurement

The 2D measurement downstream of the cascade was done with the three-hole pressure probe described in Chap. 2.2.1. It was intended to get some information of the pressure loss in the wake of the cascade, the velocity of the flow behind the cascade, and therefore the potential of the blade to accelerate the flow. In addition it is important to get informations about the flow directions behind the cascade, i.e. the angles at which the flow exits the cascade. In an axial turbine the momentum of the accelerated flow from the stator blades is used in the following rotor blades to turn the rotor. The flow directions behind the stator row (and here the cascade) also determine the design of the following rotor blades, so it is important to know the appropriate flow angles at the inlet of the rotor blades to be able to determine the flow angles of the entering flow at design conditions at different spanwise positions of the blade.

The head of the probe was positioned at  $z = \frac{H}{2}$ , this means in the middle between the endwalls. It was traversed parallel along the exit plane of the cascade with the DANTEC traversing unit for one pitch length  $t = 73$  mm. It was chosen to accept the nominal outlet blade angle  $\beta'_1$  as the reference angle for the flow direction, so when the axis of hole 1 of the three-hole pressure probe is aligned in this direction, the probe setup-angle would be  $\Delta\xi = 0^\circ$ . As mentioned above, the pressures at holes 2 and 3 are expected to differ very little at a probe setup-angle of  $\Delta\xi = 0^\circ$ , so the probe was used with a probe setup-angle of  $\Delta\xi = 15^\circ$  (see Fig. 2.11). As already mentioned, the probe was used in the

## 2 Experimental Calibration of the initial Configuration

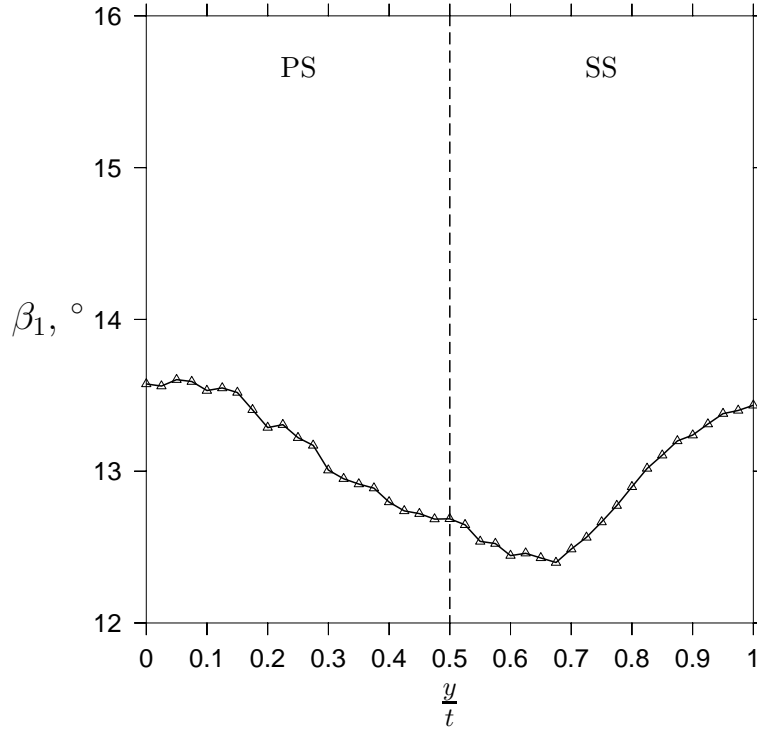


Figure 2.12: Pitchwise Exit Flow Angle  $\beta_1$  at Midspan with Three-Hole Pressure Probe (Probe Setup-Angle  $\Delta\xi = 15^\circ$ )

non nulling mode. 40 measuring points were recorded when traversing the pitch length, this means that one point was recorded every 1.825 mm.

Periodic conditions were checked by traversing the probe downstream of the whole cascade instead of just one pitch length. Evaluating and comparing the measurement values at corresponding points downstream of different blades <sup>4</sup> revealed, that with the setup chosen, periodic conditions were perfectly simulated.

Compared with the design outflow angle of  $14.5^\circ$  (compare [29]), the blade tested under the conditions mentioned above, shows slight overturning ( $\Delta\beta_1 \cong -1^\circ$ , see Fig. 2.12) at midspan. One reason may be, that Perdicchizzi and Dossena [29] used a different testing facility at different conditions for their investigation.

The acceleration of the flow behind the cascade can also be determined by using the three-hole pressure probe with

$$w_1 = \sqrt{\frac{2 \cdot (p_{t1} - p_1)}{\rho}}$$

The flow is accelerated about 3.8 times of the inlet flow velocity in the region of undis-

<sup>4</sup>The evaluation of this measurement is not presented in this work.

## 2 Experimental Calibration of the initial Configuration

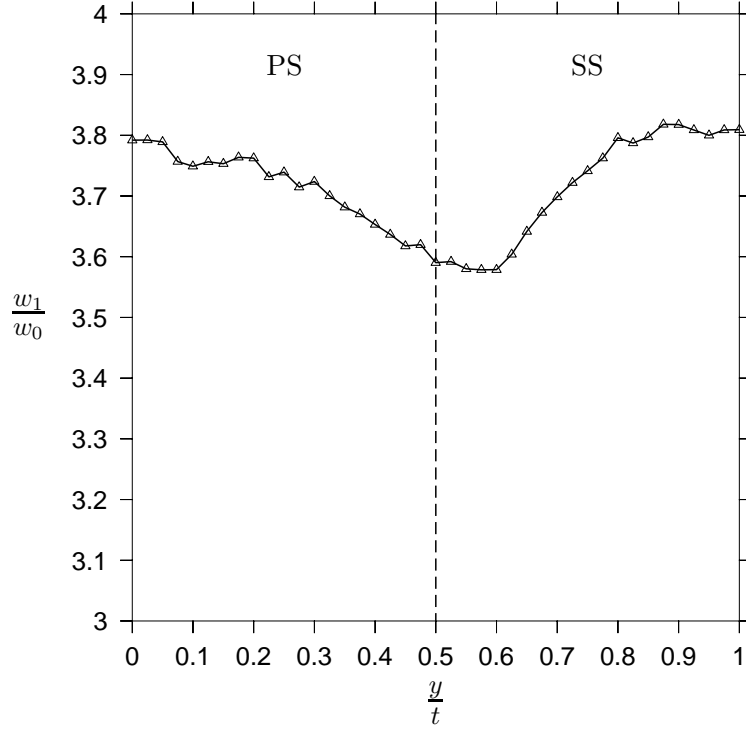


Figure 2.13: Cascade Exit Flow Velocity Ratio at Midspan with Three-Hole Pressure Probe (Probe Setup-Angle  $\Delta\xi = 15^\circ$ )

turbulent flow (compare Fig. 2.13). In the neighbouring regions of the blade the effect of the boundary layers, that are developed on the suction side and the pressure side of the blade, can be seen. The flow velocity is lower there. The minimum outflow velocity is reached in the wake of the blade, which can again be seen very clearly at  $\frac{y}{t} = 0.6$ .

The local total pressure coefficient  $C_{p,t1,MS}$ , defined as

$$C_{p,t1,MS} = \frac{p_{t1} - p_{t0}}{\frac{1}{2}\rho w_0^2} \quad (2.14)$$

is displayed in Fig. 2.14. It quantifies the loss of stagnation pressure, that is produced by the cascade. The wake of the cascade can be determined quite well at  $\frac{y}{t} \cong 0.6$ , where the loss reaches a maximum. Theoretically, the total pressure coefficient should be zero in the freestream region of the flow channel between the blades, as no losses occur. This is the case for  $0 \leq \frac{y}{t} \leq 0.3$  on the pressure side and for  $0.87 \leq \frac{y}{t} \leq 1$  on the suction side, where  $C_{p,t1,MS}$  is around zero, so it is assumed, that between those two regions, losses are produced.

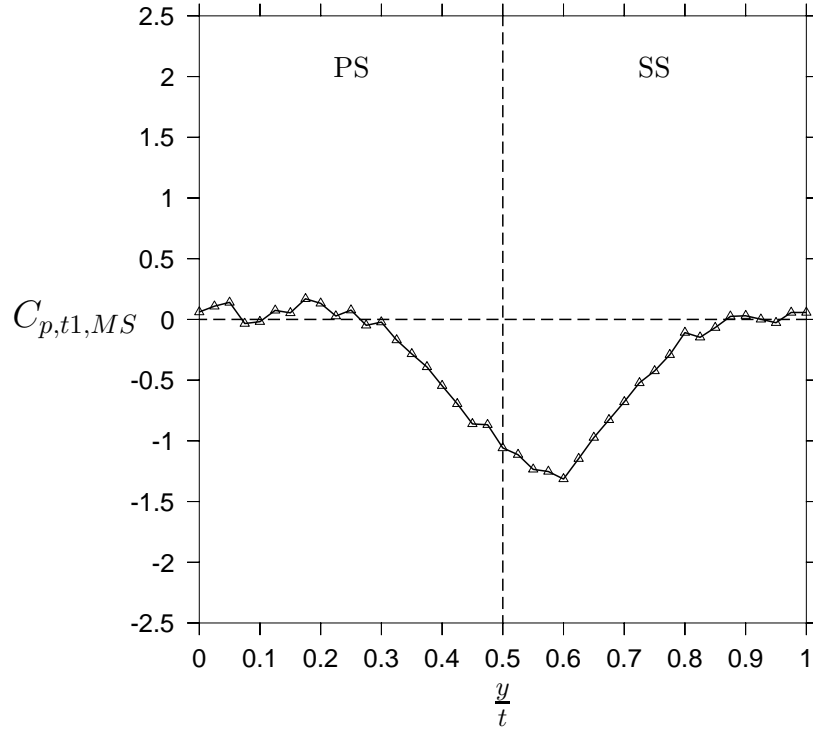


Figure 2.14: Total Pressure Coefficient  $C_{p,t1,MS}$  at Midspan with Three-Hole Pressure Probe (Probe Setup-Angle  $\Delta\xi = 15^\circ$ )

## 2.6 3D Measurement

In order to get some more insight information about the flow downstream of the cascade, measurements were executed with a five-hole pressure probe, described in Chap. 2.2.2. Beginning from  $z = 5$  mm, one pitch length  $t$  was scanned by traversing the probe with the DANTEC traversing unit, recording 40 measuring points. Then the probe was moved 5 mm in spanwise direction towards midspan and again one pitch length  $t$  was scanned in 40 steps. This was done until midspan was reached, so in total  $15 \times 40 = 600$  measuring points were recorded. Again the probe was inclined at a setup-angle of  $\Delta\xi = 15^\circ$  from the flow direction of the reference angle  $\beta_1'$ . The gridded data was used to present contourplots of important flow characteristics downstream of the cascade. The total pressure coefficient  $C_{p,t1}$  shows the occurrence and the size of losses, that occur downstream the cascade. The two flow angles,  $\beta_1$  and  $\gamma_1$  give a good picture of the occurrence and the behaviour of secondary flow downstream of the cascade.

Figure 2.15 and Fig. 2.16 present the flow angles downstream of the cascade. The pitchwise flow angle  $\beta_1$  (Fig. 2.15) at midspan is comparable to the measurements with the three-hole probe, although slightly lower. Towards the endwall regions, increasing overturning was observed, which is caused by the boundary layers and was to be expected.

The spanwise deviation of the flow direction from the pitchwise flow direction, the span-

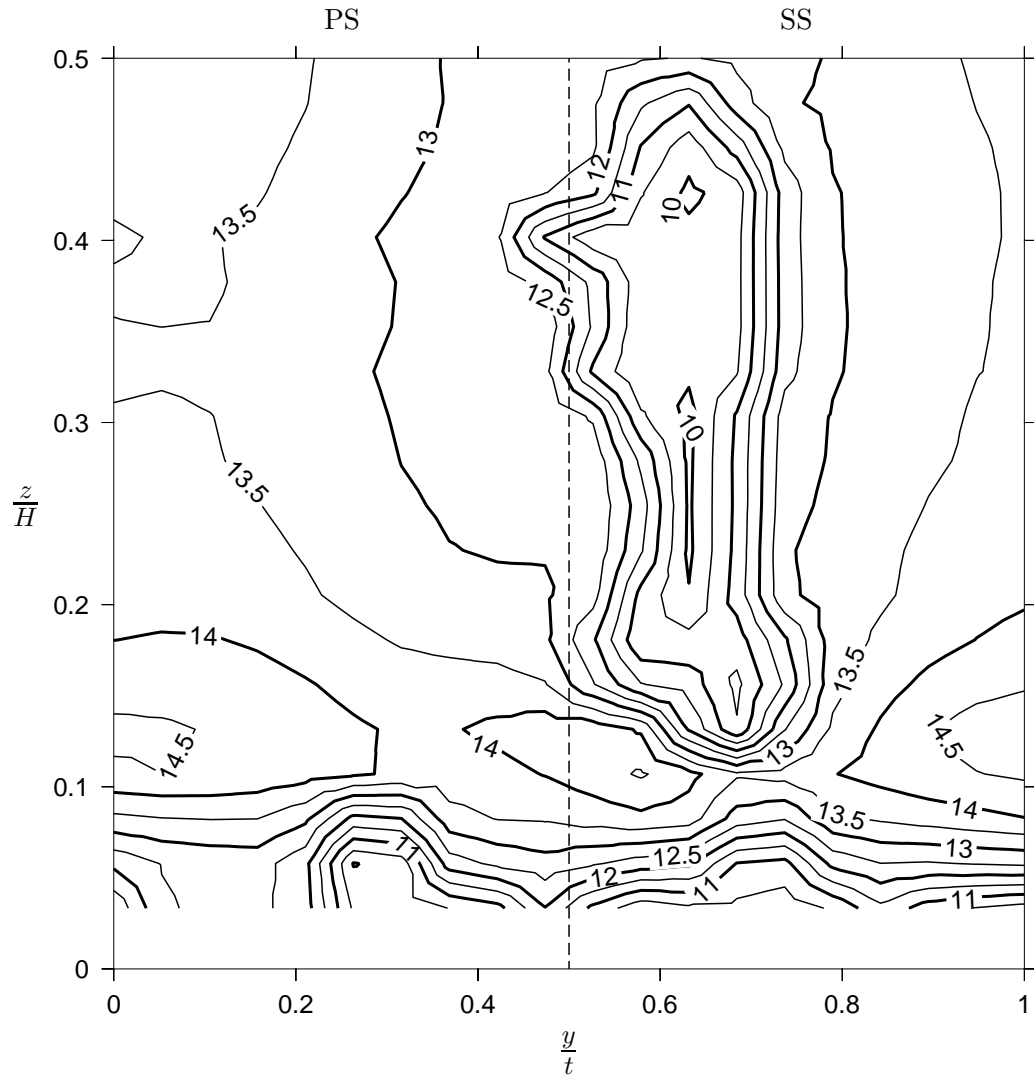


Figure 2.15: Pitchwise Exit Flow Angle  $\beta_1$  with Five-Hole Pressure Probe (Probe Setup-Angle  $\Delta\xi = 15^\circ$ )

wise flow angle  $\gamma_1$ , which is displayed in Fig. 2.16, has to be evaluated together with the diagram of the pitchwise flow angle  $\beta_1$  (Fig. 2.15): Combining both pictures leads to the conclusion, that the passage vortex can be detected quite clearly, as the flow flows in an upward direction (away from the endwall) when approaching the suction side of blade from the free-stream-region, also in regions near the endwall. On the other side, the pressure side of the blade, the flow flows in a downward direction towards the endwall. Together with  $\beta_1$  the flow is curled clockwise, which is consistent with the model of the passage vortex, which is very common and meanwhile widely undisputed in turbomachinery research.

In Fig. 2.17 the total pressure coefficient  $C_{p,t1}$  is plotted as a contour plot for  $0 \leq \frac{z}{H} \leq 0.5$  and  $0 \leq \frac{y}{t} \leq 1$ . The position of the loss core, which is the region where the highest losses occur (presumably produced by secondary flows), is located at  $\frac{y}{t} = 0.6$  and at around 15% of the blade height. This is consistent with current loss- and secondary-flow-models (e.g. [21] and [35]). At midspan ( $\frac{z}{H} = 0.5$ ) the results with the five-hole probe can be compared with the results of the three-hole probe. Again, the wake of the blade can be seen in the same region of  $\frac{y}{t} \cong 0.6$ , the level of  $C_{p,t1} \cong -1$  is about the same as measured with the three-hole probe. Furthermore the influence of the endwall boundary layers can be seen, as the losses grow in the flow regions near the endwall. Outside the regions described above, the freestream experiences no disturbances, therefore no losses are produced in those regions.

## 2.7 Profile Pressure Measurements

The result of the blade profile pressure measurement is presented in Fig. 2.18, where the static pressure coefficient

$$C_p = \frac{p - p_0}{p_{t0} - p_0} = \frac{p - p_0}{\frac{1}{2}\rho w_0^2} \quad (2.15)$$

is plotted along the normalized blade length  $\frac{x}{b}$ .

$p$  denotes the pressure on the blade surface, the other values are the ones measured at the inlet. At the stagnation point the value of  $C_p$  should therefore theoretically be 1, which is not the case here. It is suspected, that this arises from the fact, that there is no measuring point exactly at the stagnation point.

The distance between the measuring points on the suction and the pressure side represents the blade loading at the respective position. It can be seen quite clearly, that the blade is strongly aft-loaded, the minimum pressure is reached at an axial position of  $\frac{x}{b} \approx 0.77$ . After that position, the flow is decelerated considerably on the suction side. According to Weiss and Fottner [43], aft-loaded blade cascades tend to show different spanwise distributions of loss coefficient and different flow angle distributions than front-loaded blade cascades in the cascade exit planes, even with overall secondary loss coefficients of

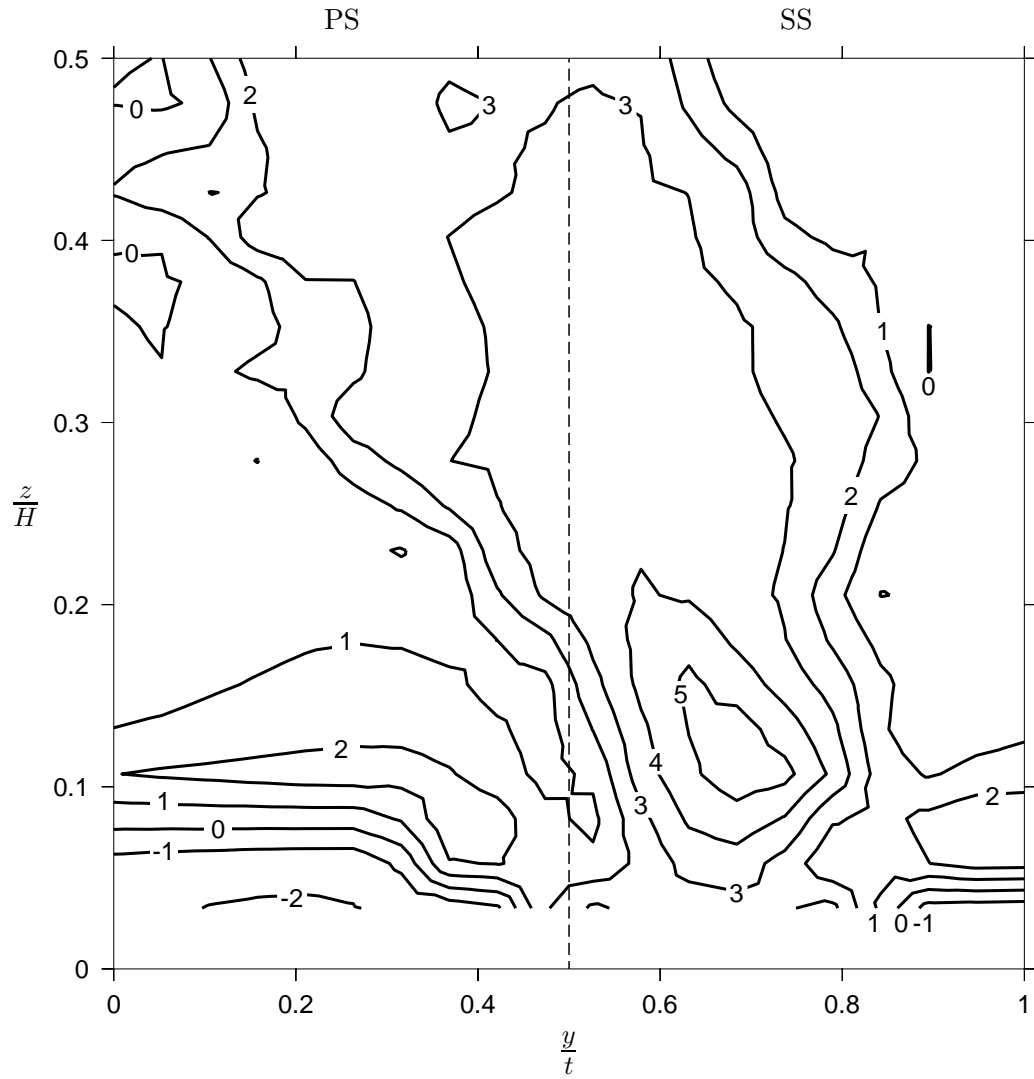


Figure 2.16: Spanwise Exit Flow Angle  $\gamma_1$  with Five-Hole Pressure Probe (Probe Setup-Angle  $\Delta\xi = 15^\circ$ )

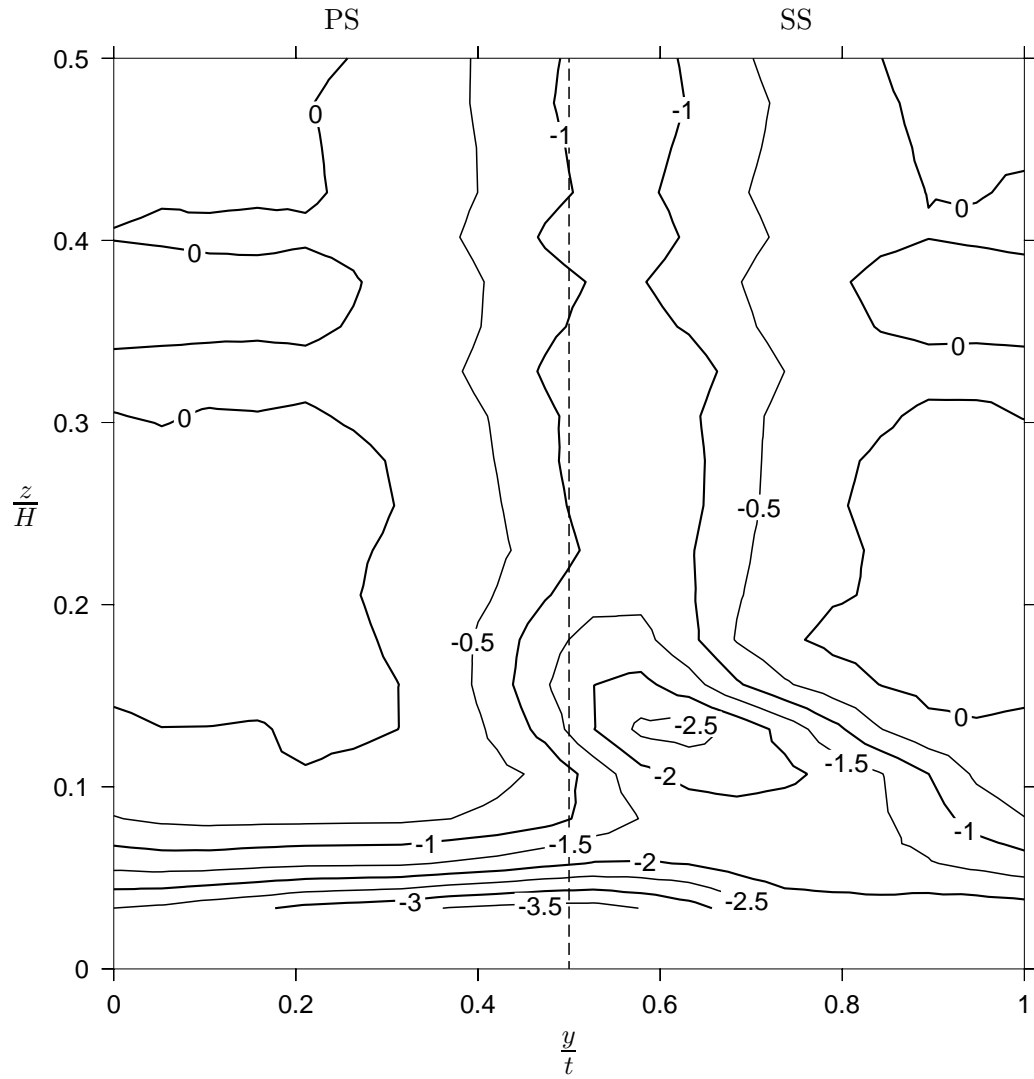


Figure 2.17: Total Pressure Coefficient  $C_{p,t1}$  with Five-Hole Pressure Probe (Probe Setup-Angle  $\Delta\xi = 15^\circ$ )

## 2 Experimental Calibration of the initial Configuration

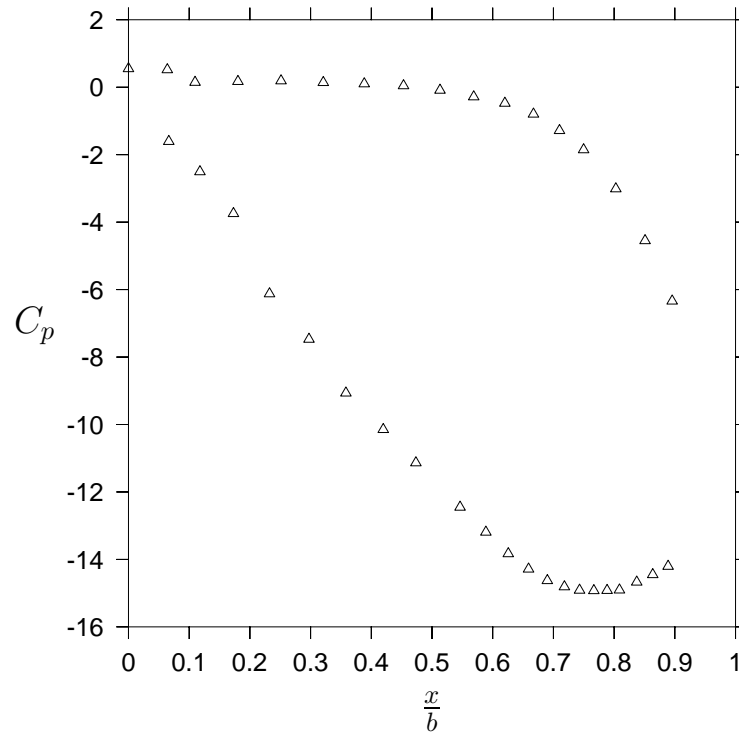


Figure 2.18: Static Profile Pressure Coefficient  $C_p$  at Midspan

equal magnitude. In their experiment, these different spanwise distributions disappeared due to mixing processes further downstream. However, in this experiment, the measuring plane was at  $\frac{x}{b} = 1.3$  (compare Figs 2.15, 2.16 and 2.17), whereas in their experiment it was at  $\frac{x}{b} = 1.5$ .

## 3 Optimisation

Never tell people how to do things. Tell them what to do and they will surprise you with their ingenuity.

---

(George S. Patton,  
U.S. Army General)

### 3.1 Comparison of four widely used Optimisation Techniques

Amongst the many algorithms that one can choose for optimisation problems, hillclimbing methods, linear programming (e.g. the simplex algorithm) and simulated annealing procedures are very common for finding solutions for today's optimisation problems in turbomachinery. For very good reasons, which will be obvious after a short introduction of those techniques. However, a new class of optimisation methods is becoming more and more popular for a wide variety of optimisation problems. One can find them under the terminology of *artificial intelligence techniques (AI)* or *evolutionary programming (EP)*. One subclass of those is often named *genetic algorithms (GA)*, a technique which tries to simulate nature's evolutionary process.

The short introductions of the hillclimbing algorithm and the simulated annealing algorithm are based on the textbook of Russel and Norvig about Artificial Intelligence [33].

#### 3.1.1 Hillclimbing

Hillclimbing is a very popular method for various optimisation tasks, as it is

- easy and quick to use and to program,
- very quickly converging, and therefore
- costefficient in terms of CPU-time.

Mathematically spoken it is the task of maximising (or minimising) a function  $f(\vec{x})$ , where  $\vec{x}$  represents discrete states. Figure 3.1 shows an example for a search domain of a typical hillclimbing problem. The discrete states are represented by  $z$ -values of the intersections (vertices) of the  $x - y$ -grid. A hillclimbing algorithm will follow the edges of the grid from vertex to vertex, always increasing the value of  $f$  until a local maximum is reached. A more rapid variant of hillclimbing algorithm would always detect the steepest

### 3 Optimisation

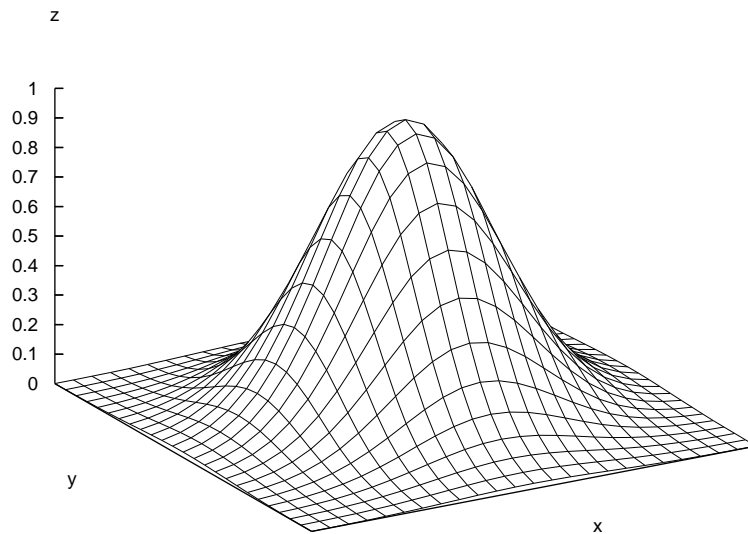


Figure 3.1: Good qualified Search Domain (Global Optimum) for Hillclimbing Algorithm

path to the next vertex (“steepest ascent hillclimbing”).

Besides all these advantages of hillclimbing algorithms, there are also some drawbacks for this class of algorithms, namely

- local maxima,
- ridges, and
- plateaus.

Figure 3.2 shows a good example for an optimisation problem, where a hillclimbing optimisation algorithm might not find the global, but a local optimum of the search domain, depending on where the algorithm starts its search. The other problems mentioned essentially result in the same difficulty, namely that the algorithm reaches a vertex, where it cannot find a vertex with a higher value of  $f$  in the local environment. To summarize, hillclimbing algorithms are very sensitive to the form of the search domain as well as to a good and careful selection of the starting point.

To overcome these problems, variants and other local search algorithms were developed such as stochastic hillclimbing, random walks, and simulated annealing, just to mention a few. Hillclimbing can also operate on a continuous search domain, in that case it is called gradient ascent (descent) method.

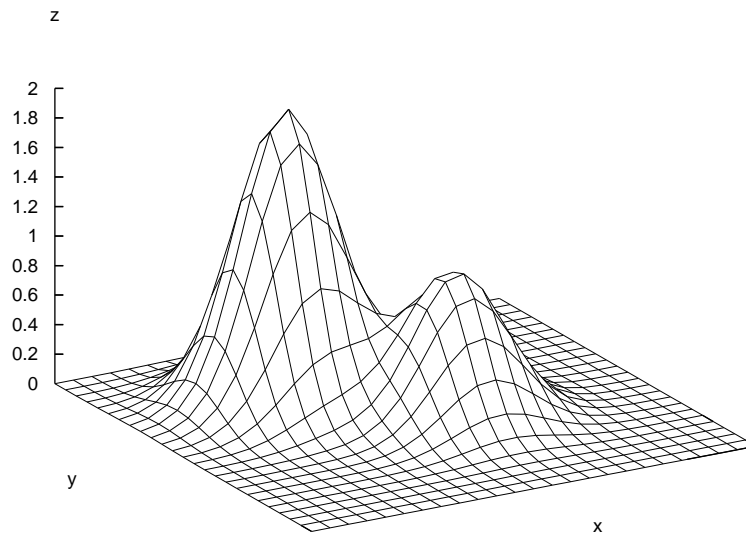


Figure 3.2: Bad qualified Search Domain (Local Optimum) for Hillclimbing Algorithm

### 3.1.2 Simplex Algorithm

Wingelhofer [47] used an adapted form of a simplex algorithm namely the downhill method of Nelder and Mead [27] to get some insight towards better design criteria for axial turbine bladings. The Nelder-Mead method, as it is also called is a commonly used nonlinear optimisation algorithm. It is a numerical method for minimising an objective function in a many dimensional space. A simplex, which is a polytope of  $N + 1$  vertices in  $N$  dimensions, is used for this method.

### 3.1.3 Simulated Annealing

Simulated annealing (SA) is a generic probabilistic meta-algorithm for locating a good approximation to the global optimum of a given function in a large search space and was presented first in 1983 by Kirkpatrick, Gelatt and Vecchi [15]. They tried to simulate the annealing process, where steel is heated and cooled down slowly and temperature-controlled afterwards, in order to let the molecules of the microstructure reorder and change into a state of lower energy level. After the annealing process some minimum of the energy level is reached, the ductility of the steel has risen. The fundamental idea is to allow moves resulting in solutions of worse quality than the current solution (uphill moves) in order to escape local minima. The probability of doing such moves is decreased during the search. Beside this advantage, there is the disadvantage, that a simulated annealing algorithm is rather time consuming, and therefore costly in terms of computing time.

<b>Problem:</b>	Given the search domain $D$ and the fitness function $f : D \rightarrow \mathbb{R}$ , find a global minimum from $f$ in $D$ , viz. $x \in D \mid f(x) \leq f(y)$ for every $y \in D$
<b>Initialisation:</b>	Choose an initial starting solution $x \in D$ Choose temperature $T$ and cooling-constant $\alpha$ Time $t := 0$
<b>Local Change:</b>	Choose $y \in D$ in the local environment of $x$
<b>Selection:</b>	If $f(y) \leq f(x)$ put $x := y$ If $f(y) > f(x)$ put $x := y$ with probability $\exp(-\frac{f(y)-f(x)}{\alpha^t T})$
<b>Breaking condition:</b>	If breaking condition is not met, start again with a local change at $t := t + 1$ , else break

Figure 3.3: Pseudocode for Simulated Annealing Optimisation Algorithm

For a better understanding, some pseudocode for a simple SA-algorithm is presented in Fig. 3.3.

### 3.1.4 Genetic Algorithm

As the genetic algorithm (GA) was the algorithm of choice in this work it shall be described and explained more in detail than the other algorithms mentioned above. A detailed presentation with the optimisation task treated in this work follows in one of the next sections. This section is based on Michalewicz [25].

A GA can be used to find solutions for parameter optimisation problems. Without any loss of generality, as will be clear later when the definitions and assumptions for the given turbomachinery problem will be presented, maximization problems only are solved by using a GA. If, as in this work, the problem given is to minimize a function  $f$ , which will be called objective function from now on, a maximization problem can be made out of it by simply maximizing the function  $g = -f$ , i.e.

$$\min f(x) = \max g(x) = \max \{-f(x)\} . \quad (3.1)$$

It is assumed, that the objective function  $f$  is positive on its domain. If this is not the case, a positive constant  $C$  can be added, that is

$$\max g(x) = \max \{g(x) + C\}. \quad (3.2)$$

### 3 Optimisation

The function  $f$  consists of  $k$  variables, namely  $f = f(x_1, x_2, \dots, x_k) : R^k \rightarrow R$ . Each variable  $x_i$  can take values from a domain  $D_i = [a_i, b_i] \subseteq R$  and  $f(x_1, x_2, \dots, x_k) > 0 \mid x_i \in D_i$ . In order to achieve a desired precision for the variables' values, for example  $n$  decimal places, the domain  $D_i[a_i, b_i]$  has to be cut into  $(b_i - a_i) \cdot 10^n$  ranges of equal size. If  $m_i$  represents the smallest integer such that  $(b_i - a_i) \cdot 10^n \leq 2^{m_i} - 1$ , then a representation having each variable  $x_i$  coded as a binary string of length  $m_i$  obviously satisfies the above mentioned precision requirement.  $x_i$  can be calculated as

$$x_i = a_i + decimal(string_{2(m_i)}) \cdot \frac{b_i - a_i}{2^{m_i} - 1} \quad (3.3)$$

where  $decimal(string_{2(m_i)})$  stands for the decimal value of a binary string of length  $m_i$ . Furtheron the following definitions will be used: An *individual* is represented by  $k$  *genes*. As  $m_i$  is the length of the binary representation of each gene,  $m = \sum_{i=1}^k m_i$  is the length of the binary representation of the individual. Herein, the first  $m_1$  bits range from  $a_1$  to  $b_1$ , the second group ranges from  $a_2$  to  $b_2$ , and so on. The last  $m_k$  bits can take values from  $D_k = [a_k, b_k]$ . The value of the function  $f = f(x_1, x_2, \dots, x_k)$  represents the *fitness value* of each individual. A *population* is made out of *pop\_size* individuals.

Having defined the prerequisites and assumptions for the GA, the actual process of optimisation can be carried out now. After having fixed the constant *pop\_size* for the given search, the initial population of individuals has to be determined. This can be done by randomly choosing *pop\_size* binary strings of length  $m$ . Each string then represents an individual of the initial population. Another, possibly more promising, method would be, to choose the candidates (individuals) of the initial population according to some specific knowledge about the distribution of some potential optima. The initial population is now evaluated (the value of the function  $f$  represents the fitness value for each individual) and a new population is selected, taking into account the probability distribution based on the fitness values. The individuals of the selected new population are altered via mutation and crossover operations. Having done that, the process starts again with evaluation of the fitness of the individual members. After some steps, when no further improvement can be observed, an optimal solution, which might be the global optimum, is found. Further techniques to enhance the speed of the algorithm or to influence the selection of the search path, as well as other possible improvements for specific problems exist and can be found in the literature, but will not be treated further here.

To select a new population of individuals, based on the probability distribution of the fitness values, as described above, some kind of roulette wheel is used. The size of the slots of the roulette wheel is defined according to the fitness of the individuals, which means, the higher the fitness of an individual, the more likely this specific individual is chosen for the next population. This can be achieved in the following way:

- Calculation of the fitness value  $eval(\mathbf{v}_i)$  for each individual  $\mathbf{v}_i$  ( $i = 1, \dots, pop\_size$ ) by evaluating  $f(\mathbf{v}_i)$
- Calculation of the fitness value for the whole population

### 3 Optimisation

$$F = \sum_{i=1}^{pop\_size} eval(\mathbf{v}_i)$$

- Calculation of the probability  $p_i$  of selection of each individual  $\mathbf{v}_i$  ( $i = 1, \dots, pop\_size$ )  

$$p_i = \frac{eval(\mathbf{v}_i)}{F}$$
- Calculation of the cumulative probability  $q_i$  for each individual  $\mathbf{v}_i$  ( $i = 1, \dots, pop\_size$ )  

$$q_i = \sum_{j=1}^i p_j$$

For each individual of the new population, the roulette wheel has to be spun once, which means spinning the roulette wheel  $pop\_size$  times to generate the whole new population, which undergoes the mutation and crossover process afterwards. The selection itself is processed as follows:

- Generation of a random (float) number  $r$  in the range  $[0..1]$
- Selection of the first individual  $\mathbf{v}_1$  as a member of the new population if  $r < q_1$ ; else, selection of the  $i$ -th individual  $\mathbf{v}_i$  ( $2 \leq i \leq pop\_size$ ) such that  $q_{i-1} < r < q_i$

Having selected  $pop\_size$  individuals of the old population as members of the new (before crossover and mutation) population, these individuals then undergo the process of recombination (crossover) and mutation. In order to determine the candidates for undergoing these alterations, two new variables, namely  $p_c$  and  $p_m$  are introduced. They determine the probability of crossover and mutation respectively.  $p_c$  and  $p_m$  may vary from step to step of the algorithm or be left unchanged.

The number of individuals, which are expected to undergo the process of crossover is defined by the product  $p_c \cdot pop\_size$ . To select the candidates for crossover, the following steps have to be carried out for each individual ( $pop\_size$  times):

- Generation of a random (float) number  $r$  in the range  $[0..1]$
- Selection for crossover of the given individual if  $r < p_c$

In case the number of selected individuals for crossover is even, they can be paired easily, in case the number is odd, either an extra individual is added for mating, or, one selected individual is removed from the selection - this choice is done at random as well. For each pair of selected individuals for crossover a random integer number  $pos$  in the range of  $[1..m - 1]$  has to be generated, which indicates the position of the crossing point. Then, the two individuals

$$\begin{pmatrix} b_1 b_2 \dots b_{pos} b_{pos+1} \dots b_m \\ c_1 c_2 \dots c_{pos} c_{pos+1} \dots c_m \end{pmatrix} \quad \text{and}$$

are replaced by their offspring:

$$\begin{pmatrix} b_1 b_2 \dots b_{pos} c_{pos+1} \dots b_m \\ c_1 c_2 \dots c_{pos} b_{pos+1} \dots c_m \end{pmatrix}.$$

The second alteration, which is performed on the population, is called mutation. It is

performed on a bit-by-bit basis for the whole population, so the below mentioned steps have to be performed  $m \cdot pop\_size$ -times. The expected number of bits which undergo the process of mutation is calculated by  $p_m \cdot m \cdot pop\_size$ . Each bit has the same chance to be mutated, i.e. change its value from 0 to 1 or vice versa. The selection of the bits, which undergo mutation is similar to the selection for crossover:

- Generation of a random (float) number  $r$  in the range  $[0..1]$
- Mutation of the bit if  $r < p_m$

After the mutation, the new population is now ready restart the algorithm by evaluating the fitness values of the new population. Then, one step of the evolution is finished, the rest is just cyclic repetition of the steps explained above.

### 3.2 Definition of the Genetic Algorithm for the given Problem

The initial configuration is a cylindric HP-steam turbine blade, as described in Chap. 2.4. In this work it was decided to alter two parameters of the initial, cylindric, configuration, while keeping the rest unaltered. The, originally straight, span of the cylindric blade is replaced by two parabolic arcs at the sidewalls and a straight spanwise piece in between them. This is sketched in Fig 3.4.

$\alpha$  denotes the angle between the spanwise direction, and the tangent of the parabolic arc, where the arc intersects with the sidewall.  $h$  denotes half of the straight piece in spanwise direction between the arcs. For practical reasons, namely manufacturing and installing of the final configuration(s), it was decided to limit  $\alpha$  in the range of  $[-45^\circ \leq \alpha \leq 45^\circ]$ . Positive values for  $\alpha$  denote a convex pressure side of the blade, negative values denote a convex suction side (Fig 3.4 shows a positive value of  $\alpha$ ). For reasons of computing time, only half of the blade was modelled for being calculated in the subsequent CFD calculations, therefore  $h$  was limited in the range of  $0 \text{ mm} \leq h \leq 75 \text{ mm}$ . The precision was set to be  $1^\circ$  for  $\alpha$  and 1 mm minimum increment for  $h$ . Following the description of the genetic algorithm from Chap. 3.1.4, two domains  $D_1$  and  $D_2$  for the parameters  $x_1$  ( $h$ ) and  $x_2$  ( $\alpha$ ) have to be defined. The requirement

$$(b_i - a_i) \cdot 10^n \leq 2^{m_i} - 1 , \quad (3.4)$$

has to be fulfilled, therefore  $m_1$ , which stands for the length of the binary representation of  $h$ , was set to be 7, because  $2^6 \leq 75 \leq 2^7$ . The same considerations for  $m_2$ , which is the length of the binary representation of  $\alpha$ , resulted in  $m_2 = 7$  as well, as  $2^6 \leq 90 \leq 2^7$ . So the binary representation of one blade configuration is  $m = m_1 + m_2 = 7 + 7 = 14$  bits long.

To calculate the fitness of the individuals and of the whole population as well, an objective function had to be chosen next. Wingelhofer and Haselbacher [48], for example, used flow

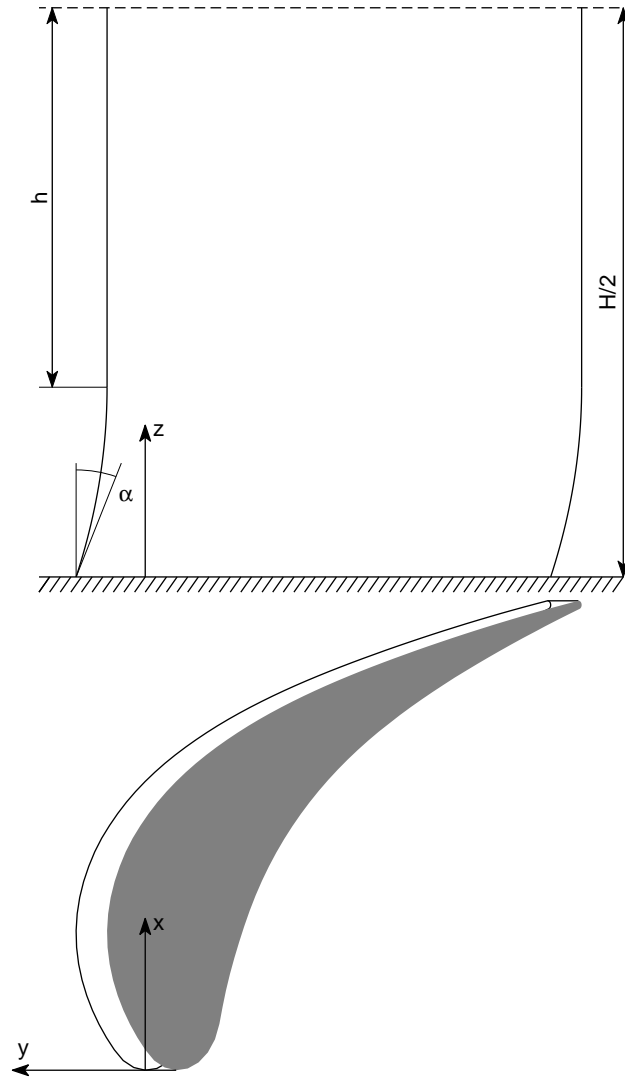


Figure 3.4: The two altered Parameters of the 3D Configuration

homogeneity of the exit flow from the nozzle blades as objective function for optimizing the stator row of a turbine stage. An optimisation algorithm proposed new compound lean designs for the stator blades, following that, the stage efficiency for the whole stage was evaluated.

According to Denton [7] the only rational measure of loss in an adiabatic machine is entropy creation, as any irreversible flow process creates entropy and therefore reduces isentropic efficiency. Entropy cannot be measured or seen directly, but has to be calculated with the rules of thermodynamics with any other two thermodynamic properties, that can be measured, such as temperature and pressure. The relations for a perfect gas read as

### 3 Optimisation

$$s - s_{ref} = c_p \ln \frac{T}{T_{ref}} - R \ln \frac{p}{p_{ref}} \quad (3.5)$$

and

$$s - s_{ref} = c_v \ln \frac{T}{T_{ref}} - R \ln \frac{\rho}{\rho_{ref}} . \quad (3.6)$$

All the thermodynamic properties used in these equations are either static or stagnation values, as, by definition, the change from static to stagnation conditions is isentropic. Denton further argues, that for adiabatic flow through a stationary blade row the change in entropy is only dependent on the stagnation pressures, viz.

$$\Delta s = -R \ln \frac{p_{t1}}{p_{t0}} . \quad (3.7)$$

For small changes in stagnation pressure between inlet and outlet of a blade cascade, which is the case here, Eq. 3.7 can be rewritten as

$$\Delta s = -R \frac{\Delta p_t}{p_t} . \quad (3.8)$$

Hence, the loss of stagnation pressure can be used as equal to the increase of entropy of the blade row. Therefore, the total pressure loss coefficient  $\omega$ , defined in Eq. 3.9 was used as the objective function of choice in this work. The index "1" here stands for the outlet, which was set to same axial position as in the experiment (see Chap. 2.4) that was used for calibration of the CFD calculation. "0" as an index indicates the inlet conditions.

$$\omega = \frac{\bar{p}_{t0} - \bar{p}_{t1}}{\bar{p}_{t1} - \bar{p}_1} = \frac{\Delta \bar{p}_t}{\frac{1}{2} \rho \bar{w}_1^2} = \frac{\Delta \bar{p}_t}{\bar{p}_{1,dyn}} . \quad (3.9)$$

As described in Chap. 3.1.4, a very important part of a genetic algorithm is the ability to generate random numbers in the range [0..1]. A computer is a strongly deterministic machine, therefore it is indeed not easy to generate such random numbers, which pass statistical test in order to be distributed really randomly. Here, the method *ran1* from [31] was chosen, as the authors claim, that, to their knowledge, no statistical test so far is known, that would reveal, that the numbers generated by *ran1* were not randomly distributed. *ran1* was used for the generation of all random numbers needed for running the genetic algorithm.

After having set the population size *pop\_size* to consist of ten individuals, it was imperative to define an initial population. This was done by randomly generating *pop\_size* · *m* bits. The resultant initial population is displayed in Tab. 3.1.

Binary representation	$\alpha, ^\circ$	$h, \text{ mm}$
10000000000000	0	0
10001110100010	5	20
10010111111011	8	72
10100010001010	12	5
11100111000000	36	37
01011000000000	-14	0
00101100001010	-30	5
00011111011111	-35	56
11001001001110	25	46
11010101111111	30	75

Table 3.1: Initial Population of the Genetic Algorithm

Finally, the probability for mating was set to  $p_c = 0.25$ , that is, on average, 25% of the population were expected to undergo the process of crossover in every generation. The probability of mutation was set to  $p_m = 0.01$ . This means, that, on average, 1% of the genes in every generation were expected to undergo mutation. These values were left unchanged from generation to generation.

The Genetic Algorithm for the problem was then well-defined, as

- an objective function,
- the size of the population,
- the binary representations of the parameters plus their precisions,
- the probabilities for crossover and mutation, and
- an initial population

had been fixed. Next, the fitness values of the individuals had to be determined. This was done by evaluating each configuration by means of CFD. In order to be able to do that, the preparations that were necessary to start with the evaluations are presented here.

### 3.3 Grid Generation and Boundary Condition Definition

The construction of the computational domain and the meshing was done by means of ANSYS Gambit<sup>®</sup>. A 2D sketch of the computational domain at the sidewall and the blade profile is shown in Fig. 3.5.

The fluid flows from the left to the right, so the left boundary, where the fluid enters was defined as a so-called "Velocity Inlet". This means, that on this boundary the boundary condition informations consist of velocity informations mainly. The right boundary,

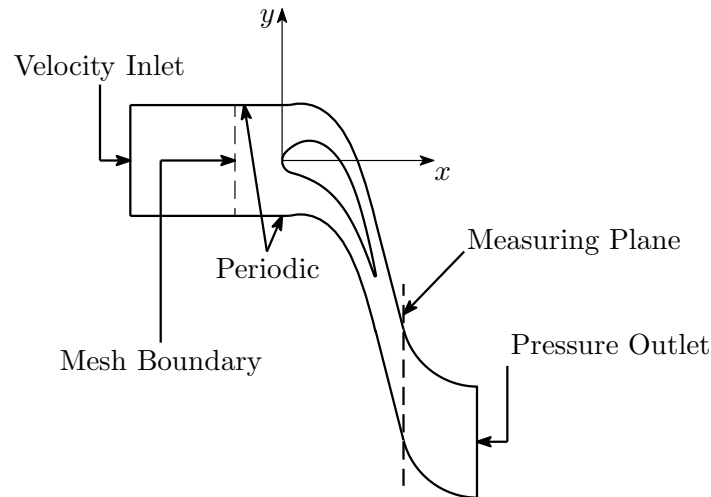


Figure 3.5: 2D Sketch of Computational Domain

where the fluid leaves the domain was defined as "Pressure Outlet", so the boundary conditions were defined via (static) pressure. The upper and lower boundaries of the domain were defined as "Periodic", that is, an unlimited cascade of blades plus their respective computational domains were defined in this way. To save computing time, only half of the blade was calculated, so, at  $z = \frac{H}{2}$ , a symmetric boundary was introduced. Similar to the calibration experiment at  $z = 0$  the boundary was defined as "Wall". In addition, the so-called "Measuring Plane", that is the plane parallel to the  $y - z$ -plane, where the heads of the pressure probes were traversed in a translational way in  $y$ -direction during the experiment is outlined in Fig. 3.5. The mesh boundary is the boundary between the structured and unstructured grid and will be explained in further detail later.

### 3.3.1 Meshing of the Computational Domain

The construction of the computational mesh was separated in two main parts, that is, the generation of the 2D mesh in the  $x$ - $y$ -plane, which was left unchanged for all configurations, and the mesh in the third dimension, which was constructed for each configuration by so-called "Coopering" of the 2D mesh along an edge of the computational domain. The 2D mesh consists of a structured mesh from the Velocity Inlet to the Mesh Boundary with quadrilateral cells, a so-called "Boundary Layer" around the blade profile and an unstructured mesh in the rest of the domain. The structured mesh in the inflow region was chosen in order to get well-controlled inflow conditions upstream of the blade. The boundary layer around the blade profile was chosen for two reasons: First, it is imperative to have a well-defined mesh in Near-Wall-Regions, speaking in terms of mesh resolution, as the flow near walls, and the blade is treated like a solid wall, has to be resolved correctly with the chosen turbulence model. Second, leaving the algorithms, that Gambit<sup>©</sup> uses for its unstructured meshes, define a mesh for the whole computational domain either results in meshes, that are not satisfactory for calculating the flow for this problem, or,

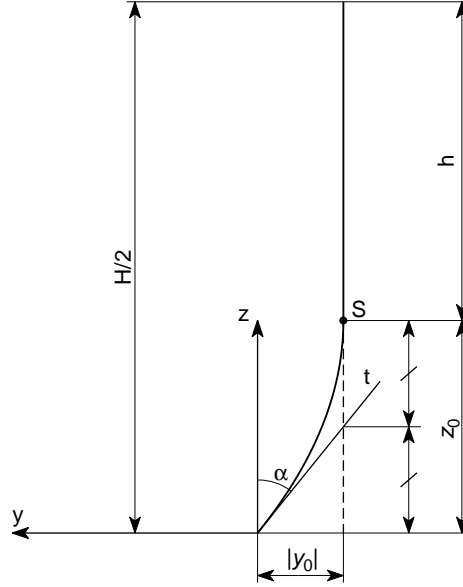


Figure 3.6: Calculation of Vertex Coordinates of Parabola

it results in a mesh, which would be much too fine for the turbulence model chosen and therefore, finally, use much too much CPU-time for the whole optimisation problem.

To construct the 3D domain and mesh it, a parabola was erected at the intersection of the lower Periodic Boundary and the Velocity Inlet at  $\frac{x}{c} = -1$ . The coordinates of the vertex of the parabola were calculated according to Fig. 3.6 and

$$y_0 = \tan(\alpha) \cdot \frac{z_0}{2} \quad (3.10)$$

taken from [36].

This edge was then meshed and moved along the boundaries (periodic and blade), creating the mesh of the periodic boundaries and the 3D mesh of the blade surface at the same time. Finally, the 2D mesh of the  $x$ - $y$ -plane was so-called "coopered" along the now existing meshes from  $z = 0$  to  $z = \frac{H}{2}$ . Further control possibilities of the meshing, which were used during the process (e.g. number of mesh points along certain edges of the model) are not described in further detail here. In order to ensure a satisfying quality of all meshes possible during the optimisation process, the most extreme configurations ( $\alpha = \pm 45^\circ$ ,  $h = 0/75$  mm) were meshed and the quality of the meshes was checked manually before starting the optimisation. The number of cells of the whole mesh stayed the same for all configurations and was equal to 239250, the number of mesh points, or nodes, was equivalent to 261092. Hildebrandt and Fottner [13] concluded, that for a typical CFD calculation of a turbine blade cascade, about 1 million mesh points halfspan is the minimum for a solution to be independent of the type of mesh and of the mesh resolution. Test calculations prior to the start of the optimisation process did not show better results with finer meshes, so the above mentioned number of roughly  $2.5 \cdot 10^5$  cells seemed sufficient for the given problem, and, as a consequence, was used for the

optimisation. It is important to mention the fact, that, due to the specific modelling and meshing method chosen, the quality of the mesh varied slightly from configuration to configuration.

### 3.3.2 Modelling Turbulence

When speaking in terms of turbulence, one has to envision, that all sorts of flows occur in typical turbomachinery flow, viz. laminar flow, transitional flow and turbulent flow. Therefore, careful attention has to be layed on the modelling of turbulence when calculating flow through a turbomachine, but the same is valid when calculating flow through a linear blade cascade. The many ways of modelling turbulence, that are provided today can roughly be divided into algebraic models, one- and two-equation models and other models.

The complexity and difficulty of the models also rises in this order, as only algebraic equations have to be solved for the first type, up to two additional partial differential equations have to be solved <sup>1</sup> for the second type, and more than two additional differential equations have to be solved for the others. This complexity also increases the calculation time for the CFD solver, which is an important parameter for an optimisation task, as it was performed in this work. Algebraic models are, from their nature, so-called "incomplete" models, which means, that additional information about the scales of turbulence <sup>2</sup>, that occur in the flow under examination, have to be supplied by the investigator in order to get reliable results. Although Wilcox [45] points out, that those models are in general of little use when it is tried to apply them beyond the established data, for which they were fine tuned and calibrated, Lampart et al. ([18], [19] and [20]) did extensively use a modified algebraic turbulence model of Baldwin and Lomax for their numerical studies. As several works of Lampart et al. were done with this model, it is assumed, that they indeed did calibrate this model for their specific use. The models, that were termed "others" here, are, generally speaking, more complex than the one- and two-equations models, as substantially more partial differential equations are used to model the scales, the nature and the processes, such as energy transport or dissipation between eddies, of turbulence. Direct numerical simulation (DNS), large eddy simulation (LES) and detached eddy simulation (DES) shall be mentioned here as prominent representatives of this group. As those models are also very "costly" in terms of computing time, they were not considered as an option in this work.

The models of choice therefore had to be found in the group of one- and two-equation models. Hildebrandt and Fottner [13] used three types of turbulence models during their studies on grid refinement and turbulence modelling, namely a High-Reynolds-Number  $k/\varepsilon$  model, a Low-Reynolds-Number  $k/\varepsilon$  model and a  $k/\omega$  model. Compared to the influence of the grid resolution, they identified the influence of the turbulence model as rather insignificant. For obvious reasons, the Low-Reynolds-Number  $k/\varepsilon$  model

---

<sup>1</sup>simultaneously

<sup>2</sup>e.g. mixing length

### 3 Optimisation

performed best in near-wall-regions, but it shall also be annotated, that this kind of model requires a very fine grid in those regions ( $\text{Wall-}y^+ \leq 2$ ), which, in turn, results in a grid with a very high number of grid points for the whole computational domain. But, as more grid points always involve an increase in computational effort, the Low-Reynolds-Number  $k/\varepsilon$  model was not considered as a good option here. Wilcox [45] claims the  $k/\omega$  model to show a very good behaviour when dealing with wall-bounded and free shear flow in one problem, in addition, he reports very good results for the model when the flow is exposed to adverse pressure gradients. An often used variant of the  $k/\varepsilon$  model is the so-called Renormalization Group (RNG)  $k/\varepsilon$  model. Orszag et al. [28] show the applicability of this models in various example, where it turns out, that this modified  $k/\varepsilon$  model delivers very good results for flows with unsteady effects such as separation bubbles. Being well aware, that every model has its advantages and disadvantages, it was chosen to use the Standard  $k/\varepsilon$  model in this work.

The basic concept and assumptions of the Standard  $k/\varepsilon$  model shall be presented very briefly for better understanding in the following paragraphs:

When speaking of turbulence, it means that the various flow properties fluctuate randomly. In order to classify these fluctuations, a statistical approach was chosen, namely to split up the flow property into an average part and a fluctuating part at any instantaneous moment. To determine the mean quantity, several averaging procedures can be chosen (time-averaging, spatial-averaging and ensemble-averaging), here, only time-averaging will further be considered, which, for a flow variable  $f(\mathbf{x}, t)$  of stationary flow, can be written as:

$$F_T(\mathbf{x}) = \lim_{T \rightarrow \infty} \frac{1}{T} \int_t^{t+T} f(\mathbf{x}, t) dt . \quad (3.11)$$

The instantaneous velocity  $u_i(\mathbf{x}, t)$  can then be described for a stationary turbulent flow as

$$u_i(\mathbf{x}, t) = U_i(\mathbf{x}) + u'_i(\mathbf{x}, t) , \quad (3.12)$$

where  $U_i(\mathbf{x})$  represents the mean part and  $u'_i(\mathbf{x}, t)$  the fluctuating part (compare Fig. 3.7).

The following rules, that the time-average <sup>3</sup> of a mean property is again the same time-averaged value, i.e.

$$\overline{U_i(\mathbf{x})} = \lim_{T \rightarrow \infty} \frac{1}{T} \int_t^{t+T} U_i(\mathbf{x}) dt = U_i(\mathbf{x}) , \quad (3.13)$$

and that the time-average of the fluctuating part is zero, i.e.

---

<sup>3</sup>overbar is short for time-average

### 3 Optimisation

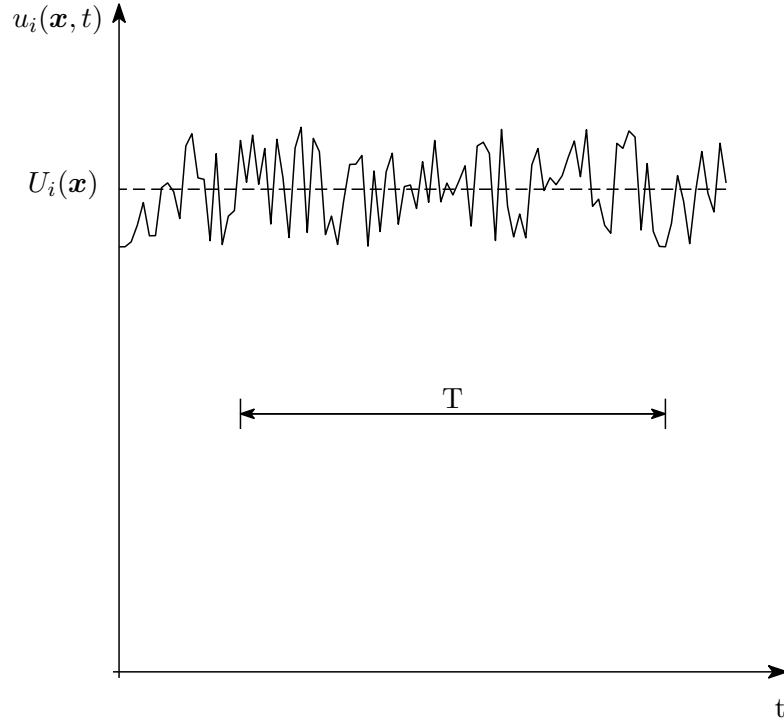


Figure 3.7: Time-Averaging for Stationary Turbulence

$$\overline{u'_i} = \lim_{T \rightarrow \infty} \frac{1}{T} \int_t^{t+T} [u_i(\mathbf{x}, t) - U_i(\mathbf{x})] dt = U_i(\mathbf{x}) - \overline{U_i(\mathbf{x})} = 0, \quad (3.14)$$

and that the average of the product of two quantities  $\phi$  and  $\psi$  is

$$\overline{\phi\psi} = \overline{(\Phi + \phi')(\Psi + \psi')} = \overline{\Phi\Psi + \Phi\psi' + \Psi\phi' + \phi'\psi'} = \Phi\Psi + \overline{\phi'\psi'}, \quad (3.15)$$

are used in the following deduction, where, for the sake of brevity, tensor notation will be used:

For incompressible, constant-property flow, the equations for conservation of mass and momentum are

$$\frac{\partial u_i}{\partial x_i} = 0 \quad (3.16)$$

$$\rho \frac{\partial u_i}{\partial t} + \rho u_j \frac{\partial u_i}{\partial x_j} = -\frac{\partial p}{\partial x_j} + \frac{\partial t_{ji}}{\partial x_j} \quad (3.17)$$

$t_{ij}$  is the viscous stress tensor defined by

### 3 Optimisation

$$t_{ij} = 2\mu s_{ij} \quad (3.18)$$

with the molecular viscosity  $\mu$  and the strain-rate tensor

$$s_{ij} = \frac{1}{2} \left( \frac{\partial u_i}{\partial x_j} + \frac{\partial u_j}{\partial x_i} \right). \quad (3.19)$$

Combining Eqs. 3.16 through 3.19 yields the Navier Stokes equation in conservation form, namely

$$\rho \frac{\partial u_i}{\partial t} + \rho \frac{\partial}{\partial x_j} (u_j u_i) = -\frac{\partial p}{\partial x_i} + \frac{\partial}{\partial x_j} (2\mu s_{ji}) \quad (3.20)$$

Time-averaging Eq. 3.16 and Eq. 3.20 results in the Reynolds-averaged equations of motion in conservation form, viz.

$$\frac{\partial U_i}{\partial x_i} = 0 \quad (3.21)$$

$$\rho \frac{\partial U_i}{\partial t} + \rho \frac{\partial}{\partial x_j} \left( U_j U_i + \overline{u'_j u'_i} \right) = -\frac{\partial P}{\partial x_i} + \frac{\partial}{\partial x_j} (2\mu S_{ji}) \quad (3.22)$$

The new correlation  $\overline{u'_i u'_j}$  is a time-averaged rate of momentum transfer due to turbulence. Rewriting Eq. 3.22 leads to the so-called Reynolds-averaged Navier Stokes equation (RANS):

$$\rho \frac{\partial U_i}{\partial t} + \rho U_j \frac{\partial U_i}{\partial x_j} = -\frac{\partial P}{\partial x_i} + \frac{\partial}{\partial x_j} \left( 2\mu S_{ji} - \overline{\rho u'_j u'_i} \right) \quad (3.23)$$

$-\overline{\rho u'_i u'_j}$  is called the Reynolds stress tensor, denoted by  $\rho \tau_{ij}$ , therefore  $\tau_{ij}$  is the specific Reynolds stress tensor<sup>4</sup>. By time-averaging the equations for conservation of mass and conservation of momentum, six new unknown quantities, the Reynolds stress components, were produced. Unfortunately, no additional equations were developed, so for ten unknown flow properties ( $p, u_i, \overline{u'_i u'_j}$ ) only four equations are available, so the system of equations cannot be closed. Herein lies the fundamental problem of turbulence.

Introducing the Boussinesq approximation, which models, similar to the molecular viscosity  $\mu$  in Stoke's Friction Law for laminar flow, a turbulent, or eddy, viscosity  $\mu_t$ , the Reynolds stress can be written as

---

<sup>4</sup> $\tau_{ij}$  is symmetric, hence  $\tau_{ij} = \tau_{ji}$

### 3 Optimisation

$$-\overline{\rho u'_i u'_j} = \mu_t \left( \frac{\partial U_i}{\partial x_j} + \frac{\partial U_j}{\partial x_i} \right) - \frac{2}{3} \rho k \delta_{ij} , \quad (3.24)$$

where the second term on the right-hand side of the equation represents the turbulent pressure (with  $\delta_{ij} = 1$  for  $i = j$  and  $\delta_{ij} = 0$  for  $i \neq j$ ), which is assumed to be proportional to the turbulent kinetic energy per unit mass, viz.

$$k = \frac{1}{2} \overline{u'_i u'_i} = \frac{1}{2} \left( \overline{u'^2} + \overline{v'^2} + \overline{w'^2} \right) \quad (3.25)$$

The turbulent intensity  $Tu$  is defined with the arithmetic average of the Reynolds-normal-stresses divided by the local absolute value of velocity as

$$Tu = \sqrt{\frac{\overline{u'^2} + \overline{v'^2} + \overline{w'^2}}{3(u^2 + v^2 + w^2)}} . \quad (3.26)$$

In the inlet region of the cascade under investigation, nearly isotropic turbulent fluctuations of the velocity are assumed, resulting in

$$k = \frac{\overline{u'^2} + \overline{v'^2} + \overline{w'^2}}{2} = \frac{3}{2} \overline{u'^2} . \quad (3.27)$$

The turbulent intensity at the cascade inlet can therefore be described as

$$Tu = \sqrt{\frac{2}{3} \frac{k}{U_e^2}} , \quad (3.28)$$

with  $U_e$  being the freestream mean-flow velocity at the inlet region.

Having explained all the fundamentals of the  $k/\varepsilon$  model above, the equation for the kinematic eddy viscosity  $\nu_t$

$$\nu_t = C_\mu \frac{k^2}{\varepsilon} , \quad (3.29)$$

the transport equation for the turbulent kinetic energy  $k$

$$\frac{\partial k}{\partial t} + U_j \frac{\partial k}{\partial x_j} = \tau_{ij} \frac{\partial U_i}{\partial x_j} - \varepsilon + \frac{\partial}{\partial x_j} \left[ \left( \nu + \frac{\nu_t}{\sigma_k} \right) \frac{\partial k}{\partial x_j} \right] , \quad (3.30)$$

the transport equation for the turbulent dissipation rate  $\varepsilon$

### 3 Optimisation

$$\frac{\partial \varepsilon}{\partial t} + U_j \frac{\partial \varepsilon}{\partial x_j} = C_{\varepsilon 1} \frac{\varepsilon}{k} \tau_{ij} \frac{\partial U_i}{\partial x_j} - C_{\varepsilon 2} \frac{\varepsilon^2}{k} + \frac{\partial}{\partial x_j} \left[ \left( \nu + \frac{\nu_t}{\sigma_\varepsilon} \right) \frac{\partial \varepsilon}{\partial x_j} \right], \quad (3.31)$$

and the closure coefficients

$$C_{\varepsilon 1} = 1.44, \quad C_{\varepsilon 2} = 1.92, \quad C_\mu = 0.09, \quad \sigma_k = 1.0, \quad \sigma_\varepsilon = 1.3 \quad (3.32)$$

are given without further deduction. In Eq. 3.30 the first term on the left-hand side represents the unsteady term, the second term on the left-hand side stands for the convection. Together they give the rate of change of  $k$  of a fluid particle of the flow. The first term on the right-hand of Eq. 3.30 is the production term, the rate, at which kinetic energy is transferred from the mean flow to the turbulence.  $\varepsilon$ , the turbulent dissipation rate, which is the rate, at which turbulent kinetic energy is transformed into internal thermal energy, is defined to be

$$\varepsilon = \nu \overline{\frac{\partial u'_i}{\partial x_k} \frac{\partial u'_i}{\partial x_k}}. \quad (3.33)$$

The term  $\nu \frac{\partial k}{\partial x_j}$  represents the molecular diffusion, and, finally, the term  $\frac{\nu_t}{\sigma_k} \frac{\partial k}{\partial x_j}$  describes the turbulent transport and pressure diffusion.

The application of the Standard  $k/\varepsilon$  turbulence model demands certain prerequisites, namely:

- It can only be applied for High-Reynolds-number flow.
- The near-wall regions in wall-bounded flows have to be calculated with wall-functions, because the model cannot predict correct results for these regions.
- The nondimensional, sublayer scaled, wall-distance  $y^+$  has to be  $\approx 30 \leq y^+ \leq \approx 100$ .

The Standard  $k/\varepsilon$  model, being a High-Reynolds-number model, cannot predict accurate and correct results in near-wall-regions for wall-bounded flows, as the Reynolds numbers, calculated with a significant cell dimension, in those regions are low. Viscous stresses dominate over turbulent Reynolds stresses in these regions, therefore wall-functions were developed to overcome these disadvantages. The idea was to supply empirical functions  $u^+ = f(y^+)$ , which define the flow velocity being dependent of the wall-distance. As the Standard  $k/\varepsilon$  model cannot be integrated satisfactory through the viscous sublayer, a linear relation between the nondimensional velocity  $u^+$  and the nondimensional wall-distance  $y^+$  was modelled for this viscous sublayer, viz.

$$u^+ = y^+. \quad (3.34)$$

### 3 Optimisation

The nondimensional wall-distance  $y^+$  and the nondimensional velocity  $u^+$  are being defined as

$$y^+ = \frac{u_\tau y}{\nu} \quad \text{and} \quad u^+ = \frac{U}{u_\tau} \quad (3.35)$$

with the friction velocity  $u_\tau$  being defined as

$$u_\tau = \sqrt{\frac{\tau_W}{\rho}} \quad . \quad (3.36)$$

Schlichting and Gersten [34] and Wilcox [45] show, that a turbulent boundary layer consists of a thin wall layer, or viscous sublayer, a fully turbulent outer layer, the log layer, a so-called overlap region in between them, and a defect layer at the edge of the boundary layer. In the viscous sublayer both, turbulent and molecular momentum transfer act. In the fully turbulent outer layer molecular, or viscous, stress can be neglected compared to the Reynolds stress. This region lies approximately in between  $y^+ = 30$  and  $y = 0.1 \cdot \delta$ , with the value of  $y^+$  at the upper boundary depending upon the Reynolds number of the flow. It should be mentioned, that the layer thickness of the log layer is several orders of magnitude larger than the thickness of the viscous sublayer. In the defect layer, reaching from the upper boundary of the log layer until the edge of the boundary layer, the velocity of the flow asymptotically approaches the value of the freestream velocity. The logarithmic law of wall is not valid in this region any more.

A sketch of a typical turbulent boundary layer with the viscous sublayer, the overlap region and the log layer is depicted in Fig. 3.8.

In the region of the log layer, the logarithmic Law of Wall

$$u^+ = \frac{1}{\kappa} \ln y^+ + C \quad (3.37)$$

can be applied with  $\kappa$  being Kármán's constant.  $\kappa \approx 0.41$  for smooth and rough surfaces and  $C \approx 5.0$  for smooth surfaces were determined by correlations with experiments [17].

As was mentioned above and can be seen from Fig. 3.8, the logarithmic law of wall can only model the dimensionless velocity  $u^+$  correctly, if the nondimensional wall-distance  $y^+ \geq 30$ , in addition,  $y^+$  should not exceed 100 (1000) very much <sup>5</sup> for typical turbomachinery applications, as the region of the defect layer is beginning there, and the logarithmic law of wall is not valid there any more. Equation 3.35 shows, that this results in the condition, that the cells next to a wall must not be too small, so that they do not fully lie inside the viscous sublayer. This condition was fully met by the mesh used for the optimisation.

---

<sup>5</sup>Values for the upper limit of  $y^+$  ranging from 100 to 1000 can be found in the literature for variants of the Standard  $k/\varepsilon$  model.

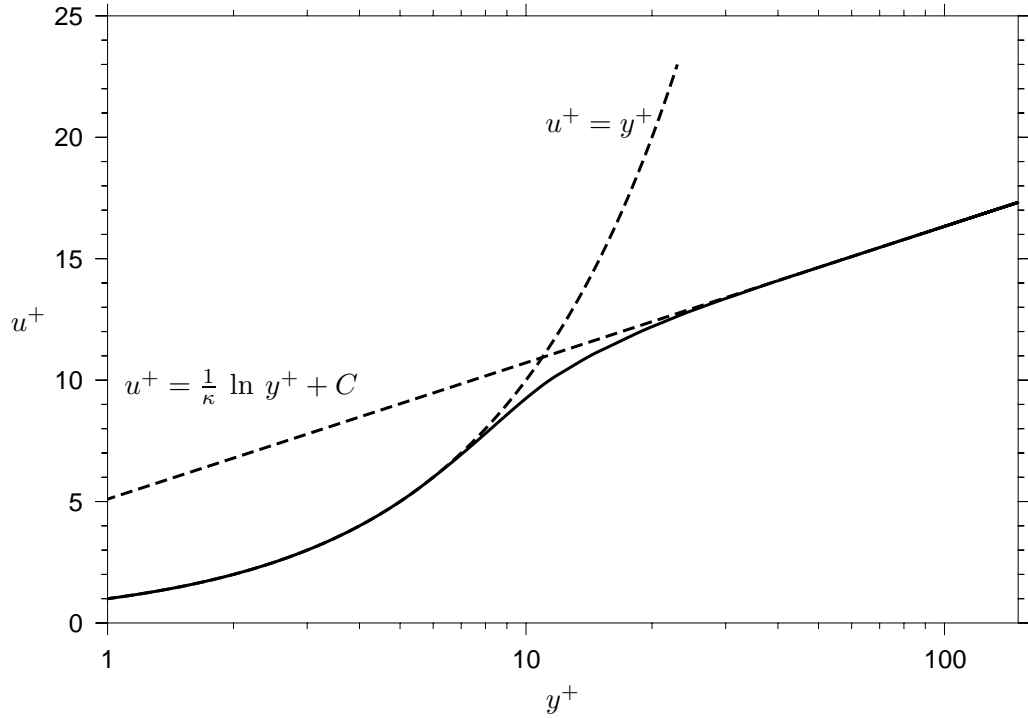


Figure 3.8: Turbulent Boundary Layer: Viscous Sublayer, Overlap Region and Log Layer

### 3.3.3 Boundary Conditions, nondimensional Variables, numerical Schemes

It is a common practice in turbomachinery design to calculate the relevant variables and equations in a nondimensional form. One reason for using this practice is that the results of different investigations with different boundary conditions, blades, etc. can be more easily compared, when the results are presented in a scaled, nondimensional form. Another important reason is, that for a CFD calculation, the values calculated for the different flow properties are of the same order of magnitude (around O1), which, in turn, gives higher levels of accuracy, as roundoff errors are somehow reduced. This practice was followed here, the variables were defined and verified in the relevant equations. For practical reasons, the derivation is presented for two dimensional equations, that is for  $x$  and  $y$ , only. The definitions

$$\begin{aligned} x^* &= \frac{x}{c} \\ y^* &= \frac{y}{c} \end{aligned} \quad (3.38)$$

$$\begin{aligned} u^* &= \frac{u}{w_0} \\ v^* &= \frac{v}{w_0} \end{aligned} \quad (3.39)$$

represent the nondimensional lengths and velocities. In the continuity equation for steady state flow ( $\frac{\partial}{\partial t} = 0$ ), which in its original form reads as

### 3 Optimisation

$$\frac{\partial u}{\partial x} + \frac{\partial v}{\partial y} = 0 \quad (3.40)$$

$u$  and  $v$  are replaced by their nondimensional representations. Therefore

$$\frac{w_0}{c} \frac{\partial u^*}{\partial x^*} + \frac{w_0}{c} \frac{\partial v^*}{\partial y^*} = 0$$

is leading to

$$\frac{\partial u^*}{\partial x^*} + \frac{\partial v^*}{\partial y^*} = 0 . \quad (3.41)$$

With the nondimensional pressure and the Reynolds number (calculated with the chord length of the blade and the inlet flow velocity)

$$p^* = \frac{p}{\rho \cdot w_0^2} \quad (3.42)$$

$$Re_0 = \frac{w_0 \cdot c}{\nu} \quad (3.43)$$

the Navier Stokes equations for steady state flow with neglected gravity influence

$$u \frac{\partial u}{\partial x} + v \frac{\partial u}{\partial y} = -\frac{1}{\rho} \frac{\partial p}{\partial x} + \nu \left( \frac{\partial^2 u}{\partial x^2} + \frac{\partial^2 u}{\partial y^2} \right) \quad (3.44a)$$

$$u \frac{\partial v}{\partial x} + v \frac{\partial v}{\partial y} = -\frac{1}{\rho} \frac{\partial p}{\partial y} + \nu \left( \frac{\partial^2 v}{\partial x^2} + \frac{\partial^2 v}{\partial y^2} \right) \quad (3.44b)$$

lead to the nondimensional Navier Stokes equations, given as

$$\begin{aligned} u^* \frac{\partial u^*}{\partial x^*} + v^* \frac{\partial u^*}{\partial y^*} &= -\frac{1}{\rho} \frac{1}{w_0^2} \frac{\partial p}{\partial x^*} + \frac{\nu}{c w_0} \left( \frac{\partial^2 u^*}{\partial x^{*2}} + \frac{\partial^2 u^*}{\partial y^{*2}} \right) = \\ &= -\frac{\partial p^*}{\partial x^*} + \frac{1}{Re_0} \left( \frac{\partial^2 u^*}{\partial x^{*2}} + \frac{\partial^2 u^*}{\partial y^{*2}} \right) , \end{aligned} \quad (3.45a)$$

and

$$\begin{aligned} u^* \frac{\partial v^*}{\partial x^*} + v^* \frac{\partial v^*}{\partial y^*} &= -\frac{1}{\rho} \frac{1}{w_0^2} \frac{\partial p}{\partial y^*} + \frac{\nu}{c w_0} \left( \frac{\partial^2 v^*}{\partial x^{*2}} + \frac{\partial^2 v^*}{\partial y^{*2}} \right) = \\ &= -\frac{\partial p^*}{\partial y^*} + \frac{1}{Re_0} \left( \frac{\partial^2 v^*}{\partial x^{*2}} + \frac{\partial^2 v^*}{\partial y^{*2}} \right) . \end{aligned} \quad (3.45b)$$

### 3 Optimisation

The equations for the  $k/\varepsilon$  turbulence model had to be made nondimensional as well. According to Launder and Spalding in their original paper of the  $k/\varepsilon$  turbulence model [23], the High-Reynolds number formulation of the model was used, neglecting the influence of molecular diffusion, as it is several orders of magnitude smaller than the turbulent transport and pressure diffusion. This means, that the term  $\frac{\partial}{\partial x_j} \left[ \left( \nu + \frac{\nu_t}{\sigma_k} \right) \frac{\partial k}{\partial x_j} \right]$  was replaced with  $\frac{\partial}{\partial x_j} \left[ \frac{\nu_t}{\sigma_k} \left( \frac{\partial k}{\partial x_j} \right) \right]$  in the transport equation for the turbulent kinetic energy,  $k$ , yielding

$$u \frac{\partial k}{\partial x} + v \frac{\partial k}{\partial y} = \frac{\partial}{\partial x} \left[ \frac{\nu_t}{\sigma_k} \left( \frac{\partial k}{\partial x} \right) \right] + \frac{\partial}{\partial y} \left[ \frac{\nu_t}{\sigma_k} \left( \frac{\partial k}{\partial y} \right) \right] + P - \varepsilon. \quad (3.46)$$

The turbulent production term  $\tau_{ij} \frac{\partial U_i}{\partial x_j}$ , as explained above and in Eq. 3.30, is denoted short with  $P$  here. The variables for  $x$ ,  $y$ ,  $u$  and  $v$  are replaced according to Eqs. 3.38 and 3.39, the equation is then multiplied by  $\frac{c}{w_0^3}$ , leading to

$$u^* \frac{\partial k^*}{\partial x^*} + v^* \frac{\partial k^*}{\partial y^*} = \frac{\partial}{\partial x^*} \left[ \frac{1}{\sigma_k Re_{0,t}} \left( \frac{\partial k^*}{\partial x^*} \right) \right] + \frac{\partial}{\partial y^*} \left[ \frac{1}{\sigma_k Re_{0,t}} \left( \frac{\partial k^*}{\partial y^*} \right) \right] + P^* - \varepsilon^* \quad (3.47)$$

with

$$k^* = \frac{k}{w_0^2} \quad (3.48) \quad \varepsilon^* = \frac{\varepsilon c}{w_0^3} \quad (3.49)$$

$$P^* = \frac{Pc}{w_0^3} \quad (3.50) \quad \frac{1}{Re_{0,t}} = C_\mu \frac{k^{*2}}{\varepsilon^*} \quad (3.51)$$

In the transport equation for the dissipation rate  $\varepsilon$ , the relevant variables are replaced by their nondimensional forms as above. Again, the High-Reynolds number formulation is used. Going out from the dimensional form

$$u \frac{\partial \varepsilon}{\partial x} + v \frac{\partial \varepsilon}{\partial y} = \frac{\partial}{\partial x} \left[ \frac{\nu_t}{\sigma_\varepsilon} \left( \frac{\partial \varepsilon}{\partial x} \right) \right] + \frac{\partial}{\partial y} \left[ \frac{\nu_t}{\sigma_\varepsilon} \left( \frac{\partial \varepsilon}{\partial y} \right) \right] + C_1 \frac{\varepsilon}{k} P - C_2 \frac{\varepsilon^2}{k} \quad (3.52)$$

and dividing the nondimensional form by  $\frac{c^2}{w_0^4}$  this leads to

$$u^* \frac{\partial \varepsilon^*}{\partial x^*} + v^* \frac{\partial \varepsilon^*}{\partial y^*} = \frac{\partial}{\partial x^*} \left[ \frac{1}{\sigma_\varepsilon Re_t} \left( \frac{\partial \varepsilon^*}{\partial x^*} \right) \right] + \frac{\partial}{\partial y^*} \left[ \frac{1}{\sigma_\varepsilon Re_t} \left( \frac{\partial \varepsilon^*}{\partial y^*} \right) \right] + C_1 \frac{\varepsilon^*}{k^*} P^* - C_2 \frac{\varepsilon^{*2}}{k^*}. \quad (3.53)$$

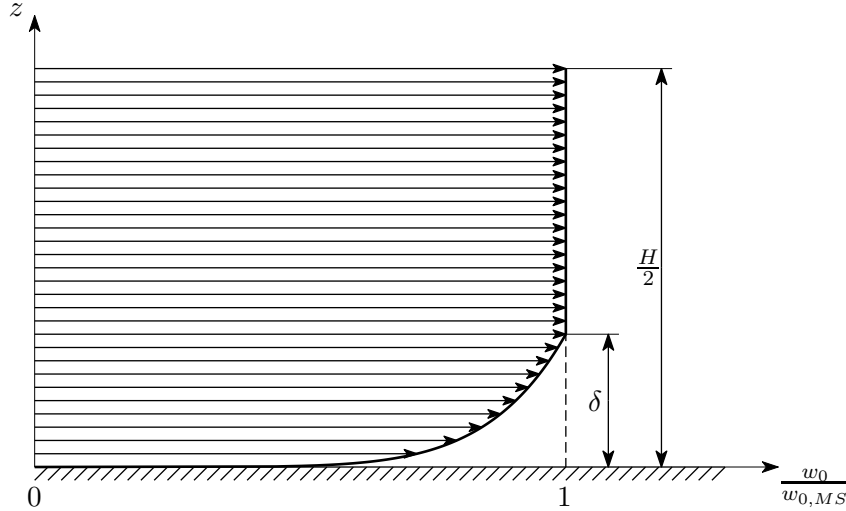


Figure 3.9: Velocity Inlet: 1/7 Power Law

To simulate the boundary conditions for the velocity at the inlet, the flow inside the boundary layer of the endwall was approximated by means of the 1/7 power law which, in its dimensional form, reads as

$$\frac{w_0}{w_{0,MS}} = \left(\frac{z}{\delta}\right)^{\frac{1}{7}}. \quad (3.54)$$

Outside of the boundary layer, in the freestream region the velocity was set equal to the velocity at the symmetric boundary, denoted as  $w_{0,MS}$ . A sketch of these conditions is given in Fig. 3.9

The flow angle at the blade inlet was set to  $\beta_0 = \beta_0' = 76.1^\circ$ , defined in [29], so the velocities in the coordinate directions are

$$w_{0,x} = w_0 \sin(\beta_0) \quad w_{0,y} = w_0 \cos(\beta_0) \quad w_{0,z} = 0$$

for zero incidence. This is sketched in Fig. 2.11.

To solve the equations for the computational domain, it was chosen to use the segregated solver scheme of ANSYS<sup>©</sup> Fluent due to its robustness. The segregated solver solves the equations for continuity and momentum sequentially whereas its counterpart, the so-called coupled solver<sup>6</sup>, would solve these equations simultaneously. The equations for scalars such as the turbulent kinetic energy  $k$  or the turbulent dissipation  $\varepsilon$  are solved sequentially as well. Both schemes use the Finite Volume method to solve the relevant

<sup>6</sup>Test calculations were performed and evaluated with the coupled solver using the explicit and implicit linearisation scheme. Convergence could not be reached reliably.

equations. Both discretisation schemes, viz. First-Order Upwind Scheme and Second-Order Upwind Scheme were used during iteration. The First-Order Upwind Scheme gives results of the deducted algebraic equations of first order accuracy, meaning that the values of flow quantities in the cell centers are set equal to the values at the faces in the upwind cells. In general, calculations done with the First-Order Upwind Scheme, tend to converge quicker. The Second-Order Upwind Scheme is of higher order accuracy, meaning that the value of a flow quantity at the face of an upwind cell is calculated with the value at cell center of the upwind cell and a Taylor-series approximation of the gradient between the cell center of the upwind cell and the face centroid. In this work, the First-Order Upwind Scheme was used for the first 250 iterations, then the discretisation scheme was switched to the Second-Order upwind scheme. The number of iterations was set to be constant at 750 for all calculations, as test calculations before starting the optimisation loop showed, that the 3D CFD calculations were well converged after that number of iterations.

## 3.4 Optimisation Loop

The optimisation loop was programmed in C programming language. The basic operating scheme of the loop is illustrated in Fig. 3.10.

The loop was initialized with the initial population from Tab. 3.1, after that, a mesh was constructed in ANSYS Gambit<sup>©</sup> for each configuration. Following that, the mesh was loaded into ANSYS Fluent<sup>©</sup> where the boundary conditions were defined, that is the relevant equations, the relevant constants and functions at the boundaries were set. The numeric calculations were done in nondimensional form, so the units for all variables are equal to unity.

The solution space with the initial configurations is shown in Fig. 3.11. It is imperative to do some CFD test calculations for extreme configurations <sup>7</sup> before starting the automatic optimisation process, in order to secure, that convergence is reached for those extreme configurations.

For this work, those initial test calculations were done for the configurations

- $\alpha = 45^\circ, h = 0$  mm, and
- $\alpha = -45^\circ, h = 0$  mm.

Those configurations proved to converge in the CFD calculations.

---

<sup>7</sup>”Extreme” is used in the sense, that these configurations form the border of the solution space, and therefore the behaviour of the calculations at these borders had to be checked for convergence.

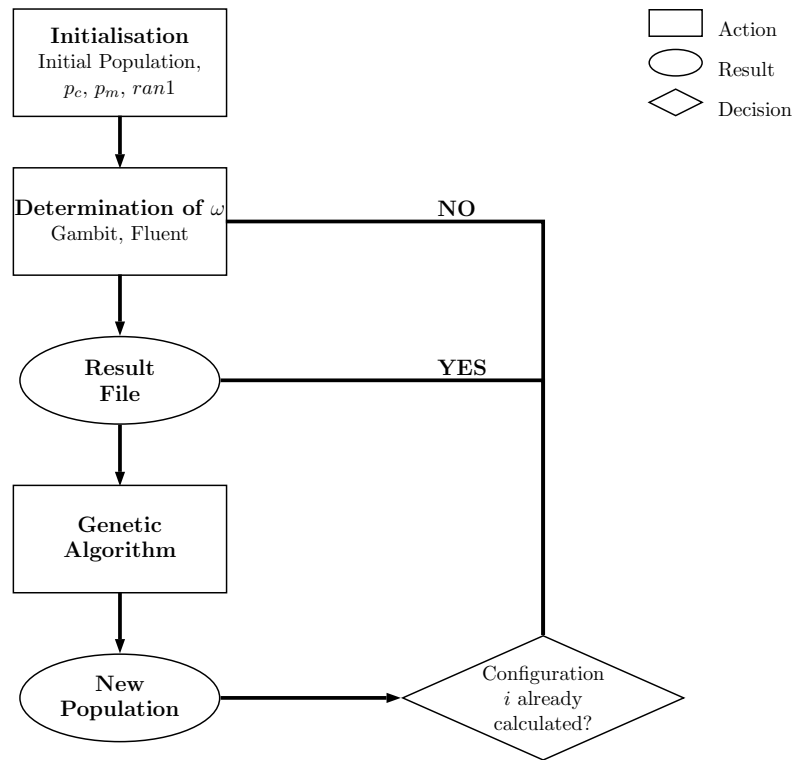


Figure 3.10: Flow Chart of Optimisation Loop

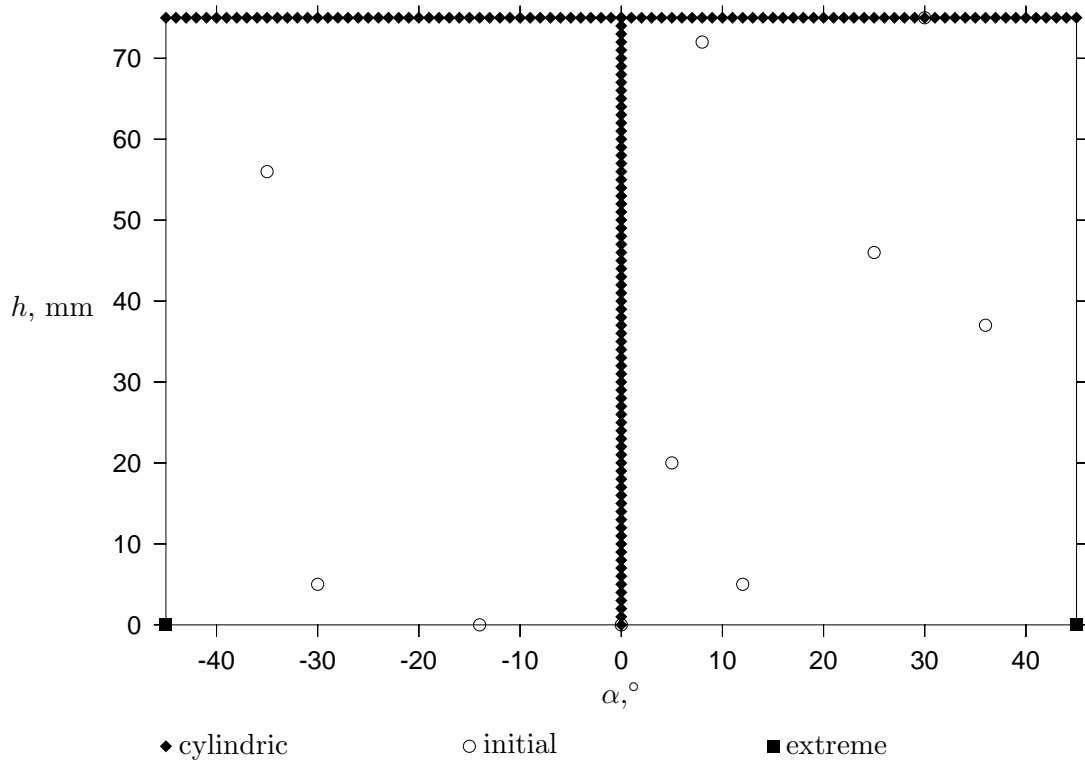


Figure 3.11: CFD Solution Space

### 3.4.1 Convergence and Reliability Check of the Solutions

Convergence for a steady state calculation, as was performed here for every configuration calculated, means, that the solution of the problem does not significantly change any more as iterations progress forward. It is in general a difficult task to judge, whether a solution is converged or not after a certain number of iterations (compare [1]). In this work, two approaches were chosen to judge, whether a solution of a configuration is converged or not. The first criterion for a solution to be converged was the level of scaled residuals. This level was set to be lower than  $1 \cdot 10^{-5}$ , which is two orders of magnitude lower than generally accepted as criterion for convergence<sup>8</sup>. This criterion was checked for a sample of configurations during and after the optimisation. As mentioned above, to ensure the convergence for "extreme" configurations, test calculations of those configurations were performed and evaluated before starting the optimisation process. The second criterion used was the calculated lift force of the blade. The nondimensional lift force of the blade was calculated at each iteration of the CFD calculation and each value was stored in a file. The mean value of lift force was calculated out of the last 50 iteration values and then compared to the value of lift force of the very last iteration. The difference had to

<sup>8</sup>A general rule is, that the level of the scaled residuals for a converged solution should be three orders of magnitude lower than at the beginning of the iterations. Here, scaled residuals at the beginning of iteration were about the order of magnitude  $1 \cdot 10^0$ .

### 3 Optimisation

$\alpha, ^\circ$	$h, \text{ mm}$
$-20 \leq \alpha \leq -10$	$66 \leq h \leq 74$
$20 \leq \alpha \leq 38$	$50 \leq h \leq 67$

Table 3.2: Approximate Regions of Local Optima

be below  $\pm 1 \cdot 10^{-4}$  <sup>9</sup>.

#### 3.4.2 Result of Optimisation

The contour plot of the total pressure loss coefficient  $\omega$  of all configurations calculated during the optimisation process and their results, respectively, are presented in Fig. 3.12.

Each point represents one configuration. Nearly 1250 configurations were calculated during the optimisation process. The initial configurations are not specially marked in this plot. Contrary to Fig. 3.11 the cylindric configurations are marked with an empty instead of a filled diamond symbol, as otherwise it would have been difficult to distinguish them from the other calculated configurations. It can be observed quite clearly, that the genetic algorithm concentrated its search in regions, where there seem to be local optima, as substantially more configurations were calculated and evaluated in those regions. Those regions are summarized in Tab. 3.2.

The region of the best solution is marked with the dashed isoline of  $\omega$ , the value of the isoline would be 0.067 there and was not plotted for the contour plot to stay consistent in its labelling. There seems to be a region with low, positive values of  $\alpha$  and low values of  $h$  on one hand and high positive values of  $\alpha$  and high values of  $h$  on the other hand, where more efficient configurations than the cylindric ones lie within. This region can be identified between the two isolines with a value of  $\omega = 0.068$ . It is interesting to note, that apparently curved-only compound lean nozzles and compound lean nozzles with an explicit straight spanwise piece around midspan deliver similar efficiency gains for the nozzle.

The vertices of the parabolic arcs for good solutions with efficiency gains, compared to the cylindric blades, for the most instances lie in between the endwall and distance of the inlet endwall boundary layer thickness. This is an interesting fact that could be observed.

Finally, it should be mentioned, that the optimisation algorithm worked flawlessly without any mistake until interrupted manually after roughly 1250 configurations calculated.

---

<sup>9</sup>It shall be annotated, that this is in fact a very low value, as the whole calculation was performed on a nondimensional basis

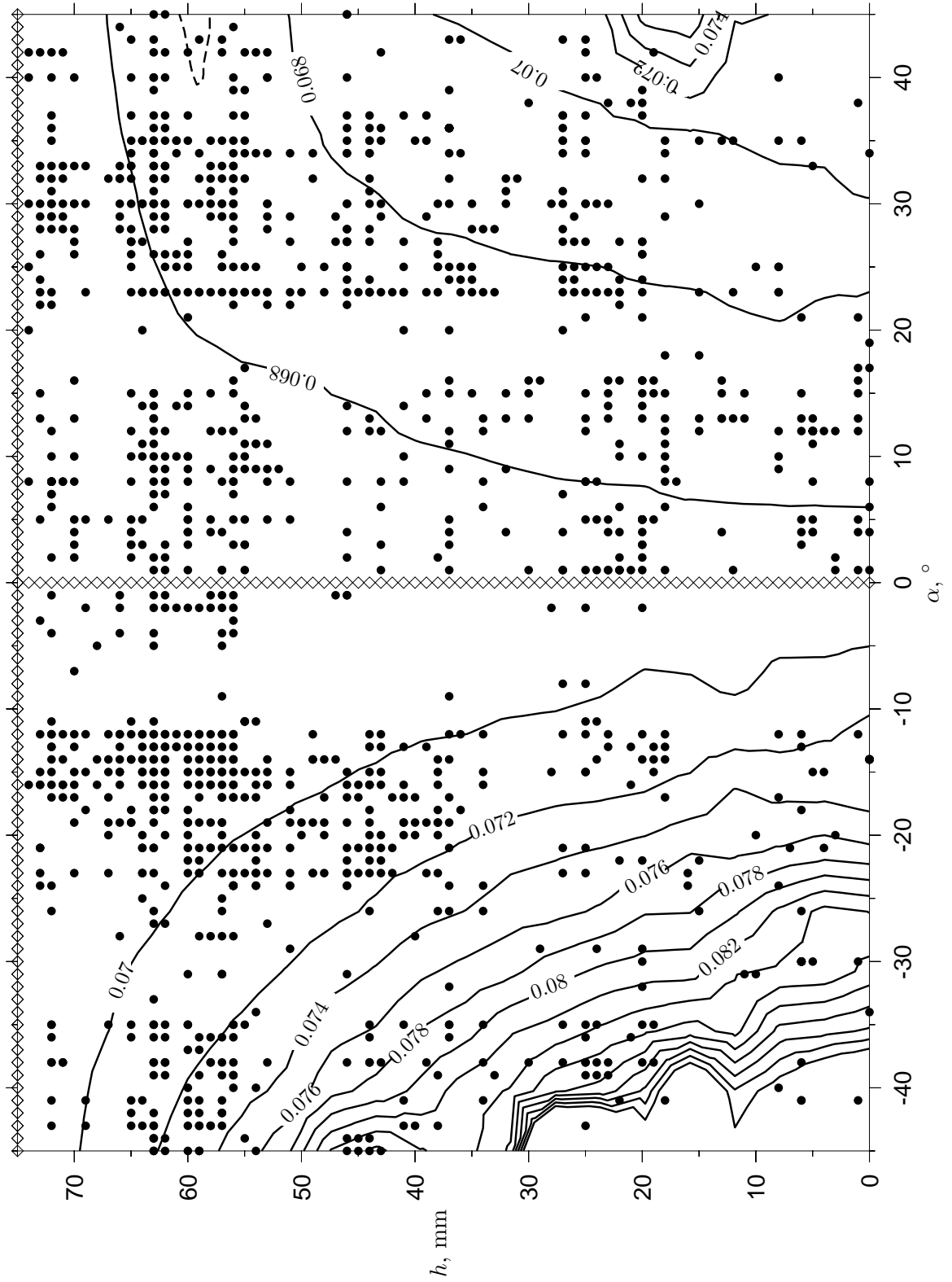


Figure 3.12: Contour Plot of Total Pressure Loss Coefficient  $\omega$  of Optimisation

## 4 Results

An expert is a man who has  
made all the mistakes which can  
be made in a very narrow field.

---

*(Niels Bohr,  
Danish Physicist)*

### 4.1 Comparison of Experiment and CFD Calculation

The results of the experiment were presented and discussed in Chap. 2.5 for the three-hole pressure probe (2D measurement), in Chap. 2.6 for the five-hole pressure probe (3D measurement) and in Chap. 2.7 for the blade profile pressure measurement. Comparing these results with the results of the CFD calculations, qualitatively and quantitatively, should be helpful, when judging the results of the CFD optimisations.

#### 4.1.1 Exit Flow Angles: Pitchwise Flow Angle $\beta_1$ and Spanwise Flow Angle $\gamma_1$

It is of utmost importance for turbomachine designers, to know the flow angles between the blade rows as exactly as possible. One of the most important tools for the design process, the velocity triangle, could not be applied without knowledge of flow angles. The comparison of the pitchwise flow angle,  $\beta_1$ , for the 2D experiment with the three-hole pressure probe and the CFD calculation at midspan is depicted in Fig. 4.1.

It can be observed very well, that, qualitatively the results are very good. Quantitatively, however, there seems to be some kind of "offset" between the results. A possible explanation is, that this offset originates of the experimental setup in the laboratory; four coordinate systems are used (sketched in Fig. 4.2) in the setup, viz.

- the "natural" coordinate system (CS\_1),
- the coordinate system attached to the windtunnel (CS\_2),
- the coordinate system attached to the mounting box (CS\_3), and
- the coordinate system attached to the traversing unit (CS\_4).

Unfortunately, not all the relations between those coordinate systems can be measured exactly, neither can all those coordinate systems be setup independently of each other. So, according to the rules of error propagation, the offset of about  $1.3^\circ$  has to be accepted

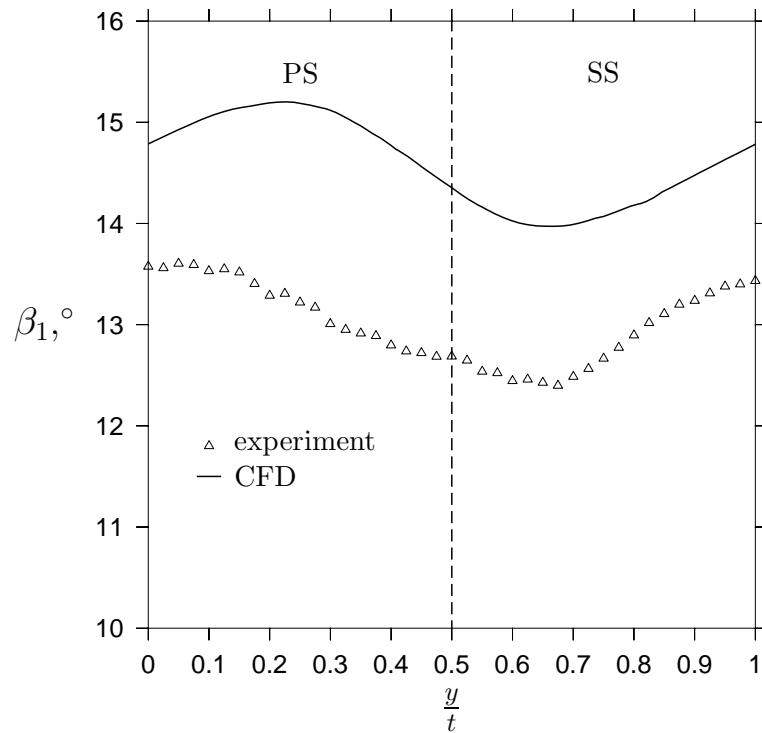


Figure 4.1: Comparison of Experiment and CFD Calculation: Three-Hole Pressure Probe, Pitchwise Exit Flow Angle  $\beta_1$  at Midspan

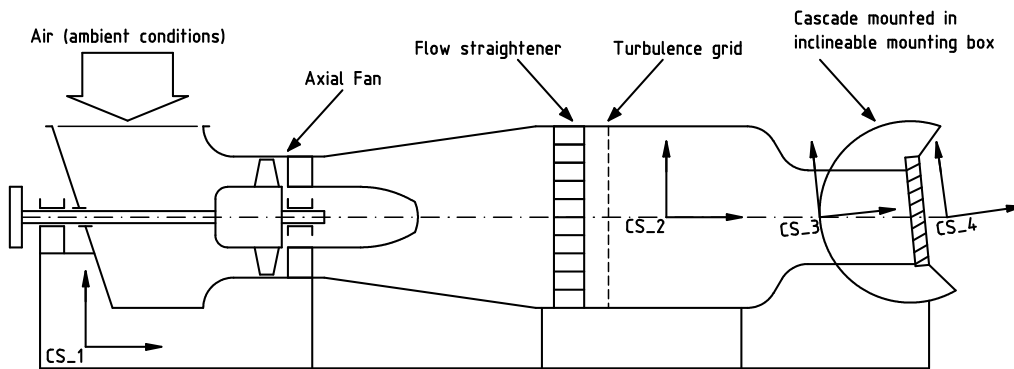


Figure 4.2: Four different Coordinate Systems for the Experiment

## 4 Results

as a systematic error, and can, at this point, not be decreased. Given the difficulties explained above, this error seems to be rather small.

The comparison for the 3D measurement and the corresponding CFD calculation is presented in Fig. 4.3. Again, at midspan, the measurement with the five-hole pressure probe shows very good agreement with the measurement with the three-hole pressure probe. The same offset as described above can be observed. Qualitatively the pitchwise flow angle  $\beta_1$  is predicted quite well with CFD, the phenomena overturning at the endwall and underturning in the region of the loss core can be identified quite clearly and at the same positions as in the experiment. However, the offset for the measurement remains, has even become higher, and cannot be overcome here. In addition, due to the class-building process, that is necessary for preparation of the contour plot, a certain level of inaccuracy has to be accepted <sup>1</sup>.

The comparison of measured and calculated spanwise flow angle  $\gamma_1$  is depicted in Fig.4.4.

Even qualitatively the agreement between experiment and CFD calculation is rather poor for the spanwise flow angle  $\gamma_1$ . For both,  $\gamma_1$  taken together with the contour plot of the pitchwise flow angle  $\beta_1$ , the helical motion of the passage vortex (compare Chap. 2.6 for further explanation) can be detected. As both, the pitchwise flow angle  $\beta_1$  and the absolute values of the spanwise flow angle  $\gamma_1$  are larger in the CFD calculation, the passage vortex is identified to be weaker in the experiment and stronger in the CFD calculation. This fact coincides with the above mentioned fact, that the loss is overestimated in the CFD calculation due to the used Standard  $k/\varepsilon$  turbulence model, as a stronger passage vortex means higher secondary losses. The reasons for the bad agreement of the spanwise flow angle between experiment and CFD calculation could not be determined.

### 4.1.2 Static Pressure Coefficient $C_{p,1}$

The static pressure coefficient  $C_{p,1}$  in the context here cannot be used for any relevant conclusion as far as turbomachinery applications are concerned, but it can serve as a tool for judging the quality of agreement of the experiment and the CFD calculation. As such, it shall be used, only the 2D measurement is evaluated here. The static pressure coefficient is defined as

$$C_{p,1} = \frac{p_1 - \bar{p}_{0,MS}}{\bar{p}_{t0,MS} - \bar{p}_{0,MS}} \quad . \quad (4.1)$$

The comparison is depicted in Fig. 4.5.

As can be seen, the agreement is excellent qualitatively, quantitatively the deviation between experiment and CFD calculation is less than 3%, which is considered to be a

---

<sup>1</sup>The term "level of inaccuracy" relates to the graphical representation, the contour plot, not to the actual data, which is as accurate as can be.

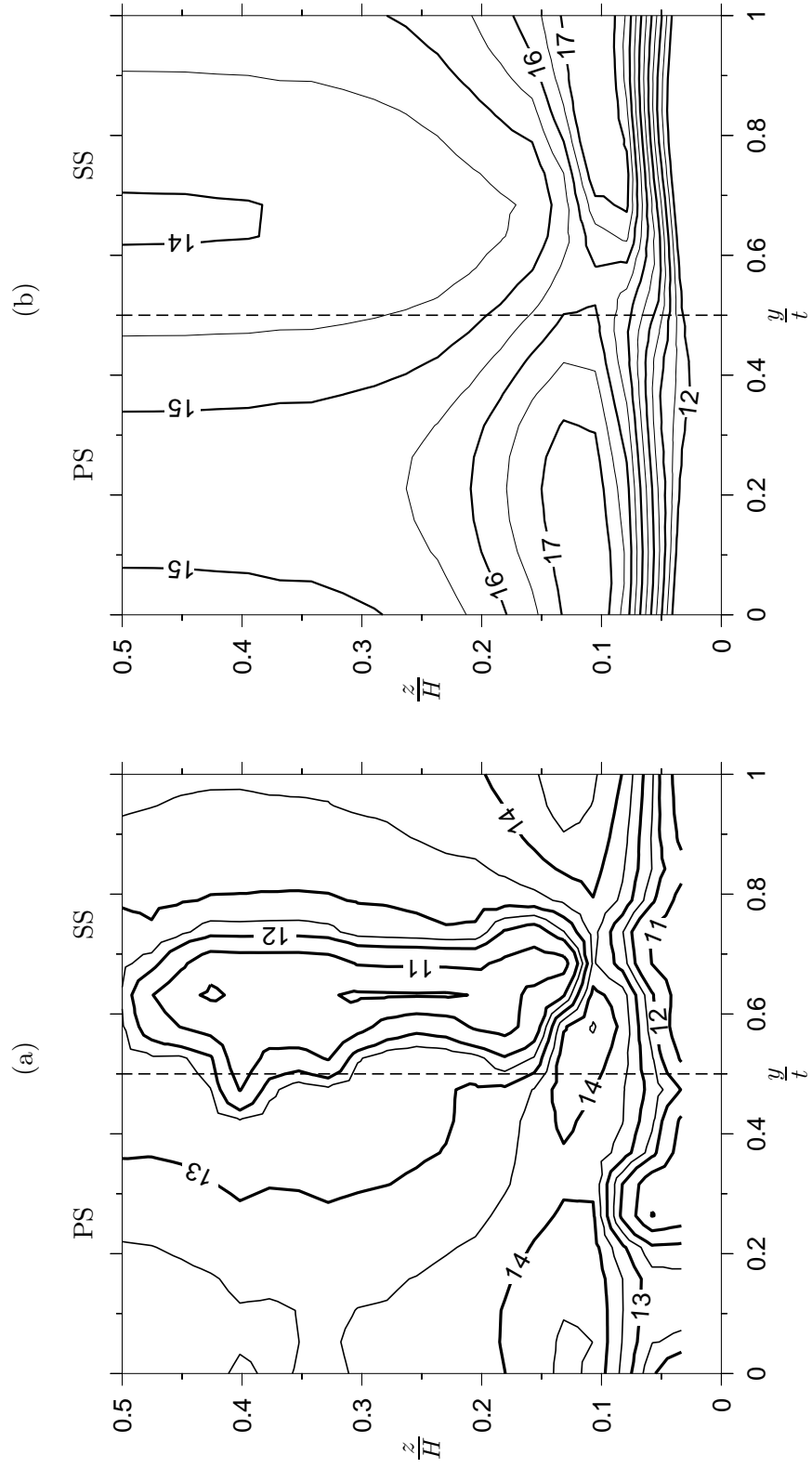


Figure 4.3: Comparison of Experiment (a) and CFD Calculation (b): Five-Hole Pressure Probe, Pitchwise Exit Flow Angle  $\beta_1$

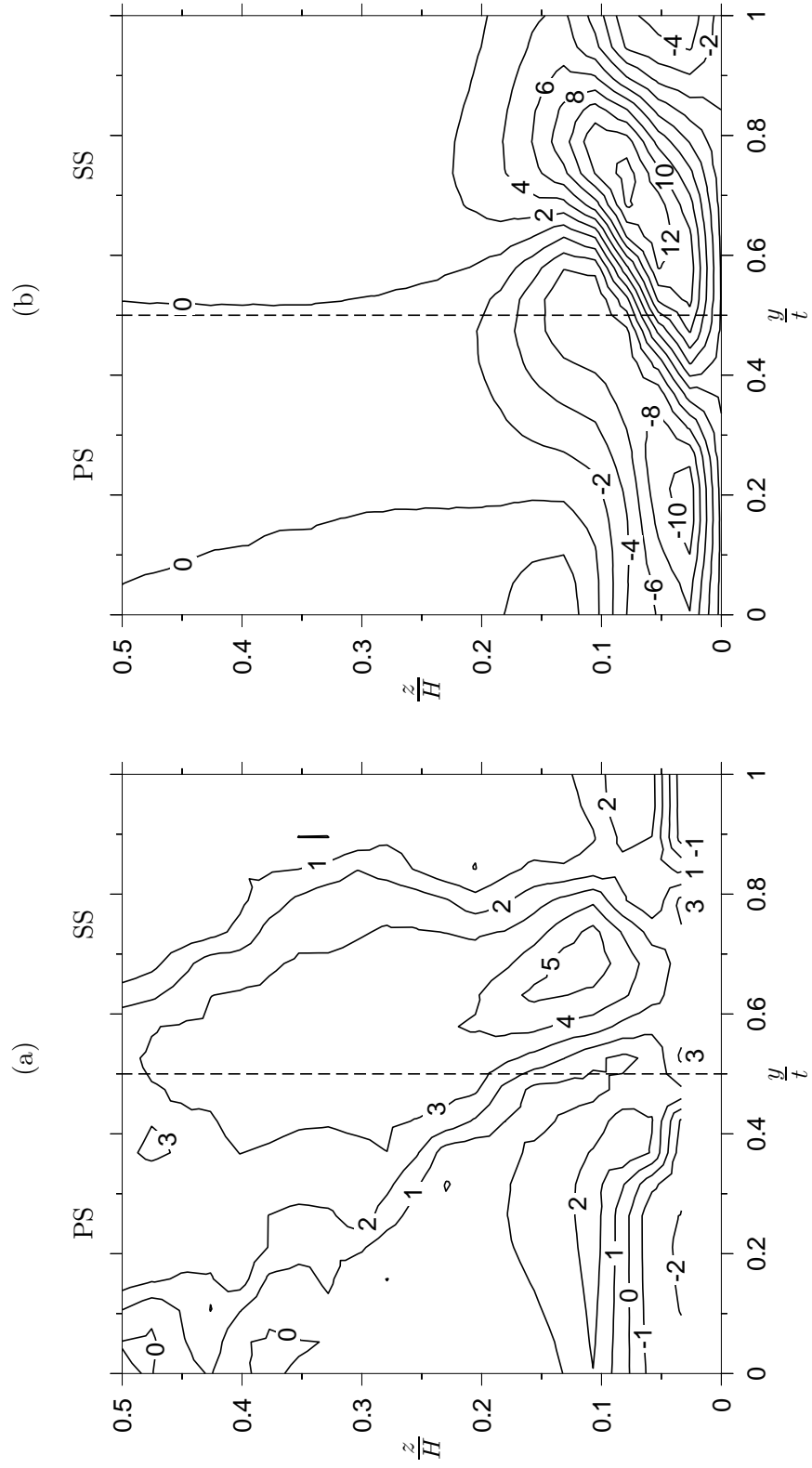


Figure 4.4: Comparison of Experiment (a) and CFD Calculation (b): Five-Hole Pressure Probe, Spanwise Exit Flow Angle  $\gamma_1$

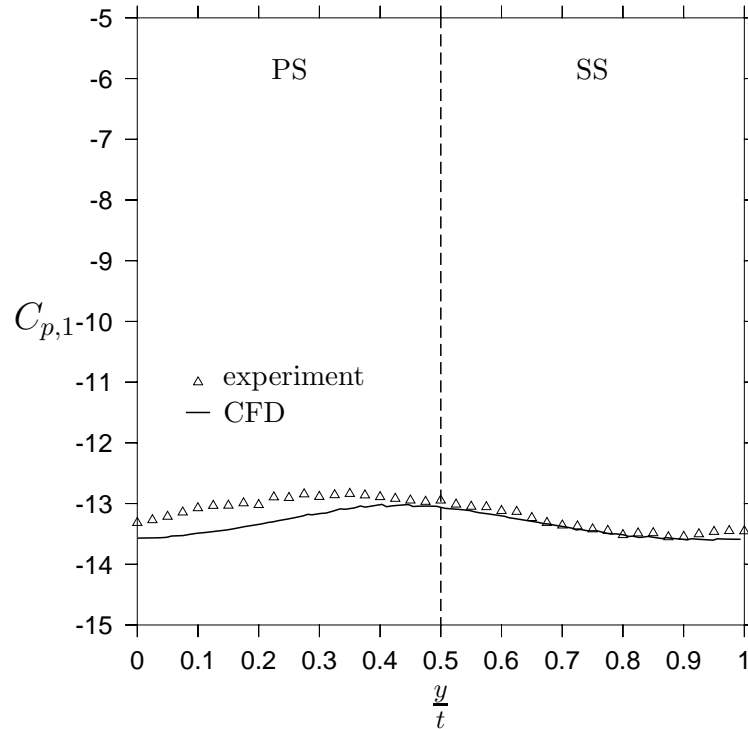


Figure 4.5: Comparison of Experiment and CFD Calculation: Three-Hole Pressure Probe, Static Pressure Coefficient  $C_{p,1}$  at Midspan

very good agreement.

#### 4.1.3 Exit Flow Velocity $w_1$

The exit flow velocity  $w_1$  is depicted in normalized form, namely  $\frac{w_1}{w_0}$ , for the exit plane at midspan in Fig. 4.6. As was the case with the static pressure coefficient, no relevant conclusion in terms of turbomachinery flow can be drawn from this flow property, but it is again used to better judge the results of the CFD calculation compared to the experiment.

As can be seen, the agreement is quite good in the blade passage in the region of undisturbed flow, however, it is better for the flow near the suction side of the blade than for the flow near the pressure side. Qualitatively, the velocity plot shows quite good agreement, quantitatively this is not the case in the region around the wake of the blade. This phenomenon could result from usage of the Standard  $k/\varepsilon$  turbulence model. Durbin [8] points out, that the Standard  $k/\varepsilon$  turbulence model predicts an anomalously large growth of turbulent kinetic energy  $k$  in stagnation point flows, and this behaviour can also affect the whole flow computation, even if the flow around the stagnation point region is not of particular interest per se. Flow around a turbine blade is such a flow. He called this phenomenon the stagnation point anomaly.

## 4 Results

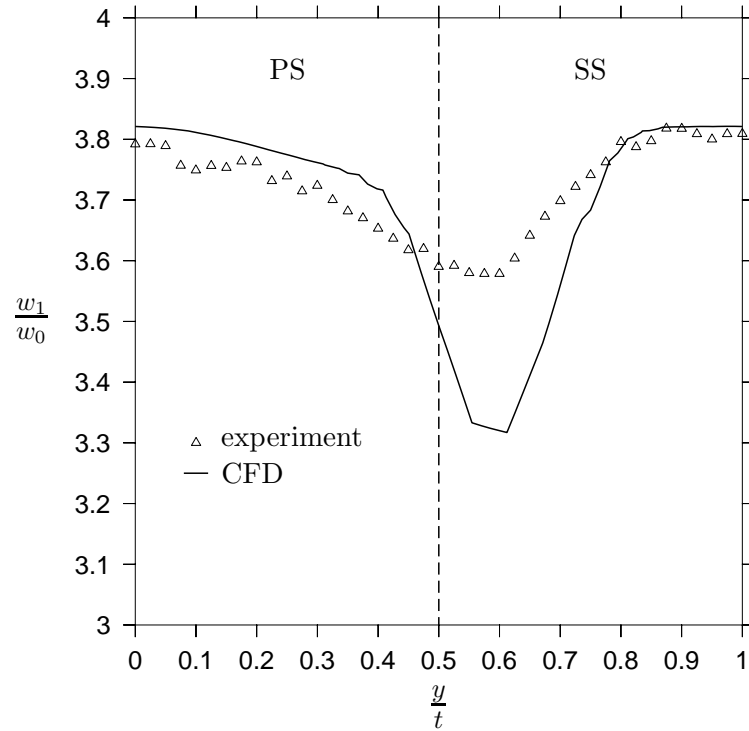


Figure 4.6: Comparison of Experiment and CFD Calculation: Three-Hole Pressure Probe, Cascade Exit Flow Velocity Ratio at Midspan

### 4.1.4 Total Pressure Coefficient $C_{p,t1}$

Figure 4.7 shows the values of  $C_{p,t1,MS}$  for the 2D experiment and the values for the CFD calculation, evaluated in the wake of the blade cascade at an axial position of 130% axial chord length  $b$ , calculated from the coordinate origin, depicted in Fig. 3.5, at midspan.

As can be seen, CFD shows very good results when predicting the total pressure in regions of undisturbed flow, viz. downstream of the middle of the blade passage. However, in the region of approximately  $0.45 \leq \frac{y}{t} \leq 0.8$ , where the wake of the blade can be seen clearly, as  $C_{p,t1,MS}$  reaches its minimum value, the result of the CFD calculation clearly predicts a much lower total pressure coefficient than the experiment. Qualitatively, the results are quite good, but quantitatively, this is not the case. One possible reason for this might be due to the usage of the Standard  $k/\varepsilon$  turbulence model, as assumed in Chap. 4.1.3. The overestimation of total pressure loss seems to be caused by the influence the stagnation point anomaly has on the velocities of the flow. The total pressure is the sum of the static and dynamic pressure. The results for the static pressure of the calculation were excellent, compared to the experiment, quantitatively and qualitatively (compare Fig. 4.5). The agreement of results between experiment and calculation of the exit flow velocity ratio was good qualitatively, but poor quantitatively, as the velocity was predicted to be much too low in the region around the blade wake, therefore the portion of dynamic pressure for the total pressure is too low as well. This results in a lower total pressure and therefore

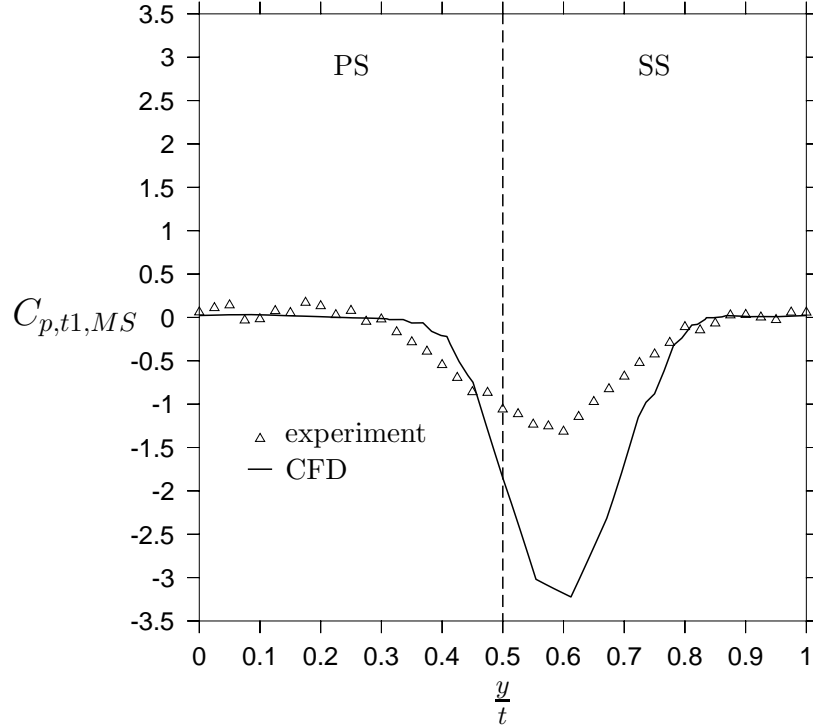


Figure 4.7: Comparison of Experiment and CFD Calculation: Three-Hole Pressure Probe, Total Pressure Coefficient  $C_{p,t1,MS}$

in a higher total pressure loss coefficient.

Walters and Leylek [41] examined the impact of film-cooling jets on turbine aerodynamic losses by means of CFD, comparing their results to experimental data. Although this specific result is not important here, their findings on the influence of turbulence modelling on the losses produced inside a blade cascade can be used to support the assumption, that the higher loss of the CFD calculation compared to the experiment in this work originate, at least partly, from the application of the Standard  $k/\varepsilon$  model. For their low-speed cascade ( $Re_c = 2.3 \cdot 10^5$ , exit Mach number  $Ma = 0.06$ ), they found out, that for a solid blade, without injection of cooling air, the Standard  $k/\varepsilon$  model overpredicted the experimental results of the total pressure loss coefficient by nearly 54%. They achieved results, that were somewhat closer to those of the experiment with the Renormalization group  $k/\varepsilon$  model (RNG  $k/\varepsilon$ ), the realizable  $k/\varepsilon$  model (RKE) and the full Reynolds-Stress model (RSM), viz. nearly 26%, nearly 2% and approximately -1% respectively.

The comparison of 3D results (130% axial chord length) for  $C_{p,t1}$  is depicted in Fig. 4.8.

As can be seen, the results at midspan are comparable qualitatively and quantitatively to those of the 2D measurement. The region of undisturbed flow can be identified very clearly in both pictures, the agreement between measurement and CFD calculation is very close. This region extends from  $\frac{z}{H} \approx 0.15$  to  $\frac{z}{H} = 0.5$  in spanwise direction and from  $0 \leq \frac{y}{t} \leq 0.25$  and  $0.8 \leq \frac{y}{t} \leq 1$  in pitchwise direction. When approaching the endwall

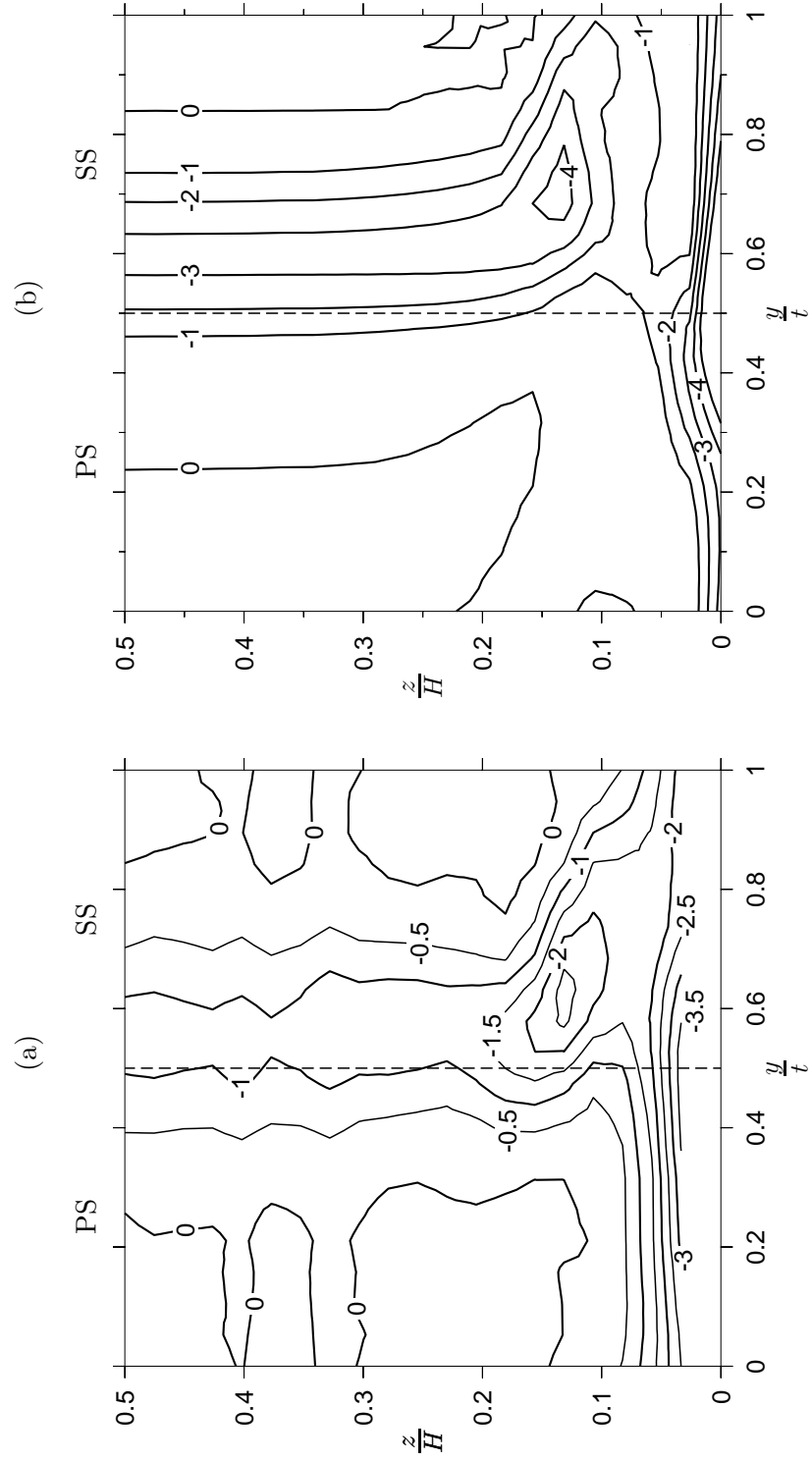


Figure 4.8: Comparison of Experiment (a) and CFD Calculation (b): Five-Hole Pressure Probe, Total Pressure Coefficient  $C_{p,t1}$

region ( $\frac{z}{H} \rightarrow 0$ ), the increasing of  $C_{p,t1}$  shows the influence of the endwall boundary layer in this region, which somehow extends further in spanwise direction in the experiment. It should be mentioned, that, for practical reasons, the mounting box of the blade cascade ended just in front of the traversing shaft of the five hole pressure probe, whereas in the CFD calculation, the endwall continued beyond this point until the pressure outlet. This might be a reason for different extension of the endwall boundary layer in that region. The isobar lines in nearly spanwise direction from  $0.2 \leq \frac{z}{H} \leq 0.5$  with total pressure coefficients lower than zero can be interpreted as profile loss of the blade. The passage vortex with its loss core at  $\frac{y}{t} \approx 0.6$  and  $\frac{z}{H} \approx 0.15$  can also be clearly identified in experiment and CFD calculation. As with the results of the 2D experiment, the comparison of the results of 3D experiment and CFD calculation show a higher general level of loss for the CFD calculation, which, as in the 2D case, can partly be explained with the stagnation point anomaly of the Standard  $k/\varepsilon$  turbulence model.

#### 4.1.5 Profile Static Pressure at Midspan

The comparison of experiment and CFD calculation of the static profile pressure at midspan is presented in Fig. 4.9. The calculation for  $C_p$  for the experiment was introduced in Chap. 2.7. For the calculation of the CFD values,

$$C_p = \frac{p - \bar{p}_{0,MS}}{\bar{p}_{t0,MS} - \bar{p}_{0,MS}} \quad (4.2)$$

is used. Equation 4.2 is more or less equal to the definition used for the experiment, but for the sake of exactness, the mass-averaging process used for the CFD evaluation is expressed by the overbar symbols.

The agreement between the results of the experiment and the calculation is very good, qualitatively and quantitatively. In the zone of diffusion on the suction side, the pressure in the calculation was predicted to be lower, than could be observed in the experiment. On the pressure side, in the zone where the fluid is accelerated again, the pressure was predicted to be lower than the experiment showed. However, the bladeload, represented by the area between the pressure side curve and the suction side curve stayed the same more or less.

## 4.2 Results of the CFD Optimisation

At the end of the optimisation process, a huge number of 3D CFD solutions was calculated (compare Fig. 3.12). Two of the best solutions, viz. the very best and the fourth-best solution are evaluated and compared. The best solution has an angle  $\alpha$  of  $43^\circ$ , which might be tough or impossible to manufacture due to reasons of mechanical strength. Therefore, the second configuration was chosen to be as close as possible to the "optimum"

## 4 Results

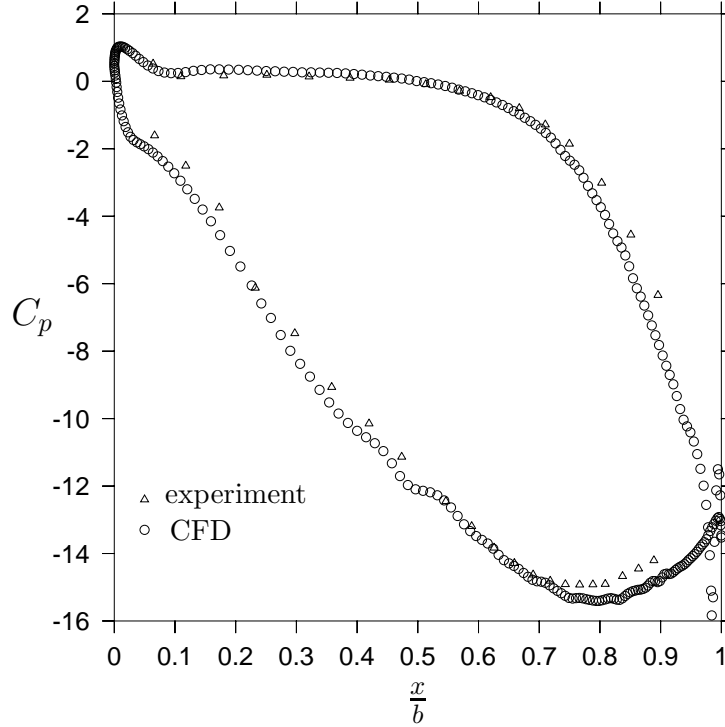


Figure 4.9: Comparison of Experiment and CFD Calculation: Static Profile Pressure Coefficient  $C_p$  at Midspan

	$\alpha, ^\circ$	$h, \text{ mm}$	$\frac{h}{H}$	$\omega$	$\frac{\omega}{\omega_{Set1}}$
Set 1	0	75	0.5	0.06864	1.0000
Set 2	15	1	$\approx 0$	0.06760	0.9848
Set 3	43	59	0.4	0.06756	0.9842

Table 4.1: Geometry Parameters and Objective Functions of evaluated Configurations

solution, speaking in terms of total pressure loss coefficient, but to have a substantial lower value of  $\alpha$ . Table 4.1 shows the basic geometrical data of those compound lean configurations and their absolute and relative total pressure loss coefficient in comparison with the initial cylindrical blade configuration.

It is interesting to note, that the best configuration, Set 3, is a classical compound lean configuration, with an explicit straight part in the middle section of the blade, but the second configuration, Set 2, is a configuration which is nearly a curved-only configuration. Both, Set 2 and Set 3, show an improvement of total pressure coefficient of about 1.5%. However, significant differences can be observed regarding the flow distribution and flow angles.

### 4.2.1 Local Total Pressure Coefficient $C_{p,t1}$

Figure 4.10, Fig. 4.11 and Fig. 4.12 show contour plots of the total pressure coefficient  $C_{p,t1}$  of the three blade sets compared to one another at a streamwise position of 130% axial chord length ("Measuring Plane" in Fig. 3.5). The dashed line represents the stacking line of the blade profiles of the individual blades.

Profile losses, represented by the isobar lines with a local total pressure coefficient  $C_{p,t1}$  lower than zero in the region of approximately  $0.3 \leq \frac{z}{H} \leq 0.5$ , rise for Set 2 compared to the cylindrical blade which can be observed in Fig. 4.10. The contourlines of  $C_{p,t1}$  also adopt the shape of the stacking line of the blade profiles for Set 2. The loss core is represented by the region of the lowest values of  $C_{p,t1}$  on the suction side at a spanwise position of approximately  $0.13 \leq \frac{z}{H} \leq 0.16$  for Set 1 and approximately  $0.1 \leq \frac{z}{H} \leq 0.3$  for Set 2. It is very pronounced for Set 1. For Set 2 it splits up into two parts with a lower level of total pressure loss. Hildebrandt and Fottner [13] discovered this splitting-up for cylindrical blades in their grid refinement studies, and attributed these separate loss cores to the different vortices, the horseshoe vortex and the passage vortex. Here, it could only be observed for the compound lean blade. The level of loss of the endwall boundary layer, represented by lower absolute values of local total pressure coefficient in the endwall regions, is lower for Set 2 than for Set 1.

Comparing the contour plots of total pressure coefficient  $C_{p,t1}$  of Set 1 and Set 3, Fig. 4.11 reveals, that the profile losses, represented by the isobar lines in spanwise direction, evaluated at about  $0.5 \geq \frac{z}{H} \geq 0.3$  are roughly equal for Set 1 and Set 3. The blade wake seems to change its shape according to the stacking line for Set 3, although this behaviour cannot clearly be identified, due to the geometrical parameters of Set 3. For Set 3 the loss core is situated at a spanwise position of about  $0.11 \leq \frac{z}{H} \leq 0.26$ . Again, as for Set 2, the loss core is split up into two separate parts. The level of total pressure around the loss core again seems lower for Set 3 compared to Set 1. At the endwall, losses originating from the endwall boundary layer are also lower than for Set 1, very clearly on the pressure side of the blade, but hard to spot on the suction side.

In Fig. 4.12 finally Set 2 and Set 3 are compared with respect to the total pressure coefficient. It is evident from the observations made above, that now, the profile losses of Set 3 are lower than those of Set 2. Furthermore, the loss cores are both split up, but different in shape. Set 2 seems to have a lower level of loss in the loss core. At the endwall, the loss of both configurations seems rather comparable to each other.

Summarizing the comparison of Set 1 to Set 3, the following statements can be made:

- The optimised compound lean configurations both tend to decrease loss originating from endwall boundary layers.
- Both optimised configurations show a split up loss core, whereas for the cylindrical blade, this is not the case.

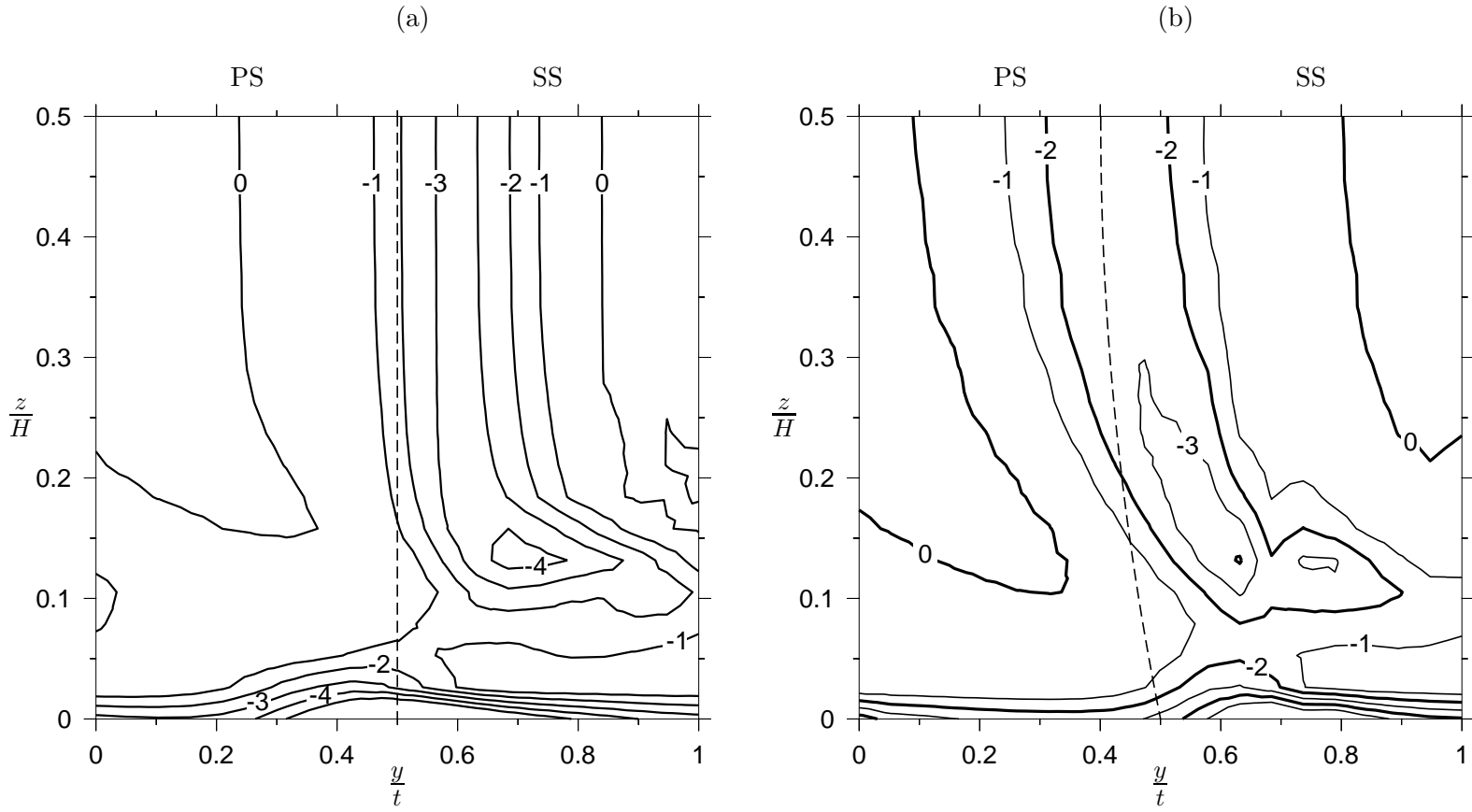


Figure 4.10: Comparison of Total Pressure Coefficient  $C_{p,t1}$  of Set 1 (a) and Set 2 (b)

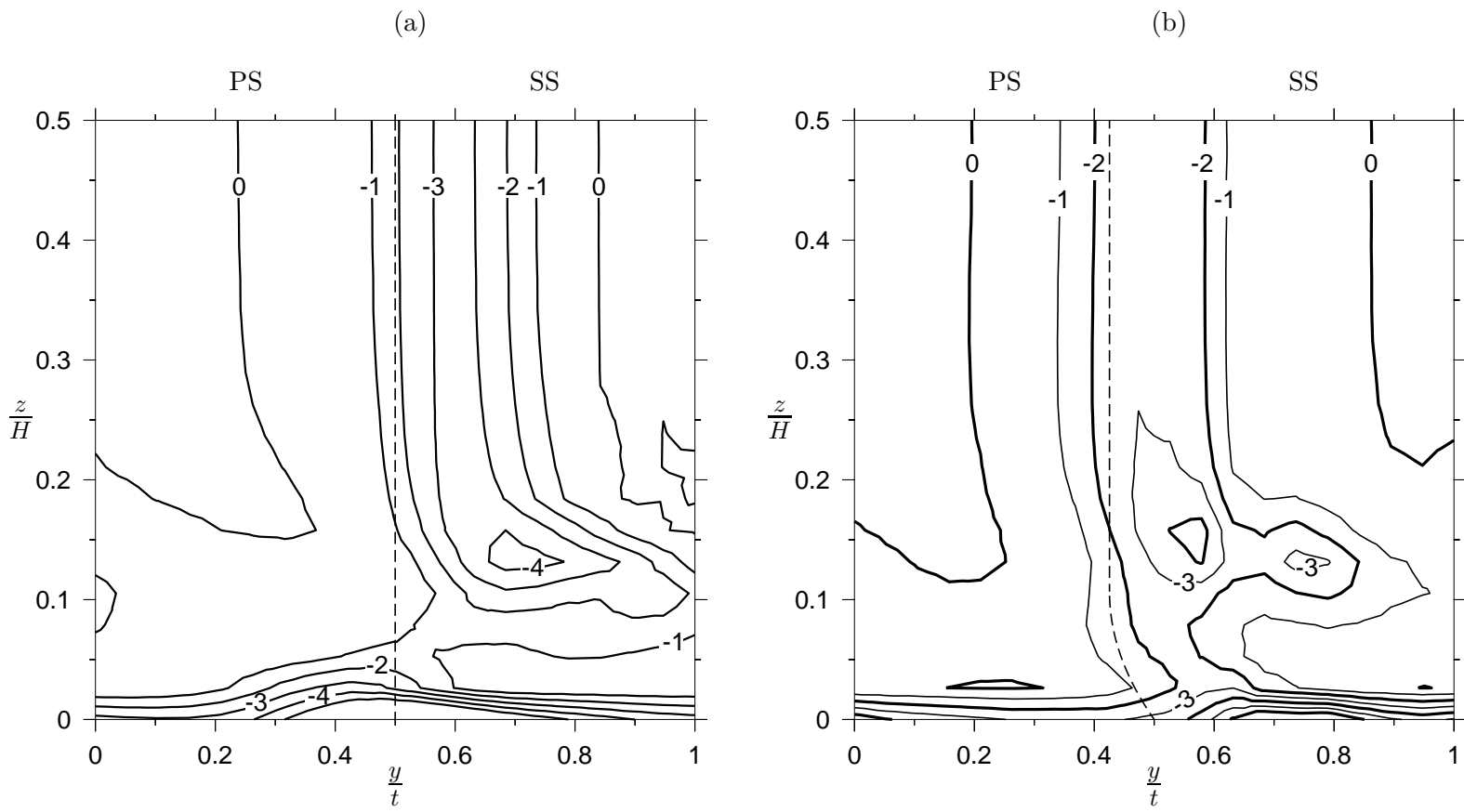


Figure 4.11: Comparison of Total Pressure Coefficient  $C_{p,t1}$  of Set 1 (a) and Set 3 (b)

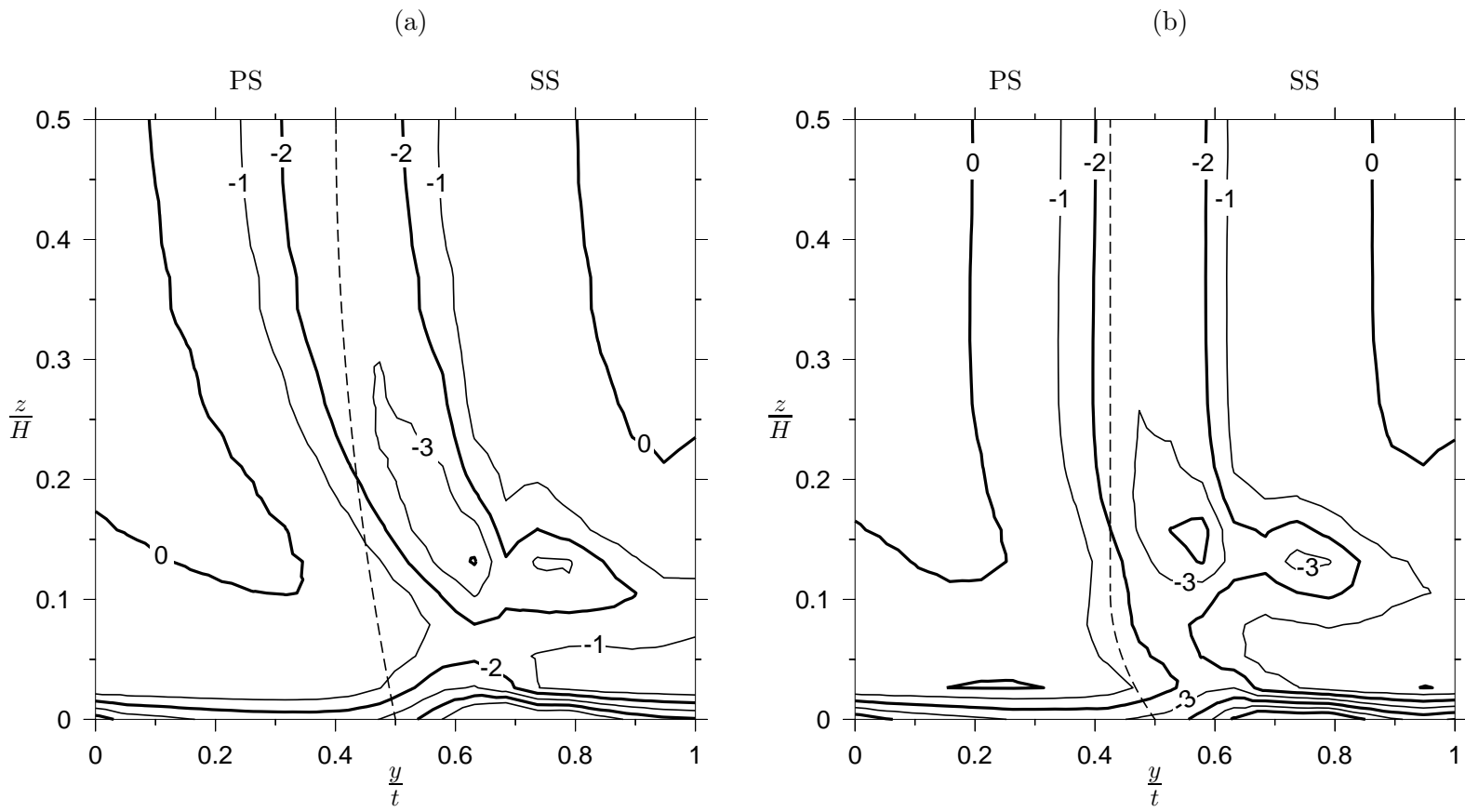


Figure 4.12: Comparison of Total Pressure Coefficient  $C_{p,t1}$  of Set 2 (a) and Set 3 (b)

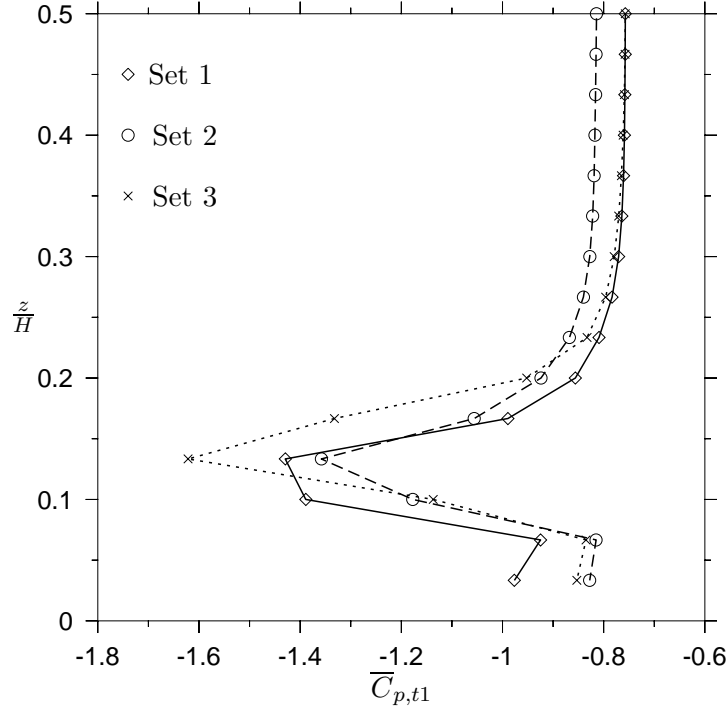


Figure 4.13: Pitchwise mass-averaged Total Pressure Coefficient  $\overline{C}_{p,t1}$

- Blade profile losses are higher for the compound lean configuration without <sup>2</sup> straight part of the blade profile stacking line around midspan, than for the cylindrical blade and the compound lean configuration with straight part of the stacking line around midspan.
- The blade wake changes its appearance according to the stacking line of the blade.

#### 4.2.2 Pitchwise mass-averaged Total Pressure Coefficient $\overline{C}_{p,t1}$

The pitchwise mass-averaged total pressure coefficient is defined by

$$\overline{C}_{p,t1} = \left[ \frac{\int_0^t C_{p,t} u \, dy}{\int_0^t u \, dy} \right]_z, \quad (4.3)$$

incompressible conditions assumed.  $\overline{C}_{p,t1}$  for different spanwise positions  $\frac{z}{H}$  is depicted vs. the nondimensional blade height  $\frac{z}{H}$  in Fig. 4.13.

The higher profile losses of Set 2 compared to Set 1 and Set 3 are confirmed here, as

<sup>2</sup>As presented in Tab. 4.1,  $\frac{h}{H}$  is not exactly zero, but very close.

can be seen by the value of  $\overline{C}_{p,t1}$  at about  $0.3 \leq \frac{z}{H} \leq 0.5$ . For Set 1 and Set 3 the profile losses are practically equal. The fact, that for  $0.3 \leq \frac{z}{H} \leq 0.5$  the value of  $\overline{C}_{p,t1}$  stays rather constant gives very strong evidence, that this region is not influenced by three-dimensional flow effects, viz. secondary flow. Near the endwall, the pitchwise mass-averaged total pressure coefficient is roughly equal and lower for both, Set 2 and Set 3, than for Set 1. This means, that both compound lean configurations produce less endwall loss due to endwall boundary layer than the cylindrical blade. In the region of the loss core, the lowest absolute value for  $\overline{C}_{p,t1}$  can be observed for Set 2. Following Tab. 4.1, both compound lean configurations have a lower total pressure loss coefficient  $\omega$  than Set 1. According to Fig. 4.13, Set 2 shows the best performance in the region of the passage vortex (loss core) and in the endwall region. However, this is somewhat balanced out by the increased profile losses. Comparing Fig.4.11 and Fig.4.13 gives a somehow contradictory picture, if the region around the loss cores is evaluated, as one might get to different conclusions when examining one of the figures alone. To get a full picture of the behaviour of the flow, it is therefore important to evaluate both figures together.

The observations and explanations of Chap. 4.2.1 are in general supported by the evaluation of the pitchwise mass-averaged total pressure coefficient.

### 4.2.3 Pitchwise mass-averaged Exit Flow Angle $\overline{\beta}_1$

The deviation of the pitchwise mass-averaged exit flow angle,  $\overline{\beta}_1$  versus blade height is presented in Fig. 4.14. The deviation of the pitchwise mass-averaged exit flow angle, denoted with  $\Delta\overline{\beta}_1$ , is measured compared to the blade exit angle  $\beta_1' = 14.5^\circ$ . Therefore, positive values of  $\Delta\overline{\beta}_1$  mean underturning of the flow, whereas negative values of  $\Delta\overline{\beta}_1$  mean overturning of the flow, respectively.

At midspan, flow turning of Set 1 and Set 3 is very close to each other. Since the inlet flow angle is fixed and equal for all configurations, the flow turning is increased by about  $1^\circ$  by Set 2. In the endwall region, a significant decrease of overturning can be observed for both compound lean configurations, Set 2 and Set 3. This is a strong indication, that cross flow is decreased near the endwall. Set 3, in addition, experiences a lower level of flow underturning in the region around the loss core due to three-dimensional effects than Set 2 and the cylindric blade.

In general, a more uniformly distributed nozzle exit flow angle in spanwise direction is expected to have favourable influence on the losses in the downstream rotor blade row of an axial turbine. This favourable influence can be explained with decreased incidence losses in the subsequent rotor blade row. From that point of view, Set 3 is to be preferred to the other Sets. Nevertheless, in a real turbine, the subsequent rotor blade row may be designed to cope with spanwise non-uniformly distributed nozzle exit flow, so this non-uniformly distributed outflow of the stator is not necessarily a disadvantage.

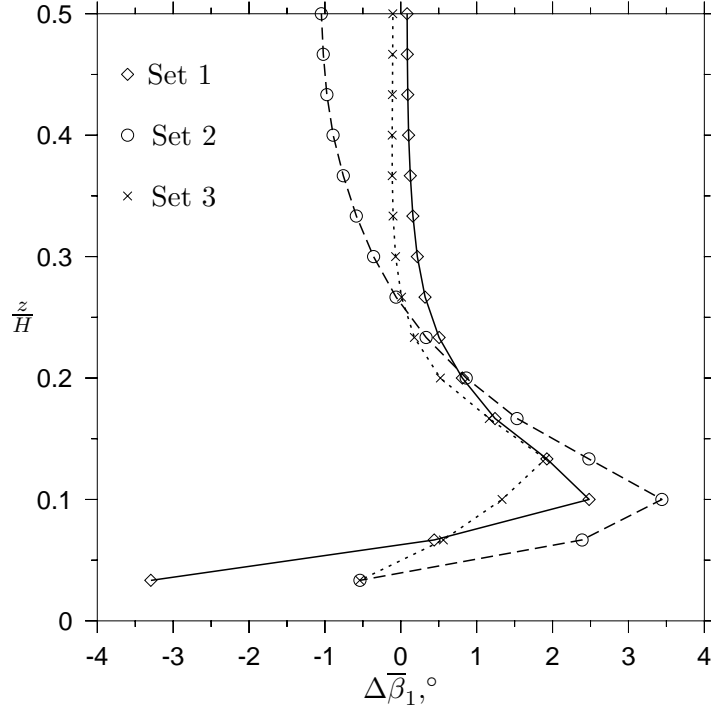


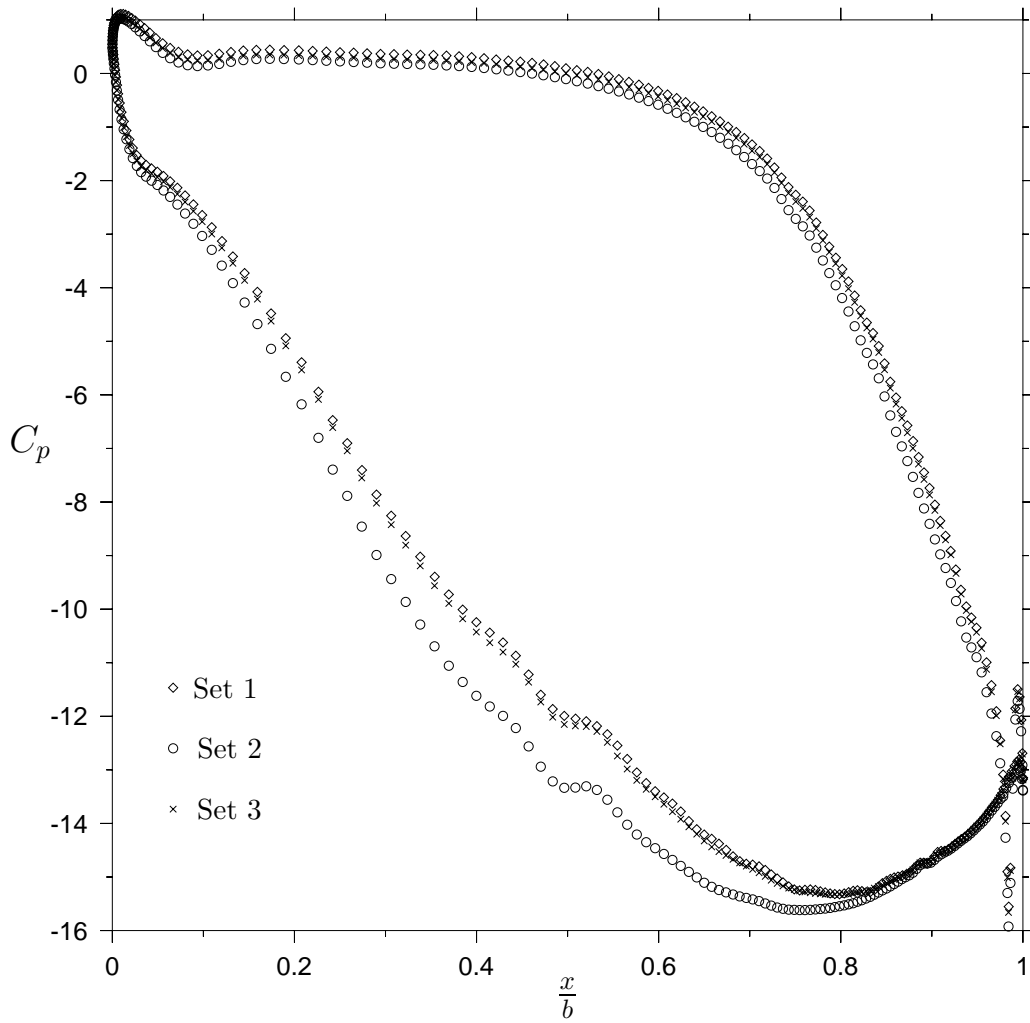
Figure 4.14: Pitchwise mass-averaged Exit Flow Angle Deviation  $\Delta\bar{\beta}_1$

#### 4.2.4 Static Profile Pressure at Midspan and Endwall

The phenomenons and flow behaviour of the various blade designs, which were described in the preceding sections, can, at least in part, be explained when evaluating and comparing the profile static pressures at midspan and at the endwall of all three designs. Again, the profile static pressure is quantified by means of the static pressure coefficient  $C_p$ , defined in Eq. 4.2.

Figure 4.15 shows the distribution of the static profile pressure coefficient  $C_p$  at midspan vs. the distance from the blade leading edge, normalized with the axial chord length.

Contrary to the experiment, the stagnation point, with  $C_p = 1$ , can clearly be identified in the CFD calculation. The reason is, that the value of the static pressure coefficient can be evaluated for every grid point on the blade at midspan, so there is at least a grid point very close to the stagnation point, if not on the stagnation point itself. The values on the pressure side are very close to each other, however slightly lower values of  $C_p$  can be observed for Set 3 than for Set 1, as well as slightly lower values for Set 2 than for Set 3. On the suction side, values of static pressure coefficient are nearly equal for Set 1 and Set 3, for Set 2 they are lower. As the bladeloading is represented by the area between the curves of  $C_p$  of the pressure and the suction side, Set 2 experiences a substantial higher bladeloading than the other two configurations. This explains the increased flow turning at midspan, observed already in Fig. 4.14, as well as the increased blade profile loss depicted in Fig. 4.13.

Figure 4.15: Static Profile Pressure Coefficient  $C_p$  at Midspan

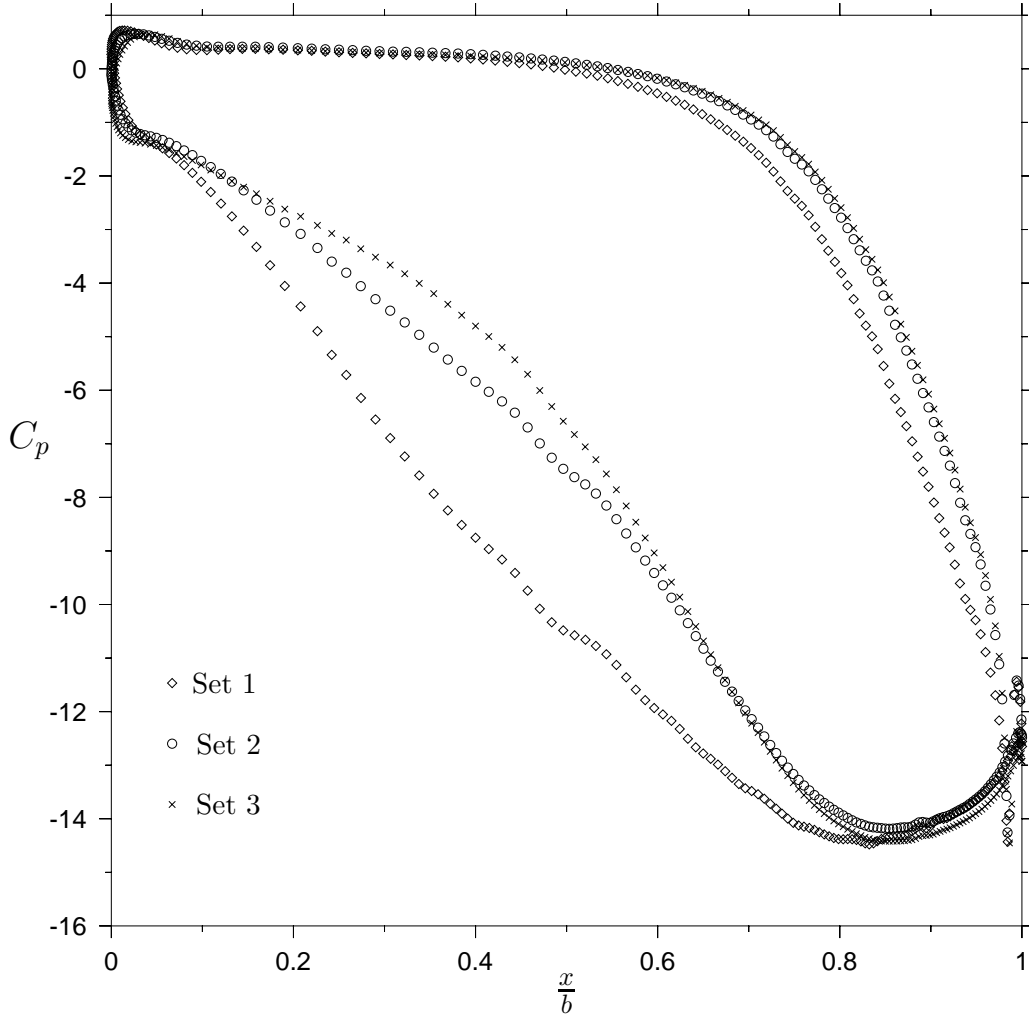


Figure 4.16: Static Profile Pressure Coefficient  $C_p$  at Endwall

In Fig. 4.16 the static pressure coefficient  $C_p$  at the endwall ( $\frac{z}{H} = 0$ ) is presented.

On the pressure side, the static pressure coefficient is higher for both compound lean configurations, Set 2 and Set 3. This increase of pressure at the endwall originates from the blade force in spanwise direction, which is induced by the acute angle between the blade pressure side and the endwall. The higher pressure at the endwall means lower velocities there, which, as a consequence, lead to lower endwall losses. On the suction side  $C_p$  is increased for both compound lean blades, compared to the cylindrical blade, reasonably more for Set 3 than for Set 2. Evaluating again the area between pressure and suction side, a significant unloading of Set 2 and Set 3 can be observed.

Finally, the lower pressure difference between suction and pressure sides of the compound lean configurations at the endwall decreases the crossflow there and hence reduces the intensity of secondary flow.

## 5 Conclusion and Outlook

If you would be a real seeker  
after truth, it is necessary, that at  
least once in your life you doubt,  
as far as possible, all things.

---

*(René Descartes,  
French Mathematician)*

### 5.1 Experiment

A HP steam turbine blade cascade was chosen to be optimised numerically, calibrating and verifying the results with experimental data.

Experimental calibration of the numerical optimisation process was done in a low speed cascade windtunnel at a Mach number  $Ma \approx 0.2$ , so, the assumption of incompressible conditions was reasonable. The conditions in the experiment did not fully meet the conditions, that can be observed in real turbines, however, it was shown, that the conditions in the experiment were adequate enough for the results to be comparable to real turbine applications. 2D and 3D pressure fields were measured in a plane parallel and downstream to the cascade exit plane, in addition the profile pressure was measured by means of pressure taps at midspan.

In comparing the results of the experiment with the results of the optimisation, it could be shown, that in the wake of the cascade experimental data and numerical results show very good agreement in regions of undisturbed flow, qualitatively and quantitatively, as well as in regions with mild secondary flow. In regions with strong secondary flow, the results of the experiments could be verified by the numerical results only qualitatively not quantitatively. One reason for this might be, that the current installation of the windtunnel has geometric disadvantages that cannot easily be overcome. First of all, four different coordinate systems are involved, when traversing probes behind a cascade, so some systematic error has to be accepted in the results. Second, the possibilities for adjusting the various components such as blade mounting box or traversing unit geometrically are limited and do not meet highest standards of accuracy for aerodynamic investigations. Third, the accuracy of the appliances for measuring the exact geometric relations between the involved components of the windtunnel is improvable.

The measurements of the blade load turned out to be of very good accuracy.

One very important issue when measuring linear blade cascades in a windtunnel is to guarantee, that periodic conditions of the cascade are provided. This was perfectly sim-

ulated and verified with the setup chosen for the experiment.

After some initial difficulties, it turned out, that aerodynamic measurements of turbine blades require very high levels of accuracy of all components involved. Great importance has to be attached to very careful calibration of the measuring devices. In this experimental work for example, tremendous improvements of the results were achieved after attentative recalibration of all pressure probes and pressure sensors involved.

It shall be mentioned, that in the author's opinion, the probe size of the three-hole pressure probe and of the five-hole pressure probe is rather large in comparison to the throat width of the measured cascade. Further miniaturisation of the probes can eventually improve the results.

Finally, the deployment of optical measurement methods, such as Laser Doppler anemometry (LDA) could further help to get more insight in the nature and behaviour of secondary flow inside the blade passage and downstream of turbine blade cascades.

### 5.2 Optimisation and Numeric Flow Calculation

Starting with the cylindric steam turbine blade, a numerical optimisation process was initiated with the objective to get an optimum blade with minimum aerodynamic loss. The objective function chosen to be minimised was total pressure loss coefficient. A genetic algorithm was programmed as optimisation algorithm, the 3D numeric calculations were done with ANSYS Fluent<sup>®</sup>. The whole process was designed to run fully automatic without the need of any human intervention and it ran flawlessly, until aborted by the user.

The optimisation process delivered an optimum compound lean configuration with a 1.5% lower total loss coefficient than that of the cylindrical blade. However, as it was suspected, that this configuration could be difficult to manufacture, a second configuration with a total pressure loss coefficient nearly as low as the optimum was evaluated as well. Comparing all three sets of blades revealed all sorts of different flow phenomena that contribute to loss, e.g. profile loss or secondary loss. In addition, positive influence on the homogeneity of the flow angles could be observed.

Comparing the results of the experiment and the calculation suspicion rose, that the choice of the turbulence model should be reconsidered for the flow situation investigated, as losses were somehow overpredicted by the applied Standard  $k/\varepsilon$  model.

Deployment of a specially adapted  $k/\varepsilon$  model, a RNG  $k/\varepsilon$  model, a  $k/\omega$  model or some other model appear to be promising alternatives.

The advantages of a genetic algorithm, namely quasi-independence of chosen starting point and unrivalled robustness, proved to be very useful. The comparatively high costs in terms of computing time are surely a fact to be thought of, before applying such

an algorithm. However, a lot of possibilities for fine-tuning genetic algorithms exist, which can make the use of those algorithms an interesting alternative in commercial environments as well. The possibility to alter an unlimited <sup>1</sup> number of variables during optimisation builds a strong asset of this optimisation method.

Contrary to other works, which used commercial code programs for optimisation algorithms, the genetic algorithm applied here was programmed by the author. This secures full control and insight of the algorithm, which allows to adapt the optimisation method to the original task and not vice versa.

For future optimisation tasks in turbomachinery, the following improvements could be implemented:

- Integration of more geometric parameters to be altered during the optimisation
- Integration of the possibilities of parallel computing
- Possibilities of automatic grid check during optimisation and automatic alteration of the mesh in order to meet specified quality parameters before being exported for calculation in CFD
- Better self-checks for convergence of the CFD calculations during iteration and algorithms for self-adapting iteration numbers
- Fully automated generation of reports and graphs during the optimisation (For this work it was only partly automated.)

### 5.3 General Developments

Turbines form the backbone of today's production of electric energy and will probably continue to do so for the next decades to come. Economical and environmental concerns demand, that these machines become more and more efficient, as even small efficiency improvements have a huge impact on their economic and ecological efficiency, given their average runtimes and their huge consumption of primary energy carriers. One possibility to improve the efficiency of those machines is to improve their aerodynamic performance.

In general, increasing of efficiency is done in a multistage process:

1. Preliminary considerations
2. Thermodynamic process calculations
3. Blade profile design, 1D and 2D analytical calculations
4. 2D and 3D numerical calculations, Cascade Tests<sup>2</sup>, Optimisation
5. Elasto-mechanical calculations, thermodynamic calculations

---

<sup>1</sup>Limitation is dictated by the computing power available.

<sup>2</sup>Linear and Annular Cascades

6. Experimental verification in model turbines
7. Deployment in real-world turbines

Normally, these steps have to be followed in the order listed here, although almost always, looping processes will have to be performed, going through certain stages again and again (e.g. elasto-mechanical constraints do not allow geometries, that were calculated in the preceding steps). It is interesting to note, that no prototyping at all is usually done for large turbomachines, as it would simply be too expensive to produce a prototype steam turbine of hundreds of megawatt output, and, testing facilities for those devices, i.e. testing powerplants, simply do not exist.

In this work, investigations of step 4 were performed. It could be shown, that the tools chosen, viz. experimental calibration of a 3D numerical optimisation process with a genetic algorithm, can indeed qualify for further usage for the task of improving aerodynamic performance of turbine blades. In a next step, which will probably still be done at the Institute of Thermodynamics and Energy Conversion of the Vienna University of Technology, the optimised compound lean configurations will be manufactured, tested and compared with the results of CFD. Then, thorough recalculation with CFD will follow. As a last research project at the institute, the compound lean stator configuration could be calculated and evaluated together with a rotor as a whole stage by means of CFD.

Finally, it should be mentioned, that this work is to be seen at the boundary between basic and applied research, as basic physical laws were used, to find out more about complex flow phenomena in an engineering application. At most, the methods were fine-tuned for the specific task to perform, but no fundamental new methods or laws were developed.

## **A Geometric Data of the Blade**

*A Geometric Data of the Blade*

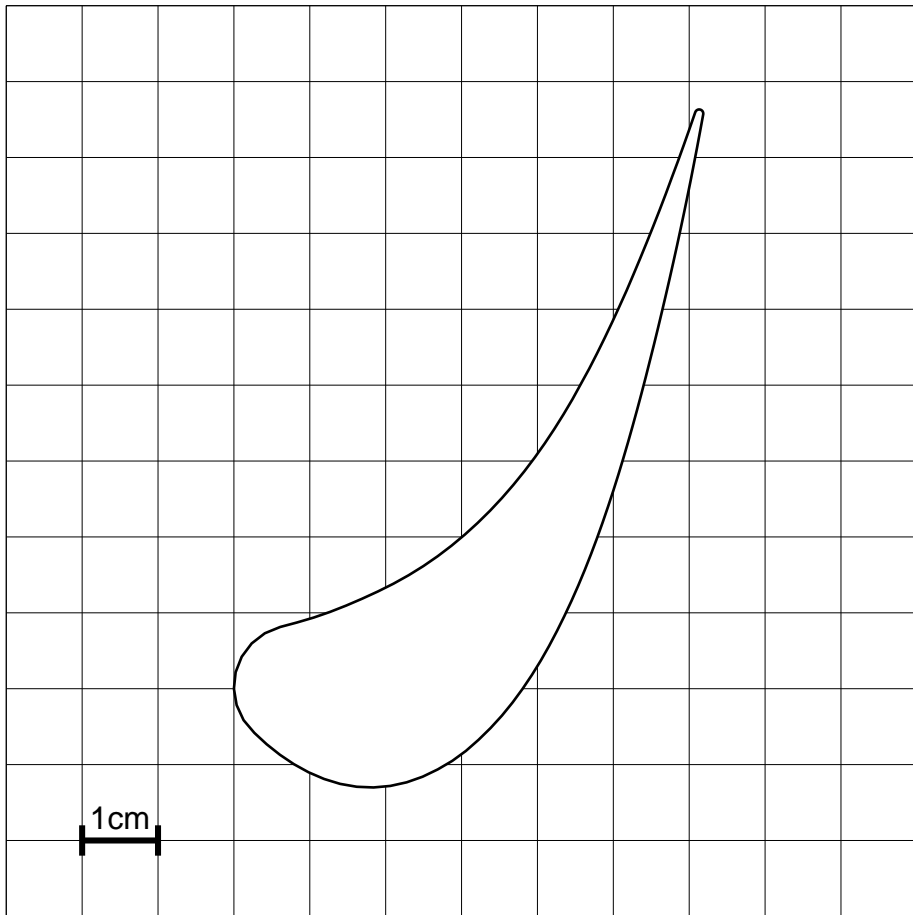


Figure A.1: Model Blade Profile (Original Size)

## A Geometric Data of the Blade

Node No.	$x/c$	$y/c$	Node No.	$x/c$	$y/c$
1	0.00000	0.00000	57	0.61456	0.73547
2	0.00229	0.02177	58	0.61047	0.71366
3	0.01029	0.04214	59	0.60627	0.69186
4	0.02342	0.05965	60	0.60197	0.66994
5	0.04073	0.07304	61	0.59758	0.64833
6	0.06098	0.08134	62	0.59308	0.62659
7	0.08310	0.08723	63	0.58848	0.60488
8	0.10505	0.09370	64	0.58378	0.58319
9	0.12668	0.10118	65	0.57899	0.56152
10	0.14798	0.10955	66	0.57409	0.53987
11	0.16901	0.11858	67	0.56911	0.51824
12	0.18980	0.12816	68	0.56402	0.49664
13	0.21026	0.13840	69	0.55884	0.47505
14	0.23027	0.14951	70	0.55357	0.45349
15	0.24971	0.16158	71	0.54819	0.43220
16	0.26855	0.17458	72	0.54269	0.41046
17	0.28676	0.18844	73	0.53708	0.38898
18	0.30434	0.20309	74	0.53134	0.36754
19	0.32127	0.21848	75	0.52545	0.34614
20	0.33757	0.23456	76	0.51939	0.32479
21	0.35322	0.25126	77	0.51315	0.30349
22	0.36823	0.26853	78	0.50670	0.28226
23	0.38263	0.28632	79	0.50002	0.26109
24	0.39643	0.30458	80	0.49309	0.24000
25	0.40965	0.32326	81	0.48590	0.21900
26	0.42232	0.34232	82	0.47842	0.19811
27	0.43447	0.36171	83	0.47062	0.17733
28	0.44614	0.38140	84	0.46246	0.15668
29	0.45715	0.40146	85	0.45392	0.13620
30	0.46816	0.42152	86	0.44495	0.11590
31	0.47861	0.44189	87	0.43554	0.09580
32	0.48872	0.46242	88	0.42568	0.07591
33	0.49855	0.48309	89	0.41531	0.05629
34	0.50811	0.50389	90	0.40435	0.03699
35	0.51759	0.52480	91	0.39270	0.01810
36	0.52649	0.54581	92	0.38033	-0.00032
37	0.53536	0.56691	93	0.36719	-0.01821
38	0.54405	0.58808	94	0.35320	-0.03543
39	0.55258	0.60932	95	0.33823	-0.05182
40	0.56094	0.63062	96	0.32238	-0.06735
41	0.56915	0.65199	97	0.30570	-0.08199
42	0.57704	0.67341	98	0.28779	-0.09508
43	0.58511	0.69489	99	0.26866	-0.10633
44	0.59286	0.71642	100	0.24867	-0.11595
45	0.60049	0.73801	101	0.22775	-0.12334
46	0.60798	0.75963	102	0.20609	-0.12813
47	0.60870	0.76104	103	0.18401	-0.13013
48	0.60980	0.76218	104	0.16185	-0.12921
49	0.61118	0.76295	105	0.13999	-0.12540
50	0.61272	0.76330	106	0.11878	-0.11892
51	0.61430	0.76318	107	0.09840	-0.11014
52	0.61578	0.76262	108	0.07898	-0.09942
53	0.61703	0.76166	109	0.06058	-0.08702
54	0.61795	0.76038	110	0.04320	-0.07322
55	0.61847	0.75889	111	0.02691	-0.05816
56	0.61856	0.75730	112	0.01277	-0.04145
			113	0.00358	-0.02159
			114	0.00000	0.00000

Table A.1: Blade Profile Coordinates

A Geometric Data of the Blade

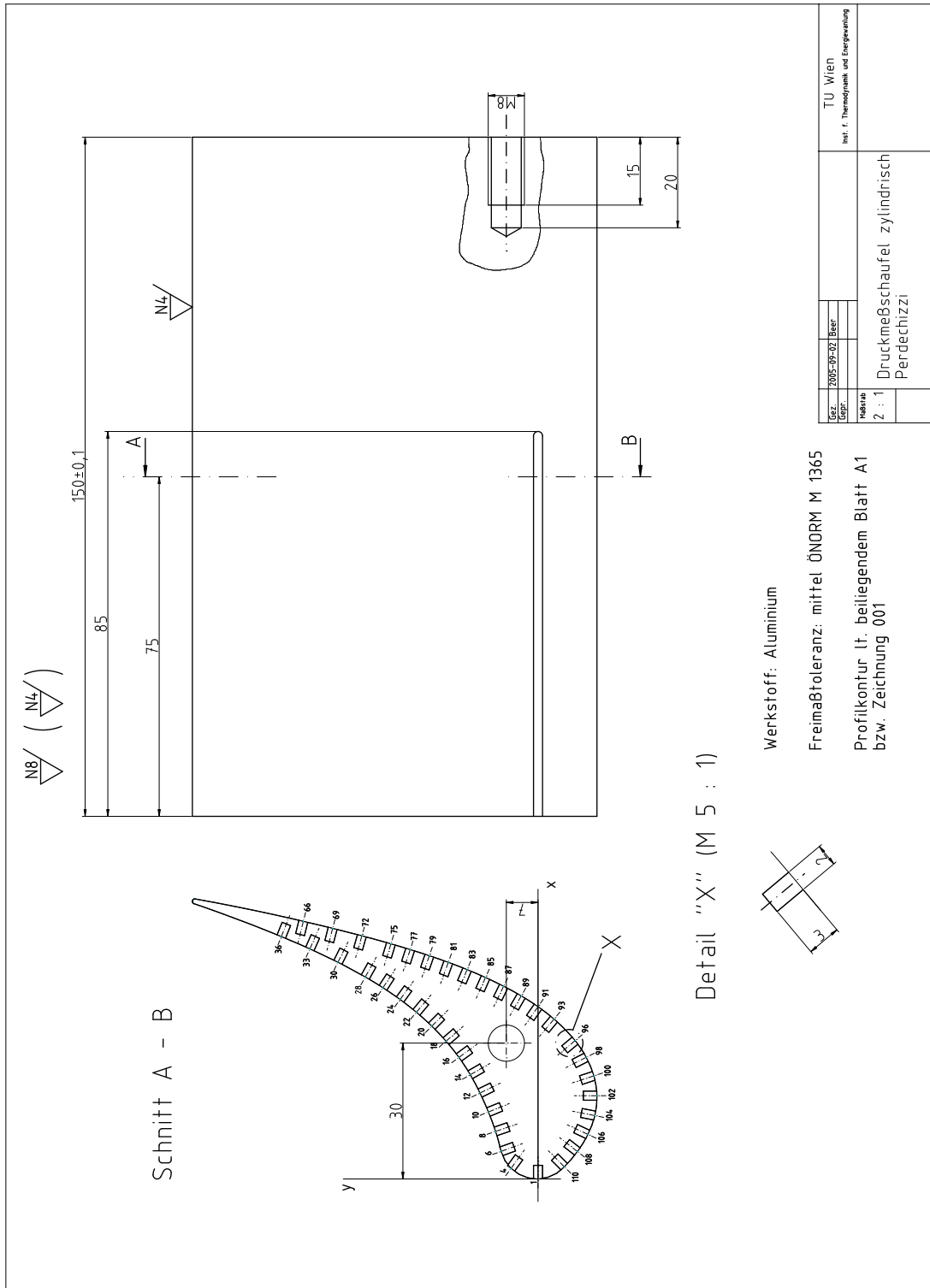


Figure A.2: Model Blade for Static Pressure Measurements

## B Used Software

In this work, commercially available and free software was used. The commercial programs were

- ANSYS Fluent, version 6.2.16
- ANSYS Gambit, version 2.1.2.

The Free Software used was published under the Gnu Public License (GPL). The programs used were

- Shell scripts written in the Bourne Again Shell (Bash),
- GCC - The GNU Compiler Collection
- Octave - High Level language for numerical calculations,
- Gri - Scientific graphics language
- gnuplot - A plotting package which outputs to X11, PostScript, PNG, GIF, and others

In addition,  $\text{\LaTeX}$  2 $\epsilon$ , published under the LaTeX Project Public License (LPL) was used for typesetting this work.

## Bibliography

- [1] 2001. “Is My Simulation Converged?” <http://www.fluent.com/about/news/newsletters/01v10i2/a20.htm>.
- [2] 2007. “International Energy Outlook 2007”. Tech. rep., <http://www.eia.doe.gov>, Energy Information Administration.
- [3] 2008. “Annual European Community greenhouse gas inventory 1990-2006 and inventory report 2008”. Tech. rep., European Commission, DG Environment European Environment Agency.
- [4] Anderson, Jr., John D., 2007. *Fundamentals of Aerodynamics*. 4th edn. McGraw-Hill.
- [5] Chen, B., and Yuan, X., 2008. “Advanced Aerodynamic Optimization System for Turbomachinery”. ASME Journal of Turbomachinery, vol. 130 pp. 021005–1 – 021005–12.
- [6] Dawes, W.N., 1983. “Computation of viscous compressible flow in blade cascades using an implicit iterative replacement algorithm”. TPRD/M/1377/N83.
- [7] Denton, J.D., 1993. “Loss Mechanisms in Turbomachines”. ASME Journal of Turbomachinery, vol. 115 pp. 621–656.
- [8] Durbin, P.A., 1996. “On the  $k/\varepsilon$  stagnation point anomaly”. International Journal of Heat and Fluid Flow, vol. 17 pp. 89 – 90.
- [9] Harrison, S., 1990. “Secondary Loss Generation in a Linear Cascade of High-Turning Turbine Blades”. ASME Journal of Turbomachinery, vol. 112 pp. 618 – 624.
- [10] Harrison, S., 1992. “The Influence of Blade Lean on Turbine Losses”. ASME Journal of Turbomachinery, vol. 114 pp. 184–190.
- [11] Havakechian S., R., Greim, 1999. “Aerodynamic Design of 50 Percent Reaction Steam Turbines”. In “Proceedings of the Inst. of Mech. Eng., Part C: Journal of Mech. Eng. Science”, vol. 213, pp. 1–25.
- [12] Heithoff, J., and Ewers, J., 2006. “Technologiefade der zukünftigen Stromerzeugung bei RWE”. Kongress vom 2. Mai 2006 der RWTH Aachen: Neue Wege in der Kraftwerkstechnik.
- [13] Hildebrandt, T., and Fottner, L., 1999. “A Numerical Study of the Influence of Grid Refinement and Turbulence Modelling on the Flow inside a Highly Loaded Turbine Cascade”. ASME Journal of Turbomachinery, vol. 121 pp. 709 – 716.
- [14] Horlock, J.H., and Denton, J.D., 2005. “A Review of Some Early Design Practice Using Computational Fluid Dynamics and a Current Perspective”. ASME Journal of Turbomachinery, vol. 127 pp. 5–13.

## Bibliography

- [15] Kirkpatrick, S., Gelatt, C.D., and Vecchi, M.P., 1983. "Optimization by Simulated Annealing". *Science*, vol. 220 pp. 671–680.
- [16] Klein, A., 1966. "Untersuchungen über den Einfluss der Zuströmungsgrenzschicht auf die Sekundärströmung in den Beschaufelungen von Axialturbinen". In "Forsch. Ing.", vol. 32.
- [17] Kline, S. J., Morkovin, M.V., G., Sovran, and Crockett, D.J., 1969. "Computation of Turbulent Boundary Layers". In "1968 AFOSR-IFP-Stanford Conference", vol. I.
- [18] Lampart, P., and A., Gardzilewicz, 1999. "Numerical study of 3D blading in HP impulse turbine". In "CIELPNE MASZYNY PRZEPLYWOWE, TURBOMACHINERY", no. 115, pp. 297 – 310.
- [19] Lampart, P., A., Gardzilewicz, A., Rusanov, and Yershov, S., 1999. "The effect of stator blade compound lean and compound twist on flow characteristics of a turbine stage - numerical study based on 3D NS simulations". In "Proceedings of the ASME PVP Conference", vol. 397-2, pp. 195 – 204. ASME.
- [20] Lampart, P., and Yershov, S., 2002. "3D shape optimisation of turbomachinery blading". *TASK Quarterly, Scientific Bulletin of the Academic Computer Centre in Gdansk*, vol. 1 pp. 113 – 126.
- [21] Langston, L.S., 2001. "Secondary Flows in Axial Turbines - A Review". *Heat Transer in Gas Turbine Systems*, vol. 934 of the *Annals of the New York Academy of Sciences*.
- [22] Langston, L.S., Nice, M.L., and Hooper, R.M., 1977. "Three-Dimensional Flow Within a Turbine Cascade Passage". *ASME Journal of Engineering for Power*, pp. 21 – 28.
- [23] Launder, B.E., and Spalding, D.B., 1974. "The numerical computation of turbulent flows". *Computer methods in applied mechanics and engineering*, vol. 3. North-Holland-Publishing Company.
- [24] Mayle, R.E., 1991. "Fundamental Aspects of Boundary Layers and Transition in Turbomachines". In "VKI Lecture Series: Boundary Layers in Turbomachines", published by Arts, T.
- [25] Michalewicz, Zbigniew, 1996. *Genetic Algorithms + Data Structures = Evolution Programs*. Springer-Verlag Berlin Heidelberg New York.
- [26] Müller, K.J., and Willinger, R., 2001. "Vorlesungen über Grundzüge der thermischen Turbomaschinen". Fassung 2001.
- [27] Nelder, J.A., and Mead, R.A., 1965. "A Simplex Method for Function Minimization". *Computer Journal*, vol. 7 pp. 308 – 312.
- [28] Orszag, S.A., Yakhot, V., Flannery, W.S., Boysan, F., Choudhury, D., Maruzewski, J., and Patel, B., 1993. "Renormalization Group Modeling and Turbulence Simulations". In Speziale, C.G., and Launder, B.E., eds., "Near Wall Turbulent Flows", Elsevier Science Publishers B.V.
- [29] Perdichizzi, A., and Dossena, V., 1993. "Incidence Angle and Pitch-Chord Effects on Secondary Flows Downstream of a Turbine Cascade". *ASME Journal of Turbomachinery*, vol. 115 pp. 383 – 391.

## Bibliography

- [30] Ploetz, C., 2003. "Sequestrierung von CO<sub>2</sub>: Technologien, Potenziale, Kosten und Umweltauswirkungen". Externe Expertise für das WBGU-Hauptgutachten 2003 "Welt im Wandel: Energiewende zur Nachhaltigkeit".
- [31] Press, W.H., S.A., Teukolsky, W.T., Vetterling, and Flannery, B.P., 1992. *Numerical Recipes in C*. 2nd edn. Cambridge University Press.
- [32] Pritchard, L.J., 1985. "An Eleven Parameter Axial Turbine Aerofoil Geometry Model". ASME Paper no. 85-GT-219.
- [33] Russel, S., and Norvig, P., 2002. *Artificial Intelligence: A Modern Approach*. 2nd edn. Prentice Hall.
- [34] Schlichting, H., and Gersten, K., 2003. *Boundary Layer Theory*. 8th edn. Springer-Verlag Berlin Heidelberg New York.
- [35] Sieverding, C.H., 1985. "Recent Progress in the Understanding of Basic Aspects of Secondary Flows in Turbine Blade Passages". ASME Journal of Turbomachinery, vol. 107 pp. 248–257.
- [36] Stachel, Hellmuth, 1986. *Arbeitsskriptum zur Vorlesung Darstellende Geometrie für die Studienrichtung Maschinenbau*. HTU Wien.
- [37] <http://ec.europa.eu/eurostat>. Statistical Office of the European Communities.
- [38] Treaster, A.L., and Yocum, A.M., 1979. "The Calibration and Application of Five-Hole Probes". In "ISA Transactions", vol. 18, pp. 23–34.
- [39] Trigg, M.A., Tubby, G.R., and Sheard, A.G., 1999. "Automatic Genetic Optimization Approach to Two-Dimensional Blade Profile Design for Steam Turbines". ASME Journal of Turbomachinery, vol. 121 pp. 11–17.
- [40] Van den Braembussche, R.A., 2001. "Design and Optimisation of Turbomachinery Components". Paper no. ATI-CST-IL2/01, pp. 5–20. 4<sup>th</sup> European Conference on Turbomachinery.
- [41] Walters, D.K., and Leylek, J.H., 2000. "Impact of Film-Cooling Jets on Turbine Aerodynamic Losses". ASME Journal of Turbomachinery, vol. 122 pp. 537 – 545.
- [42] Wanjin, H., Zhongqi, W., Chunqing, T., Hong, S., and Mochun, Z., 1994. "Effects of Leaning and Curving of Blades With High Turning Angles of the Aerodynamic Characteristics of Turbine Rectangular Cascades". ASME Journal of Turbomachinery, vol. 116 pp. 417 – 424.
- [43] Weiss, A.P., and Fottner, L., 1995. "The Influence of Load Distribution on Secondary Flow in Straight Turbine Cascades". ASME Journal of Turbomachinery, vol. 117 pp. 133 – 141.
- [44] White, F.M., 1991. *Viscous Fluid Flow*. 2nd edn. McGraw-Hill.
- [45] Wilcox, D.C., 2006. *Turbulence Modeling for CFD*. 3rd edn. DCW Industries.
- [46] Willinger, R., 2002. *Sekundär- und Spaltströmung im axialen Turbinengitter unter Teil-, Nenn-, und Überlastbedingungen*. No. 433 in Fortschritt-Berichte VDI, Reihe 7. VDI Verlag.
- [47] Wingelhofer, F., 2003. "Neue Kriterien zur Auslegung dreidimensionaler Beschaukelungen von Axialturbinen". Projektberichte des ZID der TU Wien.

## *Bibliography*

- [48] Wingelhofer, F., and Haselbacher, H., 2004. “New Optimization Criteria For the Design of Three-Dimensional Bladings Applied to Compound Lean Nozzles of an Axial Turbine”. ASME Paper no. GT2004-53830.

# Index

- 1/7 power law, 73
- Algorithm
  - Simplex, 53
  - Simulated Annealing, 53
- ANSYS
  - Fluent, 73, 74, 100
  - Gambit, 60
- Bilinear interpolation, 38
- Blade profile pressure
  - at endwall, 98
  - at midspan, 33, 47, 88, 97
- Blade profile stacking line, 90, 94
- Bladeload
  - at endwall, 98
  - at midspan, 47, 88, 96
- Boussinesq approximation, 66
- CO<sub>2</sub> sequestration, 17
- Compound twist, 25
- Computational Domain, 60
- Continuity equation, 70
- Convergence, 76
- Discretisation scheme, 74
- Five-hole pressure probe, 100
  - Calibration data, 37, 39
  - Sketch of, 36
  - Total pressure coefficient with, 49
  - Yaw angle, 48
- Flow angle
  - Pitchwise, 43, 46, 79, 82, 95
  - Spanwise, 47, 81
- Laser Doppler anemometry, 100
- Logarithmic Law of Wall, 69
- Measuring setup, 31
- Navier Stokes equations, 71
- Reynolds-averaged Navier Stokes equation (RANS), 66
- Stagnation point, 47, 96
- Stagnation point anomaly, 84, 85, 88
- Static pressure coefficient, 81
- Sutherland's law, 34
- Three-hole pressure probe, 100
  - Calibration data of, 35
  - Sketch of, 34
  - Total pressure coefficient with, 45
  - Yaw angle, 35
- Time-averaging, 64
- Total pressure coefficient, 44, 45, 85, 87, 90
  - Pitchwise mass-averaged, 94
- Total pressure loss coefficient, 59, 77, 89
- Turbulence Model
  - $k/\omega$ , 63, 64
  - Full Reynolds stress, 86
  - High-Reynolds-Number  $k/\varepsilon$ , 63
  - Low-Reynolds-Number  $k/\varepsilon$ , 63, 64
  - Realizable, 86
  - Renormalization Group, 64, 86, 100
  - Standard  $k/\varepsilon$ , 64, 68, 72, 81, 84, 85, 100
- Turbulence intensity, 42
- Turbulent dissipation rate
  - Definition of, 68
  - Transport equation for, 67
- Turbulent kinetic energy
  - Transport equation for, 67
- Vortex
  - Corner, 20
  - Counter, 19

## *Index*

Horseshoe, 19, 90

Passage, 19, 47, 81, 90

Windtunnel

Linear cascade, 99